# Structure, function, and regulation of bacterial efflux pumps

by

**Nitin Kumar**

A dissertation submitted to the graduate faculty

in partial fulfillment of the requirements for the degree of

DOCTOR OF PHILOSOPHY

Major: Chemistry

Program of Study Committee:
Edward W. Yu, Major Professor
Drena L. Dobbs
Young-Jin Lee
Emily A. Smith
Wenyu Huang

Iowa State University

Ames, Iowa

2016

**TABLE OF CONTENTS**

ABSTRACT.....iii

CHAPTER 1. GENERAL INTRODUCTION.....1

CHAPTER 2. CRYSTAL STRUCTURE OF THE TRANSCRIPTIONAL REGULATOR RV1219C OF *MYCOBACTERIUM TUBERCULOSIS*.....14

CHAPTER 3. CRYSTAL STRUCTURE OF A HOPANOID TRANSPORTER OF *BURKHOLDERIA*.....48

CHAPTER 4. STRUCTURES AND TRANSPORT DYNAMICS OF A MULTIDRUG EFFLUX PUMP IN *CAMPYLOBACTER JEJUNI*.....93

CHAPTER 5. GENERAL CONCLUSIONS AND FUTURE DIRECTIONS.....128

ACKNOWLEDGEMENTS.....134

APPENDIX. *CURRICULUM VITAE*.....136

## ABSTRACT

The continued inappropriate use of antibiotics over the years has led to the development of resistance mechanisms in microorganisms against multiple drugs. One of the most important resistance mechanisms in Gram-negative bacteria is the usage of membrane proteins that act as efflux pumps and help in recognizing and exporting a broad range of drugs from the cell. This dissertation mainly focuses on the structure, function, and regulation of these bacterial efflux pumps. Using X-ray crystallography, we have studied the *Mycobacterium tuberculoi*s transcriptional regulator Rv1219c, which controls the expression of the ABC superfamily multidrug efflux pump Rv1217c-Rv1218c. We also quantified the binding of Rv1219c with different ligands and DNA using fluorescence polarization and isothermal titration calorimetry (ITC), respectively. An inner membrane protein HpnN belonging to the RND family in *Burkholderia multivorans*, is known to be involved in transporting certain pentacyclic lipids called hopanoids towards the outer membrane. To elucidate the structural basis of hopanoid transport, we have determined the crystal structures of HpnN. Further, by using *in vivo* studies we were able to confirm that HpnN mediates drug resistance in *B. multivorans* by transporting hopanoids, hence creating a protective layer in the outer membrane. In order to understand the structure and transport dynamics of multidrug efflux pump CmeB *in Campylobacter jejuni*, also belonging to the resistance nodulation-division (RND) family, we used X-ray crystallography and single-molecule fluorescence resonance energy transfer (sm-FRET) imaging. Using sm-FRET, we were able to see that one of the crystallized forms of CmeB follows a mechanism where each protomer in an RND trimer might be able to work independently, instead of the previously proposed “rotating mechanism”.

# CHAPTER 1. GENERAL INTRODUCTION

Antibiotics are undoubtedly one of the most successful drugs in history of medicine. They have contributed significantly to the control of infectious diseases responsible for high mortality rates in humans. Despite the great success of antibiotics, drug resistance in bacteria has emerged as a major public health problem. Resistant strains of microorganisms evolve naturally as result of erroneous replication or exchange of resistant traits between them. However, the use and misuse of antibiotics accelerates the emergence of drug-resistant strains and hence compromises their effectiveness. As a consequence of reduced effectiveness of the first-line drugs, the patients remain infectious for a longer time. Further, this leads to increased health care costs and an economic burden on families, due to need for more expensive therapies. According to WHO's 2014 report, antibiotic resistance in its present case scenario can be a huge threat to the treatment of common infections. The report further predicts that the world could be heading towards a post-antibiotic era, in which common infections that have been treatable for decades can once again kill if immediate steps are not taken to prevent it [1].

Resistance of Gram-negative bacteria to antibiotics is mediated by multiple mechanisms [2], which include decreased cell permeability, synthesis of certain antibiotic-inactivating enzymes, alteration of the drug target inside the cell and active extrusion of drugs from cells via multidrug efflux pumps. While the first three mechanisms typically confer resistance to a specific class of drugs, multidrug efflux pumps contribute to both intrinsic and acquired resistance to a broad range of antimicrobials and toxic compounds. Use of multidrug resistance (MDR) transporters for extrusion of various drugs is one of the most common resistance mechanism found in bacteria.

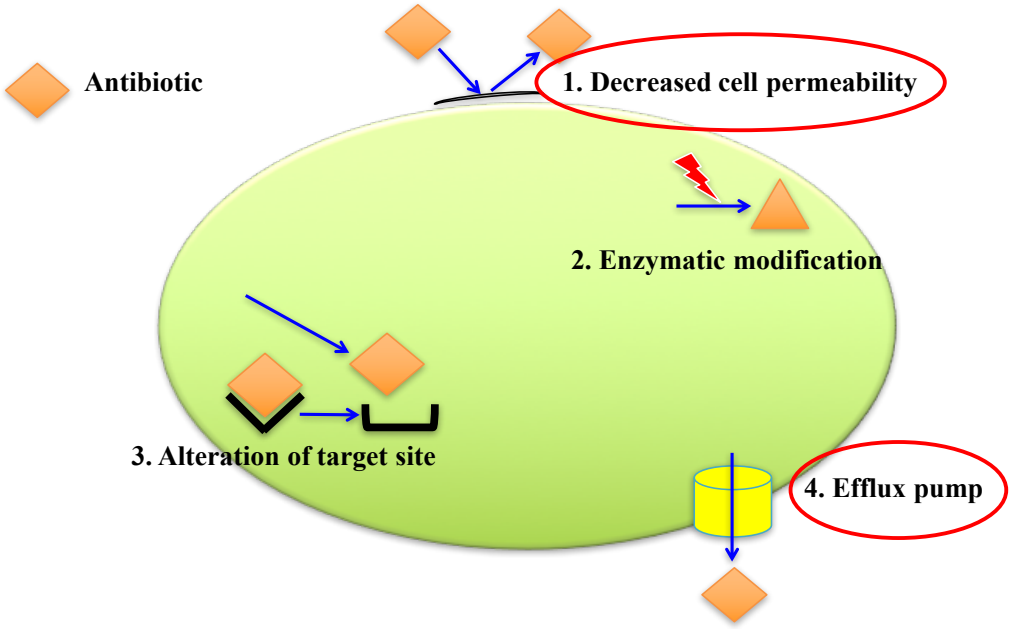


Figure 1. Antibiotic resistance mechanisms used by bacteria.

The bacterial multidrug efflux transporters can be divided into two major classes on the basis of bioenergetics and structural criteria: (i) the ATP-binding cassette (ABC) family, which uses ATP hydrolysis for active extrusion of the drugs, and (ii) Secondary transporters, which utilize the proton gradient or sodium ions to drive the pump. On the basis of size and similarities in the primary and the secondary structure, the secondary transporters can further be divided into four families: the major facilitator superfamily (MFS), the resistance-nodulation-cell division (RND) family, the small multidrug resistance (SMR) family, and the multidrug and toxic compound extrusion (MATE) family [3].

Gram-negative bacteria, in general, have their RND efflux pumps located within the inner membrane and function in complex with an outer membrane channel and a periplasmic adaptor protein to form a tripartite efflux pump spanning both the inner and the outer membrane. These protein complexes transport a wide variety of substrates including dyes, detergents, antibiotics, and host derived molecules, from the periplasm to the extra-cellular

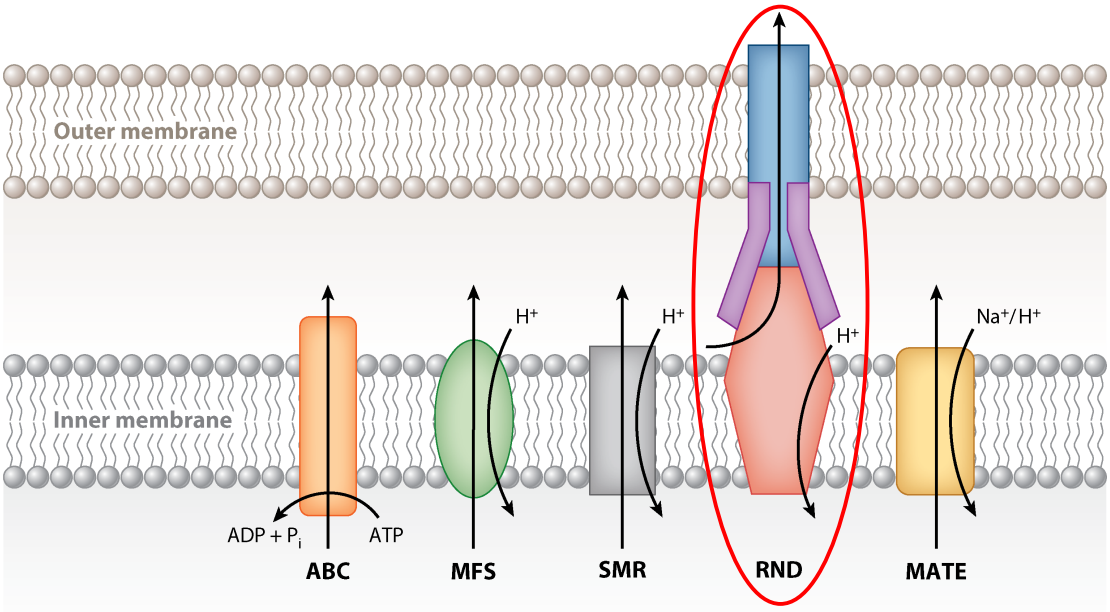


Figure 2. Classification of bacterial drug efflux pumps

space. Recent efforts have also been directed towards understanding the complex regulatory pathways controlling the expression of MDR genes.

Tuberculosis (TB) is responsible for millions of deaths across the world every year and still remains one of the deadliest diseases [4,5]. Recent studies indicate that multidrug resistance of *M. tuberculosis* is linked to constitutive or inducible expression of multidrug efflux pumps [6]. In Gram-negative bacteria, efflux systems of the RND superfamily play major roles in the intrinsic and acquired tolerance of antibiotics and noxious chemicals [7]. However, the ABC-type efflux transporters are not commonly linked to multidrug resistance. Recent work demonstrated that the ABC transporter Rv1217c–Rv1218c recognizes and actively extrudes a variety of structurally unrelated toxic chemicals and hence mediates the intrinsic resistance to these antimicrobials in *M. tuberculosis*. [8]. Repressor protein Rv1219c of *M. tuberculosis* is believed to regulate the transcription of Rv1217c-Rv1218c multidrug

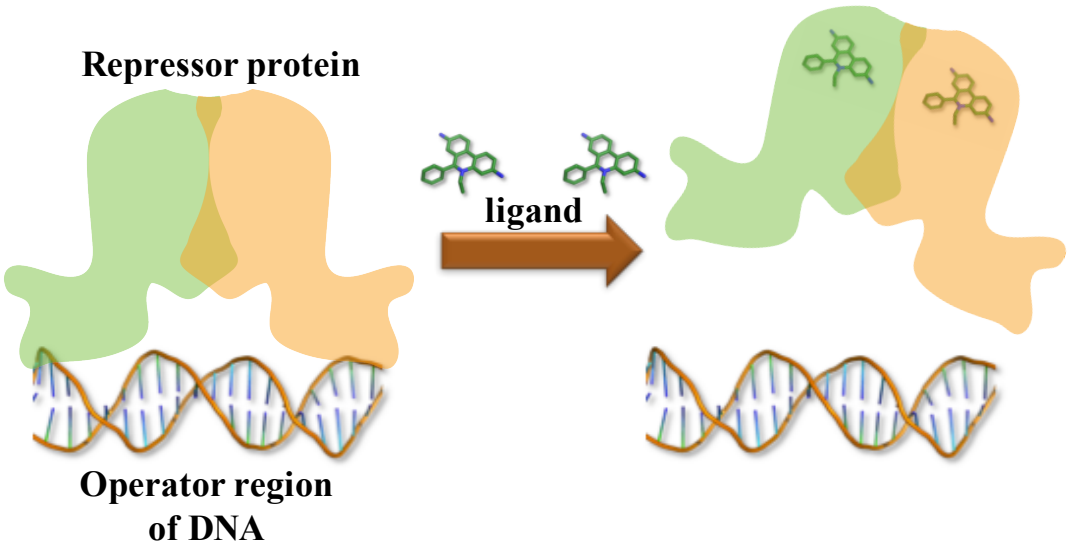


Figure 3. Transcriptional regulation mechanism in repressor proteins.

efflux system [9]. In general, a repressor protein binds to the operator region of DNA, thus blocking the progress of RNA polymerase along the DNA Strand. Once a suitable ligand binds to this protein, it releases the DNA, thus allowing the transcription of desired genes by RNA polymerase [10, 11].

In this project, we tried to establish how Rv1219c modulates the expression of Rv1217c-Rv1218c. One of the major goals of this project was to determine the structure of Rv1219c through crystallization to find out the important residues which allow it to bind to the different drugs.

*Burkholderia multivorans* is a member of the *Burkholderia cepacia* complex (Bcc) and is highly capable of affecting immunocompromised individuals, such as patients with cystic fibrosis (CF) [12]. Bcc pathogens are found to be intrinsically resistant to a broad range of antibiotics, which includes β-lactams, fluoroquinolones, aminoglycosides, polymyxins, and

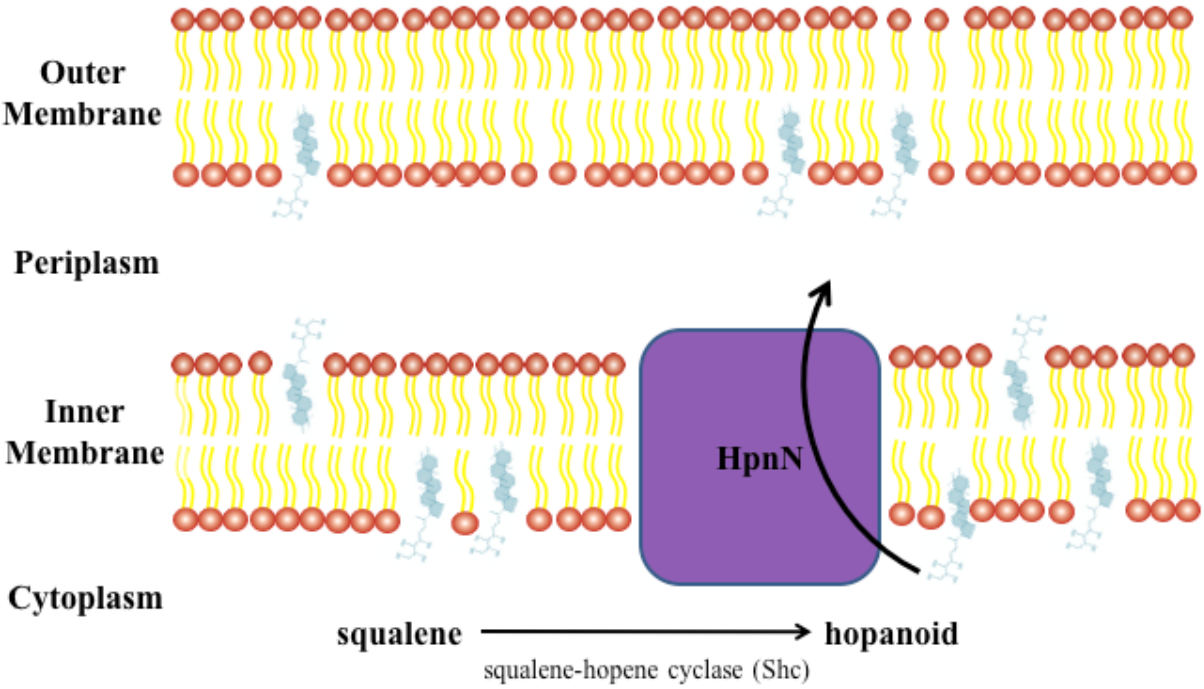


Figure 4. Proposed mechanism of hopanoid transport by RND family protein HpnN.

cationic peptides, thus posing a major challenge to the treatment of pulmonary infections caused by these bacteria [13]. It has been reported that pentacyclic triterpenoid lipids called "hopanoids" play a major role in maintaining membrane stability in *B. multivorans,* thus participating in multidrug resistance [13-15]. The hopanoids are structural analogs of sterols and like cholesterol in eukaryotic membranes, these hopanoids insert into the bacterial membranes, thus contributing to their stability and stiffness [16-19]. Recent studies have shown that Hopanoid biosynthesis-associated RND (HpnN) transporters [20,21], located in the inner membrane, are mainly responsible for shuttling hopanoids from the cytoplasmic membrane to the outer membrane of these Gram-negative bacteria. Thus, HpnN could be participating in drug resistance by transporting hopanoids towards the outer membrane and

hence decreasing the permeability of the cell towards antibiotics. In spite of the importance of hopanoids in bacteria, the mechanism of intracellular hopanoid trafficking for cell wall remodeling has not been explored.

Here, we mainly tried to study the structure-function of HpnN. Crystallization of HpnN was carried out to visualize the pathway for hopanoid transport and the important residues involved in the HpnN-hopanoid interaction. Further, site-directed mutagenesis was carried out to to perform *in vivo* studies in order to understand the importance of these residues in functioning of *Burkholderia* HpnN.

*Campylobacter jejuni* is a major causative agent of human enterocolitis [22] and is known to harbor multiple drug efflux transporters to mediate antibiotic resistance. Among them, the tripartite multidrug efflux system CmeABC [23-25], a hydrophobic and amphiphilic RND (HAE-RND) efflux pump [26] is the primary antibiotic efflux system and the best functionally characterized transporter in *Campylobacter.* The CmeABC tripartite complex comprises of the inner membrane transporter CmeB, the periplasmic membrane fusion protein CmeA, and the outer membrane channel CmeC. It has been found that this efflux pump also plays an important role in conferring resistance to *Campylobacter* against fluoroquinolones and bile compounds. Currently, the *Escherichia coli* AcrB [27-32] and *Pseudomonas aeruginosa* MexB [33] are the two multidrug transporters of the HAE-RND type efflux pumps whose structures have been resolved using crystallography. The other components of these tripartite systems have also been determined, which includes the outer membrane channels *E. coli* TolC [34] and *P. aeruginosa* OprM [35] as well as the periplasmic membrane fusion proteins *E. coli* AcrA [36] and *P. aeruginosa* MexA [37-39]. More recently, the crystal structure of outer membrane channel CmeC [40] of the tripartite complex CmeABC has been determined.

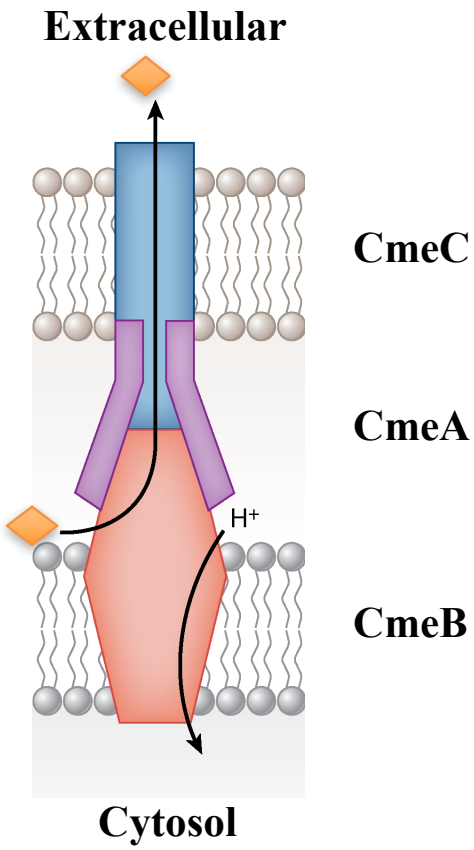


Figure 5. Model of CmeABC tripartite efflux pump in *Campylobacter jejuni*

The main aim of this project was to understand the transport mechanism of the CmeB efflux pump by structural elucidation using X-ray crystallography. In addition, the functional dynamics were studied using single-molecule FRET experiments.

## Thesis organization

Chapter 1 is the general introduction that provides the background information for the RND family hopanoid transporter HpnN, multidrug efflux pump CmeB and TetR family regulator Rv1219c.

Chapter 2 is a manuscript published in Protein Science, which describes the role of Rv1219c in regulating the expression of multidrug efflux pump Rv1217c-Rv1218c in *M. tuberculosis*. The crystal structures of Rv1219c together with the functional studies provide insight into the mechanism of transcriptional regulation by Rv1219c. Cloning of *rv1219c* was done by HT Lei. Expression, purification and crystallization was carried out by me and A. Radhakrishnan. Model building and structural refinement was done by TH Chou and CC Su.

Chapter 3 is a manuscript, presenting the crystal structures of *B. multivorans* HpnN, which is an inner membrane hopanoid transporter belonging to the RND family. The crystal structures are unique homodimers and the first of their type to be reported in the RND family. Cloning of *hpnN* was done by CC Su and me. Expression, purification and crystallization and was carried out by me. The *in-vivo* growth assays were designed by CC Su and carried out by me.

Chapter 4 is a manuscript, that describes two different crystal structures of multidrug efflux pump CmeB, which belongs to RND family and spans the inner membrane of *C. jejuni*. The crystal structures of CmeB suggest different transient states involved in drug efflux. Also, sm-FRET experiments allowed us to propose the mechanism involved in drug transport by CmeB. Cloning of *cmeB* was done by CC Su and me. Expression, purification and crystallization and was carried out by me and CC Su. Model building and structural refinement was done by CC Su. Single-molecule FRET recordings were carried out by L Yin and data analysis was done by CC Su and TH Chou.

Chapter 5 outlines conclusions and the future directions. This chapter mainly summarizes the findings in Chapter 2 to Chapter 4 in order to describe the structure, function and regulation of bacterial drug efflux pumps. Further, it states the additional set of experiments that must be performed next in order to address the key questions, and the new approaches that might be needed to overcome the challenges in the process.

## References


1) http://www.who.int/mediacentre/factsheets/fs194/en/
2) Zhang Q, Plummer P (2008) Mechanisms of Antibiotic Resistance in *Campylobacter*, p 263-276. *In* Nachamkin I, Szymanski C, Blaser M (ed), *Campylobacter*, Third Edition. ASM Press, Washington, DC.
3) Li XZ, Nikaido H (2004). Efflux-mediated drug resistance in bacteria. Drugs 64:159–204.
4) Maartens G, Wilkinson RJ (2007) Tuberculosis. *Lancet,* **370**:2030–2043.
5) World Health Organization (2010) Fact sheet no. 104: tuberculosis. Available at http://www.who.int/mediacentre/factsheets/fs104/en/index.html.
6) Nikaido H (2001) Preventing drug access to targets: cell surface permeability barriers and active efflux in bacteria. *Semin Cell Dev Biol*, **12**:215–223.
7) Tseng TT, Gratwick KS, Kollman J, Park D, Nies DH, Goffeau A, Saier MH, Jr (1999) The RND permease superfamily: an ancient, ubiquitous and diverse family that includes human disease and development protein. *J Mol Microbiol Biotechnol,* **1**:107–125.
8) Balganesh M, Kuruppath S, Marcel N, Sharma S (2010) Rv1218c, an ABC transporter of *Mycobacterium tuberculosis* with implications in drug discovery. *Antimicrob Agents Chemother*, **54**:5167–5172.

9) Kumar N, Radhakrishnan A, Wright CC, Chou TH, Lei HT, Bolla JR, Tringides ML, Rajashankar KR, Su CC, Purdy GE, Yu EW. Crystal Structure of the transcriptional regulator Rv1219c of *Mycobacterium tuberculosis* (2014). *Protein Sci.,* **23**: 423-432. doi: 10.1002/pro.2424.

10) Ramos J. L., Martinez-Bueno M., Molina-Henares A. J., Teran W., Watanabe K., Zhang X., et al. (2005) The TetR family of transcriptional repressors. Microbiol. *Mol. Biol. Rev*., **69**:326–356.

11) Cuthbertson L., Nodwell J. R. (2013). The TetR family of regulators. *Microbiol. Mol. Biol. Rev.,* **77**:440–475.

12) Mahenthiralingam, E., Urban, T. A. & Goldberg, J. B. The multifarious, multireplicon *Burkholderia cepacia* complex. *Nat Rev Microbiol*, **3**:144-156, doi:10.1038/nrmicro1085 (2005).

13) Malott, R. J., Steen-Kinnaird, B. R., Lee, T. D. & Speert, D. P. Identification of hopanoid biosynthesis genes involved in polymyxin resistance in *Burkholderia multivorans*. *Antimicrob Agents Chemother*, **56**:464-471, doi:10.1128/aac.00602-11 (2012).

14) Malott, R. J. et al. Fosmidomycin decreases membrane hopanoids and potentiates the effects of colistin on *Burkholderia multivorans* clinical isolates. *Antimicrob Agents Chemother*, **58**:5211-5219, doi:10.1128/aac.02705-14 (2014).

15) Schmerk, C. L., Bernards, M. A. & Valvano, M. A. Hopanoid production is required for low-pH tolerance, antimicrobial resistance, and motility in *Burkholderia cenocepacia. J Bacteriol*, **193**:6712-6723, doi:10.1128/jb.05979-11 (2011).

16) Ourisson, G., Rohmer, M. & Poralla, K. Prokaryotic hopanoids and other polyterpenoid sterol surrogates. *Annu Rev Microbiol*, **41**:301-333 (1987).

17) Mahato, S. B. & Sen, S. Advances in triterpenoid research, 1990-1994. *Phytochemistry*, **44**:1185-1236 (1997).

18) Saenz, J. P. et al. Hopanoids as functional analogues of cholesterol in bacterial membranes. *Proc Natl Acad Sci* (USA) **112**:11971-11976, doi:10.1073/pnas.1515607112 (2015).

19) Welander, P. V. et al. Hopanoids play a role in membrane integrity and pH homeostasis in *Rhodopseudomonas palustris* TIE-1. *J Bacteriol*, **191**:6145-6156, doi:10.1128/jb.00460-09 (2009).

20) Tseng, T. T. et al. The RND permease superfamily: an ancient, ubiquitous and diverse family that includes human disease and development proteins. *J Mol Microbiol Biotechnol*, **1**:107-125 (1999).

21) Doughty, D. M. et al. The RND-family transporter, HpnN, is required for hopanoid localization to the outer membrane of *Rhodopseudomonas palustris* TIE-1. *Proc Natl Acad Sci* (USA) **108**, E1045-1051, doi:10.1073/pnas.1104209108 (2011).

22) Ruiz-Palacios GM (2007). The health burden of *Campylobacter* infection and the impact of antimicrobial resistance: Playing chicken. *Clin Infect Dis*, **44**:701–703.

23) Lin J, Michel LO, Zhang Q (2002). CmeABC functions as a multidrug efflux system in *Campylobacter jejuni*. *Antimicrob Agents Chemother*, **46**:2124–2131.

24) Pumbwe L, Piddock LJ (2002). Identification and molecular characterisation of CmeB, a *Campylobacter jejuni* multidrug efflux pump. *FEMS Microbiol Lett*, **206**:185–189.

25) Luo N, Sahin O, Lin J, Michel LO, Zhang Q (2003) In vivo selection of Campylobacter isolates with high levels of fluoroquinolone resistance associated with gyrA mutations and the function of the CmeABC efflux pump. *Antimicrob Agents Chemother*, **47**:390–394.

26) Tseng TT, Gratwick KS, Kollman J, Park D, Nies DH, Goffeau A, Saier MH Jr (1999) The RND permease superfamily: An ancient, ubiquitous and diverse family that includes human disease and development protein. *J Mol Microbiol Biotechnol*, **1**:107–125.

27) Murakami S, Nakashima R, Yamashita E, Yamaguchi A (2002) Crystal structure of bacterial multidrug efflux transporter AcrB. *Nature,* **419**:587–593.

28) Murakami S, Nakashima R, Yamashita E, Matsumoto T, Yamaguchi A (2006) Crystal structures of a multidrug transporter reveal a functionally rotating mechanism. *Nature*, **443**:173–179.

29) Seeger MA, Schiefner A, Eicher T, Verrey F, Dietrichs K, Pos KM (2006) Structural asymmetry of AcrB trimer suggests a peristaltic pump mechanism. *Science*, **313**:1295–1298.

30) Sennhauser G, Amstutz P, Briand C, Storchengegger O, Grütter MG (2007) Drug export pathway of multidrug exporter AcrB revealed by DARPin inhibitors. *PLoS Biol,* **5**:e7.

31) Yu EW, McDermott G, Zgruskaya HI, Nikaido H, Koshland DE, Jr (2003) Structural basis of multiple drug binding capacity of the AcrB multidrug efflux pump. *Science*, **300**:976–980.

32) Yu EW, Aires JR, McDermott G, Nikaido H (2005) A periplasmic-drug binding site of the AcrB multidrug efflux pump: A crystallographic and site-directed mutagenesis study. *J Bacteriol*, **187**:6804–6815.

33) Sennhauser G, Bukowska MA, Briand C, Grütter MG (2009) Crystal structure of the multidrug exporter MexB from *Pseudomonas aeruginosa*. *J Mol Biol*, **389**:134–145.

34) Koronakis V, Sharff A, Koronakis E, Luisi B, Hughes C (2000) Crystal structure of the bacterial membrane protein TolC central to multidrug efflux and protein export. *Nature,* **405**:914–919.

35) Akama H, Kanemaki M, Yoshimura M, Tsukihara T, Kashiwag T, Yoneyama H, Narita S, Nakagawa A, Nakae T (2004) Crystal structure of the drug discharge outer membrane protein, OprM, of *Pseudomonas aeruginosa*. *J Biol Chem*, **279**:52816–52819.

36) Mikolosko J, Bobyk K, Zgurskaya HI, Ghosh P (2006) Conformational flexibility in the multidrug efflux system protein AcrA. *Structure*, **14**:577–587.

37) Akama H, Matsuura T, Kashiwag S, Yoneyama H, Narita S, Tsukihara T, Nakagawa A, Nakae T (2004) Crystal structure of the membrane fusion protein, MexA, of the multidrug transporter in *Pseudomonas aeruginosa*. *J Biol Chem*, **279**:25939–25942.

38) Higgins MK, Bokma E, Koronakis E, Hughes C, Koronakis V (2004) Structure of the periplasmic component of a bacterial drug efflux pump. *Proc Natl Acad Sci* (USA), **101**:9994–9999.

39) Symmons M, Bokma E, Koronakis E, Hughes C, Koronakis V (2009) The assembled structure of a complete tripartite bacterial multidrug efflux pump. *Proc Natl Acad Sci* (USA), **106**:7173–7178.

40) Su CC, Radhakrishnan A, Kumar N, Long F, Bolla JR, Lei HT, Delmar JA, Do SV, Chou TH, Rajashankar KR, Zhang Q, Yu EW. Crystal structure of the *Campylobacter jejuni* CmeC outer membrane channel (2014). *Protein Sci.*, **23**: 954-961. doi:10.1002/pro.2478.

41) Delmar JA, Su CC, Yu EW (2014). Bacterial multidrug efflux transporters. *Annu. Rev. Biophys*, **43**, 93-117.

# CHAPTER 2. CRYSTAL STRUCTURE OF THE TRANSCRIPTIONAL REGULATOR RV1219C OF *MYCOBACTERIUM TUBERCULOSIS*

A paper published in *Protein Sci.* (2014), 23: 423-432. doi: 10.1002/pro.2424.

Nitin Kumar[1,ψ], Abhijith Radhakrishnan[1,ψ], Catherine C. Wright[2], Tsung-Han Chou[3], Hsiang-Ting Lei[1], Jani Reddy Bolla[1], Marios L. Tringides[1], Kanagalaghatta R. Rajashankar[4], Chih-Chia Su[3], Georgiana E. Purdy[2], and Edward W. Yu[1,3*]

[1]Department of Chemistry, Iowa State University, Ames, IA 50011, USA

[2]Department of Molecular Microbiology and Immunology, Oregon Health and Sciences University, Portland, OR 97239, USA

[3]Department of Physics and Astronomy, Iowa State University, Ames, IA 50011, USA

[4]NE-CAT and Department of Chemistry and Chemical Biology, Cornell University, Bldg. 436E, Argonne National Laboratory, 9700 S. Cass Avenue, Argonne. IL 60439, USA

[ψ]N.K. and A.R. contributed equally to this work.

* To whom correspondence should be addressed. E-mail: ewyu@iastate.edu

## Abstract

The Rv1217c-Rv1218c multidrug efflux system, which belongs to the ATP-binding cassette (ABC) superfamily, recognizes and actively extrudes a variety of structurally unrelated toxic chemicals and mediates the intrinsic resistance to these antimicrobials in *Mycobacterium tuberculosis*. The expression of Rv1217c-Rv1218c is controlled by the TetR-like transcriptional regulator Rv1219c, which is encoded by a gene immediately upstream of *rv1218c*. To elucidate the structural basis of Rv1219c regulation, we have determined the crystal structure of Rv1219c, which reveals a dimeric two-domain molecule with an entirely helical architecture similar to members of the TetR family of transcriptional regulators. The N-terminal domains of the Rv1219c dimer are separated by a large center-to-center distance of 64 Å. The C-terminal domain of each protomer possesses a large cavity. Docking of small compounds to Rv1219c suggests that this large cavity forms a multidrug binding pocket, which can accommodate a variety of structurally unrelated antimicrobial agents. The internal wall of the multidrug binding site is surrounded by seven aromatic residues, indicating that drug binding may be governed by aromatic stacking interactions. In addition, fluorescence polarization reveals that Rv1219c binds drugs in the micromolar range.


## Introduction

Tuberculosis (TB) caused by *Mycobacterium tuberculosis*, is responsible for the death of approximately 2 million people each year and remains one of the deadlist diseases.[1,2] Standard treatment of TB requires 6-9 months with multiple antibiotics.[3] Noncompliance to this lengthy regimen results in relapses and selects for multidrug resistant (MDR) and extensively drug resistant (XDR) strains. MDR-TB are defined as strains that are resistant to at least the front-line antibiotics isoniazid and rifampicin, and XDR-TB is defined as resistant to rifampicin, isoniazid, fluoroquinolones, and at least one of the injectible second-line drugs.

Totally drug resistant (TDR)-TB was recently identified, indicating that even second-line drugs can be misused and become ineffective.[4-8] Combined, the emergence of drug-resistant TB complicates treatment, poses a significant risk to global public health, and challenges our expectation for TB control and elimination.

Recent research indicates that multidrug resistance of *M. tuberculosis* is linked to constitutive or inducible expression of multidrug efflux pumps.[9] Drug efflux pumps of bacteria have been categorized into five basic families: the ATP-binding cassette (ABC), resistance-nodulation-division (RND), multidrug and toxic compound extrusion (MATE), major facilitator (MF) and small multidrug resistance (SMR) families.[10] In Gram-negative bacteria, efflux systems of the RND superfamily play major roles in the intrinsic and acquired tolerance of antibiotics and noxious chemicals.[11] They are key mechanisms by which these pathogens survive in the presence of a variety of structurally unrelated, toxic compounds unfavorable for their survival. However, the ABC-type efflux transporters are not commonly linked to multidrug resistance. In *M. tuberculosis*, the ABC transporters Rv1217c-Rv1218c[12] and Rv0194[13] are among the very few efflux proteins involved in resistance to structurally diverse antimicrobials.

Roughly 2.5% of the *M. tuberculosis* H37Rv genome encodes transport proteins of the ABC superfamily, but only a few of these transporters have been characterized. Recent work demonstrated that the ABC-type Rv1217c-Rv1218c efflux system functions as a multidrug efflux pump, extruding a wide range of structurally unrelated drugs, including novobiocins, pyrazolones, biarylpiperazines, bisanilinopyrimidines, pyrroles and pyridones.[12] Our work is focused on elucidating how *M. tuberculosis* drug efflux systems are regulated. We previously determined the crystal structure of the Rv3066 efflux regulator,[14] which controls the expression of the Mmr efflux pump.[15] We report here the crystal structure of the Rv1219c regulator, which represses the transcriptional regulation of the Rv1217c-Rv1218c multidrug efflux transport

system. The *rv1219c* gene is the first gene of the Rv1217c-Rv1218c operon and encodes a 212 amino acid protein that shares sequence homology to members of the TetR family of transcriptional repressors. Our data suggest that Rv1219c is a multidrug binding protein that interacts with a variety of toxic aromatic compounds, such as bis-quinolinium cyclophanes, phosphoramidites, porphyrins and pyridazines.

## Results

### Overall structure of Rv1219c

The crystal structure of the *M. tuberculosis* Rv1219c transcriptional regulator was determined to a resolution of 2.99 Å using single isomorphous replacement with anomalous scattering (Table S1 and Fig. S1), revealing that only one Rv1219c molecule is present in the asymmetric unit. However, a dimeric arrangement of the regulator was found by applying a two-fold crystallographic symmetry operator (Fig. 1). As a TetR family of regulators, Rv1219c consists of two functional motifs: the N-terminal DNA-binding and C-terminal ligand-binding domains. Each subunit of Rv1219c is composed of 10 helices (α1-α10 and α1′-α10′, respectively). The helices of Rv1219c are designated numerically from the N-terminus as α1 (7-23), α2 (29-36), α3 (40-47), α4 (50-74), α5 (78-86), α6 (92-104), α7 (108-130), α8 (139-160), α9 (166-188) and α10 (194-206). In this arrangement, the smaller N-terminal domain includes helices α1 through α3 and the N-terminal end of α4 (residues 50-60), with α2 and α3 forming a typical helix-turn-helix motif. However, the larger C-terminal domain comprises the C-terminal end of helices α4 (residues 61-74) through α10, and helices α8, α9 and α10 are involved in the dimerization of the regulator.

**N-terminal domain**

The smaller N-terminal domain of Rv1219c shares considerably high sequence and structural similarities with the other TetR family members.[16] This is evident through protein sequence alignment that residues 7-60 of Rv1219c possess 25%, 24% and 31% amino acid identity to TetR,[17] QacR[18] and Rv3066,[14] respectively. In addition, superimposition of the Cα atoms of this N-terminal region, between residues 7 and 60, with those of AcrR[19] and Rv3066[14] results in overall rms deviations of 3.1 Å and 3.2 Å.

Perhaps, the most striking difference between the structures of Rv1219c and other TetR members is its large center-to-center distance, which is approximately 64 Å, between the two N-termini of the dimer (Fig. 1). This center-to-center distance is by far the longest among all known structures of the TetR-family regulators. The corresponding distances between the two recognition helices of the DNA-binding domains are 35 Å, 39 Å and 42 Å in the apo forms of TetR,[17] QacR[18] and AcrR.[19] Given that the separation between two successive major grooves of a B-form DNA is 34 Å, the large center-to-center distance of Rv1219c may allow this regulator to span three consecutive major grooves of the promoter DNA.

**C-terminal domain**

The C-terminal domain of Rv1219c consists of six α helices (α4 – α10), with helices α4, α5, α7, α8 and α9 forming an antiparallel five-helix bundle (Fig. 1). Like QacR, the dimerization surface mainly comprises helices α8 and α9, although helices α6 and α7 are also involved in the formation of the dimer. These helices make contacts with their counterparts to stabilize the dimerization. It should be noted that helix α10 of the C-terminal end of Rv1219c forms a long arm feature. This feature is unique in Rv1219c and was not found in other members of the TetR family. The elongated helical arm extends its length to the next subunit of the regulator and is anchored into the deep groove created by helices α5′ and α9′.

Presumably, this long arm and deep groove within the dimer are engaged to generate an interlocking system, securing the dimerization state of Rv1219c. The interlocking system may also allow the two N-terminal DNA-binding domains of the dimer to shift away from each other while still maintaining the dimeric form of the regulator. Although the C-terminal region displays no primary sequence conservation among members of the TetR family, the overall structure of the C-terminal domain of Rv1219c exhibits topological similarity to those of AcrR,[19] Rv3066,[14] EthR,[20,21] QacR[18] and CmeR.[22]

The crystal structure of Rv1219c also revealed that the C-terminal α-helical bundle of each subunit of the regulator forms a large internal cavity, with an internal volume of ~802 $Å^3$. Superimposition of the C-terminal domain of Rv1219c with that of QacR indicates that this large internal cavity overlaps with the multidrug binding pocket of QacR.[18] Thus, this cavity, assembled by helices α4-α9, presumably creates a substrate-binding site of the regulator. The interior of the cavity is surrounded by several aromatic residues, including W81, Y91, W113, Y123, F154, Y174 and Y186 (Fig. 2). These residues may interact with the bound substrate via aromatic stacking and hydrophobic interactions.

**Electrophoretic mobility shift assays (EMSA)**

The organization of the genetic locus containing the *rv1219c* gene is depicted in Figure 3A. Based on the genetic organization and preliminary ChIPSeq data from the TB Systems Biology Consortium, it was likely that Rv1219c regulated itself and downstream genes via binding of multiple sites. To demonstrate direct transcriptional regulation, we performed electrophoretic mobility shift assays (EMSA) using probes that comprised the intergenic region upstream of *rv1219c* and intragenic regions immediately upstream of the *rv1218c* gene that corresponded to additional ChIP-seq peaks (Fig. 3A). We observed a concentration-dependent shift of the Rv1219c probe and the two Rv1218c probes (Fig. 3B). Therefore, Rv1219c directly

regulates expression of Rv1219c and the Rv1217c-Rv1218c transporter. The affinity of Rv1219c for the probe encompassing the *rv1219c* promoter was greatest, shifting completely upon addition of 1 μM Rv1219c. The Rv1218-1 and Rv1218-2 probes did not completely shift even upon addition of 10 μM Rv1219c. Rv1219c bound the Rv1218-2 probe better than the Rv1218-1 probe, suggesting that high-, medium- and low-affinity binding sites exist. We identified indirect repeats in each of the probes that are likely binding sequences for Rv1219c (Fig. 3C). To demonstrate the minimal binding motif for Rv1219c, 74 bp oligonucleotide duplexes corresponding to the indirect repeat encompassed by probe Rv1219c were synthesized (Fig. 3D). This probe shifted upon addition of purified Rv1219c protein. A mutated 74-mer oligo was also synthesized with mutations within the indirect repeat. The mutated probe shifted with reduced efficiency compared to the wild type probe (Fig. 3D). Combined these data provide strong evidence that Rv1219c recognizes the indirect repeat in the Rv1219c promoter (green highlight, Fig. 3B). Our EMSA data suggests that Rv1219c regulates its own expression and the *rv1219c* operon primarily through the high-affinity binding site highlighted in green in Figure 2C. The additional medium and low-affinity binding sites highlighted in yellow and blue in Figure 3C, respectively, allow Rv1219c to further modulate the expression of *rv1218c*.

**Rv1219c-DNA interaction**

The binding affinity of the 58-bp DNA sequence (in Fig. 3C, green) within the *rv1219c* promoter region for the Rv1219c regulator was determined using isothermal titration calorimetry (ITC), which obtained the binding affinity constant, $K_A$, of $1.2 \pm 0.1 \times 10^6$ $M^{-1}$.

The enthalpic ($\Delta H$) and entropic ($\Delta S$) contributions for this binding are 4.8 ± 0.1 kcal/mol and 44.1 cal•mol•deg$^{-1}$ (Fig. 4). Interestingly, the molar ratio for this binding reaction based on ITC is one Rv1219c dimer per ds-DNA.

**Rv1219c-drug interactions**

The Rv3066 multidrug efflux regulator[14] binds several dyes, fluorescence polarization was used to examine if Rv1219c can also bind these dyes, including rhodamine 6G, ethidium and safranin O. We found that Rv1219c interacts with rhodamine 6G, ethidium and safranin O with $K_D$ values of 4.6 ± 0.5, 32.4 ± 7.4 μM and 42.4 ± 7.6 μM, respectively (Figs. 5 and S2). These data also suggest that the Rv1219c protein binds these molecules with a simple binding stoichiometry of 1:1 protomer-to-drug molar ratio. Further study is needed to confirm this protein-to-drug binding ratio.

**Virtual ligand library screening**

To elucidate the nature of protein-ligand interactions in the Rv1219c regulator virtual ligand screening was performed using the large internal cavity formed by the C-terminal domain of Rv1219c as a substrate binding cavity. We used AutoDock Vina[23] to screen small molecules in the DrugBank[24] and ZINC[25] libraries. Vina[23] utilizes the iterated local search global optimizer algorithm, which results in predicted binding free energies for these compounds ranging from -13.8 to +20 kcal/mol. Of the 70,000 screened compounds, the best predicted substrate for Rv1219c was the bisquinolinum cyclophane compound UCL 1684 ditrifluoroacetate, which is a potassium channel blocker, with a predicted binding free energy of -13.3 kcal/mol. Table S2 lists the top 11 substrates, which have the lowest predicted binding free energies, for the Rv1219c regulator.

Since our fluorescence polarization data showed that Rv1219c binds rhodamine 6G, ethidium and safranin O, Vina[23] was also used to examine how these dyes interact with the regulator. These dyes also bind within the multidrug binding pocket of the protein. The predicted binding free energies for these dyes are -8.3, -8.1 and -7.8 kcal/mol, respectively. These free energies suggest that Rv1219c binds the substrates listed in Table S2 more strongly than these dyes. Interestingly, Vina suggests that Rv1219c uses the same binding mode to interact with these drugs and dyes.

## Discussion

With the rising incidence of MDR-TB, it is increasingly important to understand the mechanisms underlying resistance to multiple antibiotics in this pathogen. The crystal structure of Rv1219c provides direct information about how this regulator interacts with its inducing ligands. The surface of the Rv1219c multidrug binding cavity has several familiar aromatic and hydrophobic residues that are critically important in other multidrug binding proteins. These residues produce a hydrophobic environment for substrate binding in the C-terminal regulatory domain.

AutoDock Vina[23] was used to study how Rv1219c binds a variety of drugs, and demonstrated that the large cavity of the multidrug binding site of each Rv1219c monomer can accommodate many different classes of drugs (Fig. 2). Surprisingly, the top substrate for Rv1219c was the positively charged heterocyclic bisquinolinium cyclophane UCL 1684 potassium channel blocker. The next top three substrates belong to the classes of phosphoramidite, tetrapyrrole and organophosphorous, suggesting that these small molecules may also be the substrates of the Rv1217c-Rv1218c multidrug efflux pump. These top compounds are either cationic or neutral molecules. In each case, the bound drug was completely buried within the multidrug binding site of the Rv1219c protomer, and strong

aromatic stacking interaction was observed between the bound drug and regulator. The docking study also indicates that residues I63, L73, W81, Y91, Y123, L146, F154, Y174, Y186 are important for providing hydrophobic and aromatic stacking interactions with these drugs.

Since fluorescence polarization experiments demonstrate that Rv1219c binds rhodamine 6G, ethidium and safranin O in the micromolar range, we also used Vina[23] to model the interactions between these positively charged dyes and the regulator. The binding affinities of these dyes by Rv1219c are much weaker than those of the top Rv1219c substrates. However, all these dyes and top Rv1219c substrates are bound within the same multidrug binding site with a similar binding mode, suggesting that the process of induction by these ligands is similar.

A distinguishing feature of multidrug binding proteins that bind cationic drugs is the presence of buried acidic glutamates or aspartates in the ligand binding pockets. This was clearly demonstrated by the structures of the QacR[18,26] and Rv3066[14] regulators. A similar characteristic for the TetR-family regulators that recognize negatively charged antimicrobials has also been observed with TtgR[27] and CmeR.[28] In this case, positively charged histidines or lysines within the ligand-binding pockets are critical for the binding. In the case of Rv1219c, the predicted substrates are either neutral or positively charged. Thus, we expected a buried acidic residue was needed to participate in binding the substrate. Unexpectedly, the binding crevice of Rv1219c does not contain any glutamate or aspartate. The only charged residue found within the multidrug binding cavity is the cationic lysine K69 (Fig. 2). Based on the docking results with the positively charged UCL 1684 and neutral phthalocyanine ligands, this lysine residue is within 4.8 Å and 3.1 Å away from these bound ligands. It is likely that K69 is responsible for providing electrostatic interaction for the binding. However, neutralization of the formal charge of the bound ligand may not be a prerequisite for drug recognition.

Intriguingly, there are three methionines, M85, M95 and M116, seemingly coordinating with each other within this hydrophobic binding cavity. These three methionines form a triad, similar to the periplasmic heavy metal binding site of the CusA efflux pump.[29-31] It is possible that these three methionines may cooperate to create a metal binding site within the multidrug binding cavity. The crystal structures of Rv1219c bound with a variety of ligands will be crucial for further understanding of how this regulator recognizes multiple antimicrobials. The structural similarity of the N-terminal domains of members of the TetR family suggests a similar mode of interaction with target DNAs. It is known that the separation between two consecutive major grooves of *B*-DNA is 34 Å. Based on the apo structure of Rv1219c, the two DNA recognition regions of the dimer are separated by 64 Å. Therefore, it is possible that the Rv1219c dimer is capable of spanning three successive major grooves of the double helix when it binds its IR. Rv1219c likely represses the transcription of *rv1217c-rv1218c* by binding to the high-affinity IR sequence in the promoter region of the efflux operon and the lower affinity sites immediately upstream of *rv1218c*. It is striking that the promoter probe contains a perfect IR that spans 58 bp (Fig. 3C, green). MEME analysis of the three probes defined a consensus binding motif corresponding to this IR that was also present in the Rv1218-2 probe. However, the putative binding site in the Rv1218-2 probe is degenerate (CGATCTGACCGCGCACGCCAGG), which may explain reduced binding of Rv1219c to the Rv1218-2 probe relative to Rv1219 probe in the EMSAs.

The control of TB has been compromised by the increasing proportion of infections due to drug-resistant strains, which are growing at alarming rate. Thus, there is a need to develop new approaches for the treatment of TB. Elucidating the structures and functions of efflux pumps and regulators of *M. tuberculosis* should enable researchers to explore novel avenues to combat the disease. It has been observed that the expression level of the Rv1217c-Rv1218c multidrug efflux pump is significantly increased in clinically isolated MDR-TB strains in

comparison with that of the wild-type H37Rv *M. tuberculosis*.[32] In this paper, we have reported the crystal structure of the Rv1219c regulator, which controls the expression level of Rv1217c-Rv1218c. It is hope that the availability of this crystal structure may allow us to rationally design agents that block the function of this regulator and diminish the expression of the multidrug efflux pump, which in turn heighten the sensitive of this pathogen to antimicrobials.

## Materials and Methods

### Cloning of *rv1219c*

The *rv1219c* ORF from genomic DNA of *M. tuberculosis* strain H37Rv was amplified by PCR using the primers 5′-CCATGGGCCGTTCAGCCGATCTGACC-3′ and 5′-GGATCCTCAGTGATGATGATGATGATGGCCGACATGTGCTTCTCC-3′. The corresponding PCR product was digested with *Nco*I and *Bam*HI, extracted from the agarose gel, and inserted into pET15b as described by the manufacturer (Merck KGaA, Darmstadt, Germany) to generate a product that encodes a Rv1219c recombinant protein with a 6xHis tag at the C-terminus (Rv1219c-$His_6$). The recombinant plasmid (pET15bΩ*rv1219c*) was transformed into DH5α cells and the transformants were selected on LB agar plates containing 100 μg/ml ampicillin. The presence of the correct *rv1219c* sequence in the plasmid construct was verified by DNA sequencing.

### Expression and purification of Rv1219c

Briefly, Rv1219c-$His_6$ was overproduced in *E. coli* BL21(DE3) cells carrying pET15bΩ*rv1219c*. Cells were grown in 6 L of Luria Broth (LB) medium with 100 μg/ml ampicillin at 37°C. When the $OD_{600}$ reached 0.5, the culture was treated with 1 mM isopropyl-β-D-thiogalactopyranoside (IPTG) to induce Rv1219c expression, and cells were harvested within 3 h. The collected bacterial cells were suspended in 100 ml ice-cold buffer containing

20 mM Na-HEPES (pH 7.2) and 200 mM NaCl, 10 mM $MgCl_2$ and 0.2 mg DNase I (Sigma-Aldrich). The cells were then lysed with a French pressure cell. Cell debris was removed by centrifugation for 45 min at 4°C and 20,000 rev/min. The crude lysate was filtered through a 0.2 μm membrane and was loaded onto a 5 ml Hi-Trap $Ni^{2+}$-chelating column (GE Healthcare Biosciences, Pittsburgh, PA) pre-equilibrated with 20 mM Na-HEPES (pH 7.5) and 250 mM NaCl. To remove unbound proteins and impurities, the column was first washed with six column volumes of buffer containing 50 mM imidazole, 250 mM NaCl, and 20 mM Na-HEPES (pH 7.5). The Rv1219c protein was then eluted with four column volume of buffer containing 300 mM imidazole, 250 mM NaCl, and 20 mM Na-HEPES (pH 7.5). The purity of the protein was judged using 12.5% SDS-PAGE stained with Coomassie Brilliant Blue. The purified protein was extensively dialyzed against buffer containing 100 mM imidazole, 250 mM NaCl, and 20 mM Na-HEPES (pH 7.5), and concentrated to 12 mg/ml.

For the SeMet-Rv1219c-$His_6$ protein expression, a 10 ml LB broth overnight culture containing *E. coli* BL21(DE3)/pET15bΩ*rv1219c* cells was transferred into 60 ml of LB broth containing 100 μg/ml ampicillin and grown at 37°C. When the $OD_{600}$ value reached 1.2, cells were harvested by centrifugation at 6000 rev/min for 10 min, and then washed two times with 10 ml of M9 minimal salts solution. The cells were re-suspended in 60 ml of M9 media and then transferred into a 6 L pre-warmed M9 solution containing 100 μg/ml ampicillin. The cell culture was incubated at 25°C with shaking. When the $OD_{600}$ reached 0.4, 100 mg/l of lysine, phenylalanine and threonine, 50 mg/l isoleucine, leucine and valine, and 60 mg/l of L-selenomethionine were added. The culture was induced with 1 mM IPTG after 15 min. Cells were then harvested within 15 h after induction. The procedures for purifying SeMet-Rv1219c were identical to those of the native protein.

**Crystallization of Rv1219c**

All crystals of the Rv1219c-$His_6$ were obtained using hanging-drop vapor diffusion. The Rv1219c crystals were grown at 18 $^oC$ in 24-well plates with the following procedures. A 2 μl protein solution containing 12 mg/ml Rv1219c protein in 20 mM Na-HEPES (pH 7.5), 250 mM NaCl and 100 mM imidazole was mixed with a 2 μl of reservoir solution containing 5% Jeffamine M-600, 0.1 M Na-citrate (pH 5.6) and 0.6 M NaCl. The resultant mixture was equilibrated against 500 μl of the reservoir solution. Crystals grew to a full size in the drops within two weeks. Typically, the dimensions of the crystals were 0.2 mm x 0.2 mm x 0.2 mm. Cryoprotection was achieved by raising the glycerol concentration stepwise to 25% with a 5% increment in each step. Crystals of the tungsten derivative was prepared by incubating the crystals of Rv1219c in solution containing 5% Jeffamine M-600, 0.1 M Na-citrate (pH 5.6), 0.6 M NaCl and 1 mM $(NH_4)_2W_6(\mu\text{-}O)_6(\mu\text{-}Cl)_6Cl_6$ for 24 hours at 25$^oC$.

**Data collection, structural determination and refinement**

All diffraction data were collected at 100K at beamline 24ID-E located at the Advanced Photon Source, using an ADSC Quantum 315 CCD-based detector. Diffraction data were processed using DENZO and scaled using SCALEPACK.[33] The crystals of Rv1219c belong to the space group *I*432 (Table S1). Based on the molecular weight of Rv1219c (23.18 kDa), the asymmetric unit is expected to contain one regulator protomer with a solvent content of 22.56%. The heavy-atom derivative was isomorphous with the native crystal (Table S1). Six tungsten cluster sites were identified using HySS as implemented in the PHENIX package.[34] Single isomorphous replacement with anomalous scattering was employed to obtain experimental phases using the program MLPHARE.[35,36] The resulting phases were subjected to density modification by RESOLVE[37] using the native structure factor amplitudes. Density modified phases were good enough to allow us to visualize the secondary structural features of

the molecule. These phases were then subjected to density modification and phase extension to 2.99 Å-resolution using the program RESOLVE.[37] The resulting phases were of excellent quality that enabled tracing of most of the molecule. In addition, the selenomethionyl-substituted (SeMet) crystal data were used to help in tracing the molecules by anomalous difference Fourier maps where we could ascertain the proper registry of SeMet residues. The full-length Rv1219c protein consists of eight methionine residues and all of these eight selenium sites were identified in each protomer of the protein. After tracing the initial model manually using the program Coot,[38] the model was refined against the native data at 2.99 Å-resolution in PHENIX,[34] leaving 5% of reflections in Free-R set. Iterations of refinement using PHENIX[34] and CNS[39] and model building in Coot[38] lead to the current model, which consists 205 residues with excellent geometrical characteristics (Table S1).

**Electrophoretic mobility shift assays (EMSA)**

Rv1219c-$His_6$ was purified from *E. coli* lysates using Talon resin (Novagen). Probes were amplified from the H37Rv genome using the primers listed in Table S3. Synthetic probes were synthesized with the following sequences: WT-TAATTCGGCGAGCAGACGCAAAATCGCCCTGAACCGTGCGTTCCAGGGCGATTTTGCGTCTGCTCGGCAAAGTT; mutant-TAATTCGGTATACGCTACGAGCATCTATATGAACCGTGCGTTCTATACGCTACAGGGCGATTATAGGCAAAGTT. All probes were labeled with Digoxigenin using the Roche DIG Gel Shift kit. For EMSA analysis, 12 nM Dig-labeled probe and the indicated micromolar concentrations of protein were incubated for 45 minutes at room temperature in the Roche binding buffer modified by the addition of 0.25 mg/mL herring sperm DNA, and 0.75 μg/mL poly(d[I-C]). All reactions were resolved on a 6% native polyacrylamide gel in TBE buffer,

transferred to nylon membrane and DIG-labeled DNA-protein complexes detected following the manufacturer's recommendations. Chemiluminescent signals were acquired using an ImageQuant LAS 4000 (GE).

**Isothermal Titration Calorimetry**

We used ITC to examine the binding of the DNA sequence (highlighted in green in Fig. 3C) to the purified CmeR regulator. Measurements were performed on a VP-Microcalorimeter (MicroCal, Northampton, MA) at 25 $^{o}$C. Before titration, the protein was thoroughly dialyzed against buffer containing 10 mM Na-phosphate pH 7.2 and 100 mM NaCl. The protein concentration was determined using the Bradford assay. The protein sample was then adjusted to a final concentration of 10 μM. DNA solution consisting of 200 μM 58-bp ds-DNA in 10 mM Na-phosphate pH 7.2 and 100 mM NaCl was prepared as the titrant. The protein and ligand samples were degassed before they were loaded into the cell and syringe. Binding experiments were carried out with the protein solution (1.5 ml) in the cell and the DNA as the injectant. Ten microliter injections of the ligand solution were used for data collection. Injections occurred at intervals of 240 s, and the duration time of each injection was 10 s. Heat transfer (μcal/s) was measured as a function of elapsed time (s). The mean enthalpies measured from injection of the ligand in the buffer were subtracted from raw titration data before data analysis with ORIGIN software (MicroCal). Titration curves were fitted by a nonlinear least squares method to a function for the binding of a DNA to a macromolecule. Nonlinear regression fitting to the binding isotherm provided us with the equilibrium binding constant ($K_A = 1/K_D$) and enthalpy of binding ($\Delta H$). Based on the values of $K_A$, the change in free energy ($\Delta G$) and entropy ($\Delta S$) were calculated with the equation: $\Delta G = - RT \ln K_A = \Delta H - T\Delta S$, where $T$ is 273 K and $R$ is 1.9872 cal/K per mol. Calorimetry trials were also carried out

in the absence of Rv1219c in the same experimental conditions. No change in heat was observed in the injections throughout the experiment.

**Fluorescence polarization assay for ligand binding affinity**

Fluorescence polarization was used to determine the binding affinities of a variety of Rv1219c ligands, including rhodamine 6G, ethidium bromide and safranin O. The experiment was done using a ligand binding solution containing 10 mM Na-phosphate (pH 7.2), 100 mM NaCl and 1 μM ligand (rhodamine 6G, ethidium bromide or safranin O). The protein solution consisting of Rv1219c in 10 mM Na-phosphate (pH 7.2), 100 mM NaCl and 1 μM ligand (rhodamine 6G, ethidium bromide or safranin O) was titrated into the ligand binding solution until the polarization (P) was unchanged. As this is a steady-state approach, fluorescence polarization measurement was taken after a 5 min incubation for each corresponding concentration of the protein and bile acid to ensure that the binding has reached equilibrium. All measurements were performed at 25$^{o}$C using a PerkinElmer LS55 spectrofluorometer equipped with a Hamamatsu R928 photomultiplier. The excitation and emission wavelengths were 526 and 555 nm for rhodamine 6G, 483 and 620 nm for ethidium, and 520 and 587 nm for safranin O. Fluorescence polarization signal (in ΔP) was measured at the emission wavelength. Each titration point recorded was an average of 15 measurements. Data were analyzed using the equation, $P = \{(P_{bound} - P_{free})[protein]/(K_D + [protein])\} + P_{free}$, where P is the polarization measured at a given total protein concentration, $P_{free}$ is the initial polarization of free ligand, $P_{bound}$ is the maximum polarization of specifically bound ligand, and [protein] is the protein concentration. The titration experiments were repeated for three times to obtain the average $K_D$ value. Curve fitting was accomplished using the program ORIGIN (OriginLab Corporation, Northampton, MA).

**Virtual ligand screening using AutoDock Vina**

AutoDock Vina was used for virtual ligand screening of a variety of compounds. The docking area was assigned visually to cover the internal cavity of the Rv1219c monomer. A grid of 35 Å × 35Å × 35Å with 0.375 Å spacing was calculated around the docking area for all atom types presented in the DrugBank and ZINC libraries using AutoGrid. The iterated local search global optimizer algorithm was employed to predict the binding free energies for these compounds.

## Protein Data Bank accession code

Coordinates and structural factors for the structure of Rv1219c have been deposited at the RCSB Protein Data Bank with an accession code 4NN1.

## Acknowledgements

This work was supported by NIH Grants R01AI087840 (G.E.P.) and R01GM086431 (E.W.Y.). This work is based upon research conducted at the Northeastern Collaborative Access Team beamlines of the Advanced Photon Source, supported by award RR-15301 from the National Center for Research Resources at the National Institutes of Health. Use of the Advanced Photon Source is supported by the U.S. Department of Energy, Office of Basic Energy Sciences, under Contract No. DE-AC02-06CH11357. We are grateful to Louis Messerle at University of Iowa for providing us the $(NH_4)_2W_6(\mu\text{-}O)_6(\mu\text{-}Cl)_6Cl_6$ complex used in this study.

## References


1. Maartens G, Wilkinson RJ (2007) Tuberculosis. *The Lancet,* **370**:2030-2043.
2. World Health Organization (2010) Fact sheet no. 104: tuberculosis. Available at http://www.who.int/mediacentre/factsheets/fs104/en/index.html.
3. http://www.cdc.gov/tb/topic/treatment/default.htm.
4. Frieden TR, Sterling T, Pablos-Mendez A, Kilburn JO, Cauthen GM, Dooley SW (1993) The emergence of drug-resistant tuberculosis in New York City. *N Engl J Med*, **328**:521-556.
5. Pillay M, Sturm AW (2007) Evolution of the extensively drug-resistant F15/LAM4/KZN strain of Mycobacterium tuberculosis in KwaZulu-Natal, South Africa. *Clin Infect Dis,* **45**:1409-1414.
6. Goldman RC, Plumley KV, Laughon BE (2007) The evolution of extensively drug resistant tuberculosis (XDR–TB): history, status and issues for global control. *Infect Disord Drug Targets,* **7**:73-91.
7. Udwadia ZF, Amale RA, Rodrigues C (2012) Totally drug-resistant tuberculosis in India. *Clin Infect Dis,* **54**:579-581.
8. Iseman MD (1993) Treatment of multidrug-resistant tuberculosis. *N Engl J Med*, **329**:784–791.
9. Nikaido H (2001) Preventing drug access to targets: cell surface permeability barriers and active efflux in bacteria. *Semin Cell Dev Biol*, **12**:215-223.
10. Li XZ, Nikaido H (2004) Efflux-mediated drug resistance in bacteria. *Drugs*, **64**:159-204.
11. Tseng TT, Gratwick KS, Kollman J, Park D, Nies DH, Goffeau A, Saier MH Jr (1999) The RND permease superfamily: an ancient, ubiquitous and diverse family that includes human disease and development protein. *J Mol Microbiol Biotechnol*, **1**:107-125.

12. Balganesh M, Kuruppath S, Marcel N, Sharma S (2010) Rv1218c, an ABC transporter of *Mycobacterium tuberculosis* with implications in drug discovery. *Antimicrob Agents Chemother*, **54**:5167-5172.

13. Danilchanka O, Mailaender C, Niederweis M (2008) Identification of a novel multidrug efflux pump of *Mycobacterium tuberculosis*. *Antimicrob Agents Chemother*, **52**:5203-5211.

14. Bolla JR, Do SV, Long F, Dai L, Su CC, Lei HT, Chen X, Gerkey JE, Murphy DC, Rajashankar KR, Zhang Q, Yu EW (2012) Structural and functional analysis of the transcriptional regulator Rv3066 of Mycobacterium tuberculosis. *Nucleic Acids Res*, **40**:9340-9355.

15. De Rossi E, Branzoni M, Cantoni R, Milano A, Riccardi G, Ciferri O (1998) *mmr*, a Mycobacterium tuberculosis gene conferring resistance to small cationic dyes and inhibitors. *J Bacteriol*, **180**:6068-6071.

16. Ramos JL, Martinez-Bueno M, Molina-Henares AJ, Teran W, Watanabe K, Zhang XD, Gallegos MT, Brennan R, Tobes R (2005) The TetR family of transcriptional repressors. *Microbiol Mol Biol Rev*, **69**:326-356.

17. Hinrichs W, Kisker C, Duvel M, Muller A, Tovar K, Hillen W, Saenger W (1994) Structure of the Tet repressor-tetracycline complex and regulation of antibiotic resistance. *Science,* **264**:418-420.

18. Schumacher MA, Miller MC, Brennan RG (2001) Structural mechanisms of QacR induction and multidrug recognition. *Science*, **294**:2158-2163.

19. Li M, Gu R, Su CC, Routh MD, Harris KC, Jewell ES, McDermott G, Yu EW (2007) Crystal structure of the transcriptional regulator AcrR from *Escherichia coli*. *J Mol Biol*, **374**:591–603.

20. Dover LG, Corsino PE, Daniels IR, Cocklin SL, Tatituri V, Besra GS and Futterer K (2004) Crystal structure of the TetR/CamR family repressor *Mycobacterium tuberculosis* EthR implicated in ethionamide resistance. *J Mol Biol*, **340**:1095-1105.

21. Frenois F, Engohang-Ndong J, Locht C, Baulard A R, Villeret V (2004) Structure of EthR in a ligand bound conformation reveals therapeutic perspectives against tuberculosis. *Mol Cell*, **16**:301-307.

22. Gu R, Su CC, Shi F, Li M, McDermott G, Zhang Q, Yu EW (2007) Crystal Structure of the transcriptional regulator CmeR from *Campylobacter jejuni*. *J Mol Biol*, **372**:583–593.

23. Trott O, Olson AJ (2010) AutoDock Vina: Improving the speed and accuracy of docking with a new scoring function, efficient optimization, and multithreading. *J Comp Chem* **31**:455-461.

24. Knox C, Law V, Jewison T, Liu P, Ly S, Frolkis A, Pon A, Banco K, Mak C, Neveu V, Djoumbou Y, Eisner R, Guo AC, Wishart DS (2011). DrugBank 3.0: a comprehensive resource for 'omics' research on drugs. *Nucl Acids Res,* **39**: D1035-D1041.

25. Irwin JJ, Sterling T, Mysinger MM, Bolstad ES, Coleman RG (2012) ZINC: A Free Tool to Discover Chemistry for Biology. *J Chem Inf Model*, **52**:1757-1768.

26. Brooks BE, Piro KM, Brennan RG (2007) Multidrug-binding transcription factor QacR binds the bivalent aromatic diamidines DB75 and DB359 in multiple positions. *J. Am. Chem. Soc.*, **129**:8389-8395.

27. Alguel Y, Meng C, Terán W, Krell T, Ramos JL, Gallegos M-T, Zhang X (2007) Crystal structures of multidrug binding protein TtgR in complex with antibiotics and plant antimicrobials. *J Mol Biol*, **369**:829-840.

28. Lei HT, Shen Z, Surana P, Routh MD, Su CC, Zhang Q, Yu EW (2011) Crystal structures of CmeR-bile acid complexes from *Campylobacter jejuni*. *Prot Sci*, **20**:712-723.

29. Long F, Su CC, Zimmermann MT, Boyken SE, Rajashankar KR, Jernigan RL, Yu EW (2010) Crystal Structures of the CusA Efflux Pump Suggest Methionine-Mediated Metal Transport. *Nature*, **467**:484-488.

30. Su CC, Long F, Zimmermann MT, Rajashankar KR, Jernigan RL, Yu EW (2011) Crystal Structure of the CusBA Heavy-Metal Efflux Complex of *Escherichia coli*. *Nature*, **470**:558-562.

31. Su CC, Long F, Lei HT, Bolla JR, Do SV, Rajashankar KR, Yu EW (2012) Charged Amino Acids (R83, E567, D617, E625, R669, and K678) of CusA Are Required for Metal Ion Transport in the Cus Efflux System. *J Mol Biol*, **422**:429-441.

32. Wang K, Pei H, Huang B., Zhu X, Zhang J, Zhou B, Zhu L, Zhang Y, Zhou FF (2013) The expression of ABC efflux pump, Rv1217c-Rv1218c, and its association with multidrug resistance of *M. tuberculosis* in China. *Curr Microbiol*, **66**:222-226.

33. Otwinowski Z, Minor M (1997) Processing of X-ray diffraction data collected in oscillation mode. *Methods Enzymol*, **276**:307-326.

34. Afonine PV, Grosse-Kunstleve RW, Adams PD (2005) The Phenix refinement framework. CCP4 Newsletter 42: contribution 8.

35. Otwinowski Z (1991) MLPHARE, CCP4 Proc. 80 (Daresbury Laboratory, Warrington, UK).

36. Collaborative Computational Project No. 4 (1994) The CCP4 suite: programs for protein crystallography. *Acta Crystallogr. D*, **50**:760-763.

37. Terwilliger TC (2001) Maximum-likelihood density modification using pattern recognition of structural motifs. *Acta Cryst. D*, **57**:1755-1762.

38. Emsley P, Cowtan K (2004) Coot: Model-building tools for molecular graphics. *Acta Crystallog D,* **60**:2126-2132.

39. Brünger AT, Adams PD, Clore GM, DeLano WL, Gros P, Grosse-Kunstleve RW, Jiang JS, Kuszewski J, Nilges M, Pannu NS, Read RJ, Rice LM, Simonson T, Warren GL (1998) Crystallography & NMR system: A new software suite for macromolecular structure determination. *Acta Crystallog D*, **54**:905-921.

## Figures and captions

Figure 1. Structure of the *M. tuberculosis* Rv1219c regulator. (A) Ribbon diagram of a protomer of Rv1219c. The molecule is colored using a rainbow gradient from the N-terminus (blue) to the C-terminus (red). (B) Ribbon diagram of the Rv1219c dimer. Each subunit of Rv1219c is labeled with a different color (green and orange). The Figure was prepared using PyMOL (http://www.pymol.sourceforge.net).

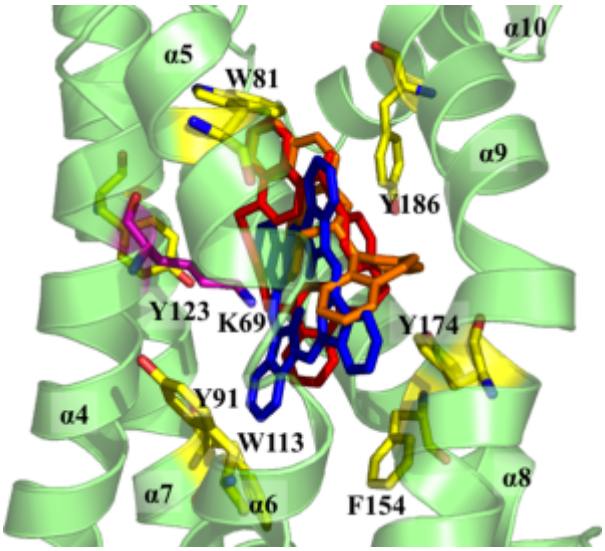


Figure 2. The C-terminal multidrug binding site. The seven aromatic residues (W81, Y91, W113, Y123, F154, Y174 and Y186) that surround the interior of the multidrug binding cavity of Rv1219c are in yellow sticks. The cationic residue K69, which is thought to be important for interacting with the bound drug, is in magenta stick. The top three Rv1219c substrates are also included (red, UCL 1684; orange, (*S*)-(+)-*N*-(3,5-Dioxa-4-phosphacyclohepta[2,1-*a*;3,4-*a*′]dinaphthalen-4-yl)-dibenzo[*b*,*f*]azepine; blue, phthalocyanine).

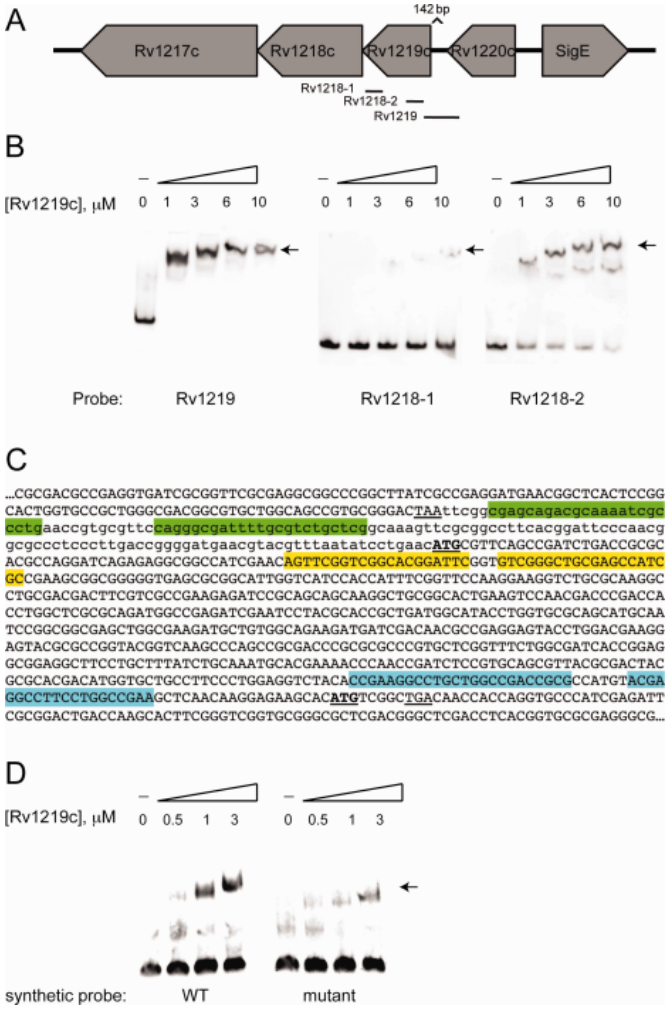


Figure 3. Rv1219c binds to promoter regions of *rv1219c* and upstream of the *rv1218c* gene. (A) A schematic depicting the DNA probes used in electrophoretic mobility shift assays (EMSAs) to examine the promoter region of *rv1219c* and *rv1218c*. (B) EMSAs were performed using 12 nM Dig-labeled probe and the indicated micromolar concentrations of protein. An arrow denotes the shifted probes. (C) The reverse complement sequence of *rv1219c-rv1218c* region. The stop codon of *rv1220c* is underlined, the start codons of *rv1219c* and *rv1218c* are bold and underlined. The 142 bp intergenic region between rv1220c and rv1219c is in lowercase, coding sequences are in upper case. Indirect repeats were identified in

each of the probes using the MEME algorithm. The high-affinity binding site in the *rv1219c* promoter probe is highlighted in green. The low-affinity Rv1219c binding motifs in the rv1218-1 and rv1218-2 probes are highlighted in blue and yellow, respectively. (D) EMSAs were performed using 12 nM Dig-labeled probe and the indicated micromolar concentrations of protein. An arrow denotes the shifted probes. Synthetic oligonucleotide duplexes comprising the high affinity binding site plus 8 nt on either side (74 bp total) were used as probes.

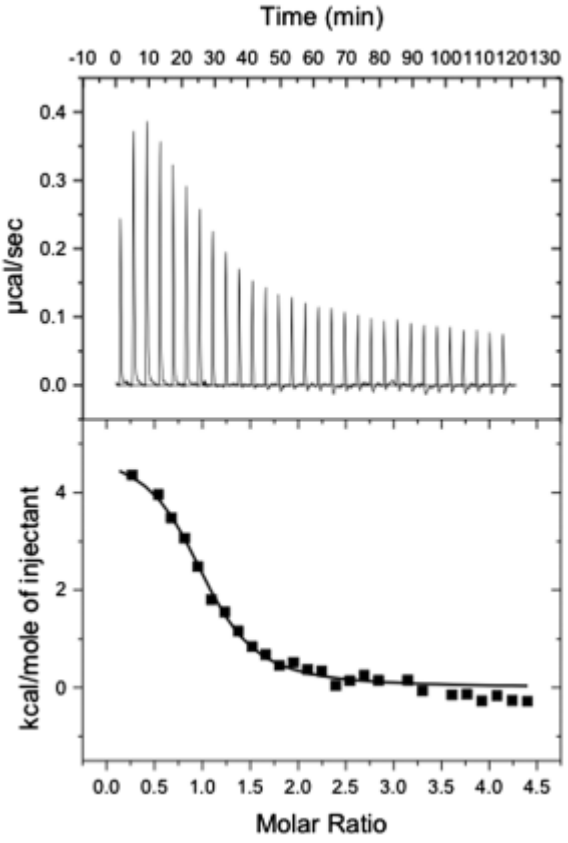


Figure 4. Representative isothermal titration calorimetry for the binding of the 58-bp DNA to Rv1219c regulator. (A) Each peak corresponds to the injection of 10 µl of 200 µM 58-bp DNA in buffer containing 10 mM Na-phosphate (pH 7.5) and 100 mM NaCl into the reaction

cell containing 10 μM Rv1219c in the same buffer. (B) Cumulative heat of reaction is displayed as a function of the injection number. The solid line is the least-square fit to the experimental data, giving a $K_A$ of 1.2 ± 0.1 x $10^6$ $M^{-1}$. The molar-to-molar ratio of dimeric Rv1219c:58-bp ds-DNA is 1:1.

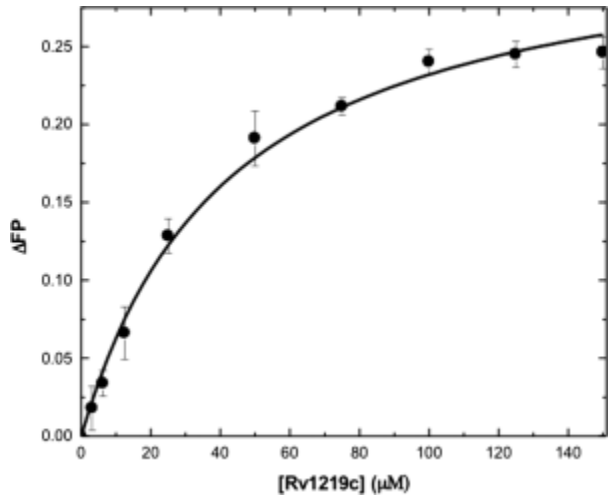


Figure 5. Representative fluorescence polarization of Rv1219c. The binding isotherm of Rv1219c with safranin O, showing a $K_D$ of 42.4 ± 7.6 μM. Fluorescence polarization is defined by the equation, FP = (V – H) / (V + H), where FP equals polarization, V equals the vertical component of the emitted light, and H equals the horizontal component of the emitted light of a fluorophore when excited by vertical plane polarized light. FP is a dimensionless entity and is not dependent on the intensity of the emitted light or on the concentration of the fluorophore. mP is related to FP, where 1 mP equals one thousandth of a FP.

# Supplemental Materials

## Supplemental Figures

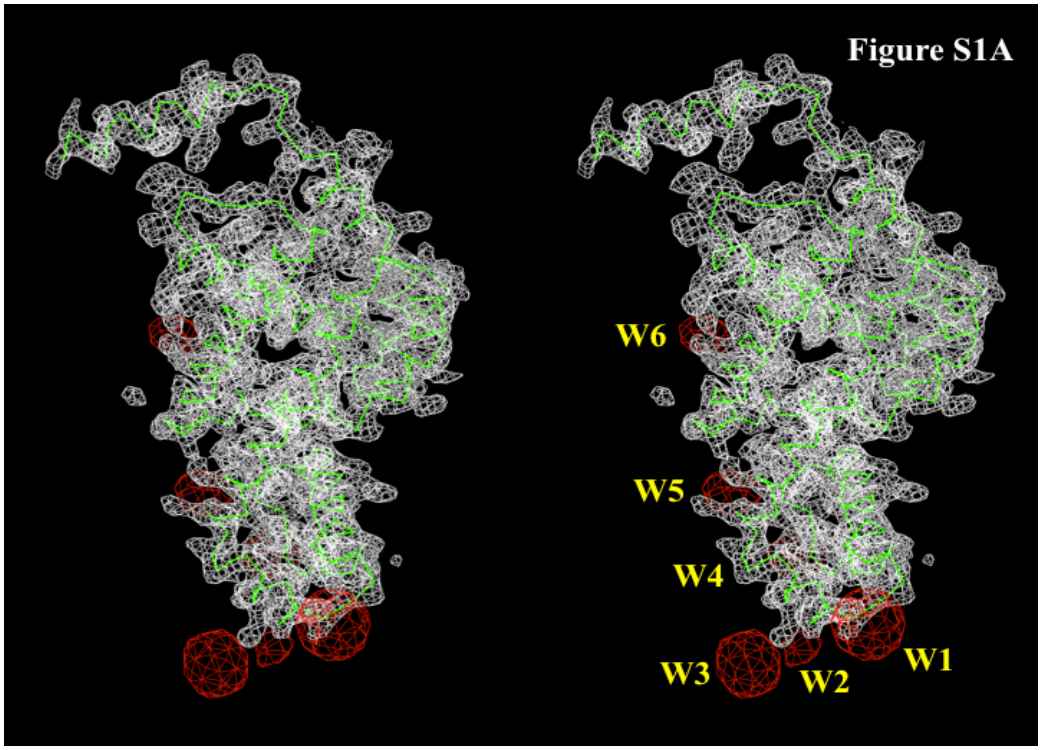


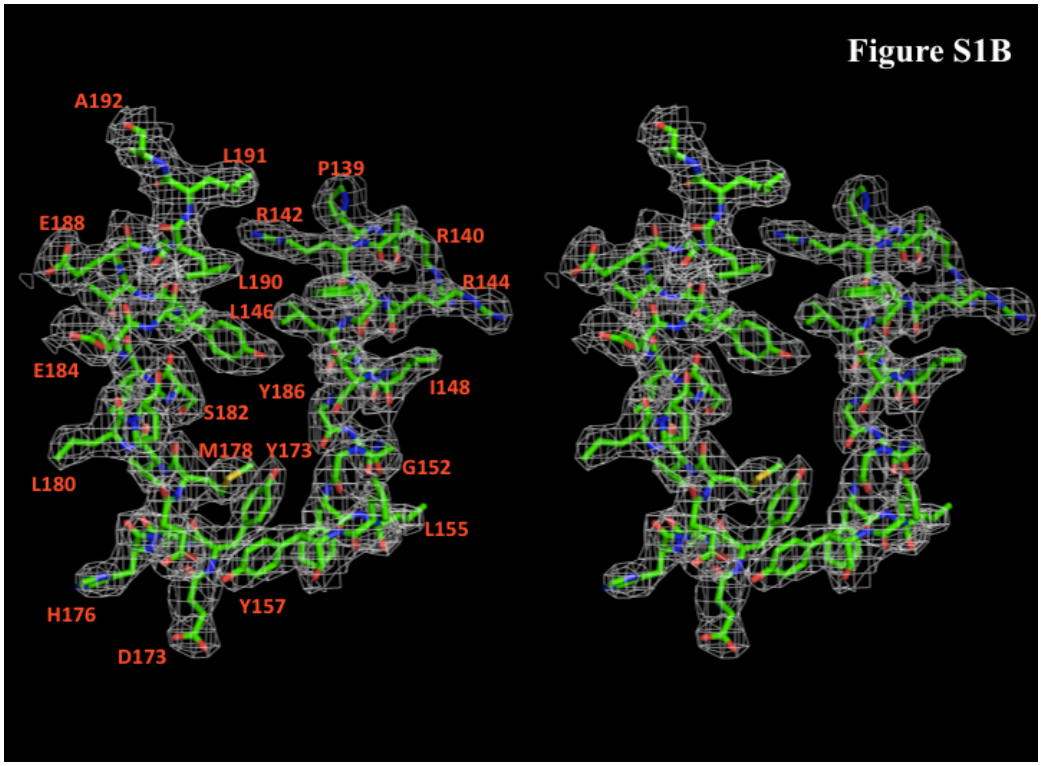

Fig. S1. Stereo view of the electron density maps of Rv1219c at a resolution of 2.99 Å. (A) The electron density maps are contoured at 1.2 σ. The Cα traces of the Rv1219c protomer in the asymmetric unit are in green. Anomalous signals of the six $W_6(\mu\text{-}O)_6(\mu\text{-}Cl)_6Cl_6^{2-}$ cluster sites (contoured at 4 σ) found in the asymmetric unit are colored red. (B) Representative section of electron density in the vicinity of helices α8 and α9. The solvent-flattened electron density (50-2.99 Å) is contoured at 1.2 σ and superimposed with the final refined model (green, carbon; red, oxygen; blue nitrogen; yellow, sulfur).

**Figure S2B**

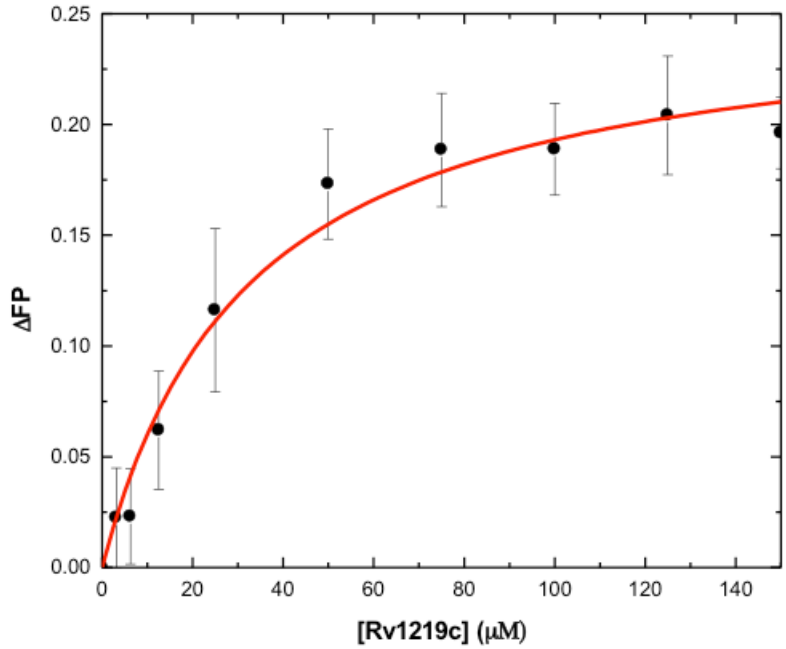


Fig. S2. Representative fluorescence polarization of Rv1219c. (A) The binding isotherm of Rv1219c with rhodamine 6G, showing a $K_D$ of 4.6 ± 0.5 μM. (B) The binding isotherm of Rv1219c with ethidium, showing a $K_D$ of 32.4 ± 7.4 μM. Fluorescence polarization is defined

by the equation, FP = (V – H) / (V + H), where FP equals polarization, V equals the vertical component of the emitted light, and H equals the horizontal component of the emitted light of a fluorophore when excited by vertical plane polarized light. FP is a dimensionless entity and is not dependent on the intensity of the emitted light or on the concentration of the fluorophore. mP is related to FP, where 1 mP equals one thousandth of a FP. The error bars for the binding of ethidium is significantly larger than those for rhodamine 6G binding because the fluorescence signal of ethidium is approximately 100 times weaker than that of rhodamine 6G.

Table S1. Data collection, phasing and structural refinement statistics of Rv1219c.

| **Data set** | Rv1219c | $W_6(\mu\text{-}O)_6(\mu\text{-}Cl)_6Cl_6^{2-}$ derivative | SeMet-Rv1219c |
|---|---|---|---|
| **Data collection** | | | |
| Wavelength (Å) | 0.979 | 0.979 | 0.979 |
| Space group | *I*432 | *I*432 | *I*432 |
| Cell constants (Å) | | | |
| a | 152.07 | 149.77 | 149.03 |
| b | 152.07 | 149.77 | 149.03 |
| c | 152.07 | 149.77 | 149.03 |
| α, β, γ (°) | 90,90,90 | 90,90,90 | 90,90,90 |
| Resolution (Å) | 2.99 (50.00-2.99) | 4.36 (50.00-4.36) | 4.99 (50.00-4.99) |
| Completeness (%) | 94.9 (92.0) | 94.2 (90.5) | 92.7 (91.3) |
| Total reflections | 61,944 | 78,413 | 113,629 |
| Unique reflections | 12,513 | 2,080 | 1,493 |
| Redundancy | 2.0 (2.0) | 3.6 (3.4) | 5.0 (4.9) |
| $R_{merge}$(%) | 6.4 (42.0) | 9.0 (33.9) | 8.9 (37.3) |
| I / σ(I) | 10.2 (2.0) | 29.0 (3.9) | 13.8 (3.8) |

Table S1. continued

| **Phasing** | |
|---|---|
| Number of sites | 6 |
| Phasing power (acentric/centric) | 1.52/1.11 |
| $R_{Cullis}$ (acentric/centric) | 0.71/0.76 |
| Figure of merit (acentric/centric) | 0.57/0.36 |
| **Refinement** | |
| Resolution (Å) | 50 – 2.99 |
| $R_{work}$(%) | 22.09 |
| $R_{free}$(%) | 28.20 |
| Average B-factors ($Å^2$) | 58.84 |
| No. of atoms in protein chain | 1577 |
| No. of water | 0 |
| rms deviations | |
| Bond angles($^o$) | 1.223 |
| Bond angles($^o$) | 0.009 |
| **Ramachandran analysis** | |
| most favored (%) | 94.4 |
| allowed (%) | 5.6 |
| generously allowed (%) | 0.0 |
| disallowed (%) | 0.0 |

Table S2. Top 11 ligands for the Rv1219c regulator.

| Ligand | Structure of ligand | Binding affinity (kcal/mol) |
|---|---|---|
| UCL 1684 ditrifluoroacetate hydrate | 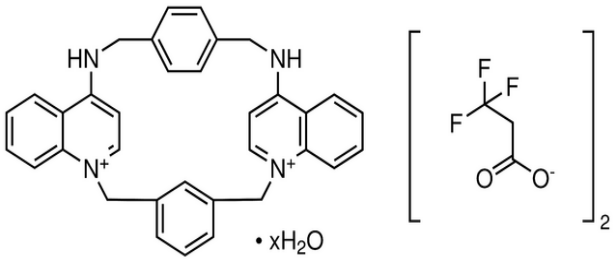 | -13.3 |
| (*S*)-(+)-*N*-(3,5-Dioxa-4-phosphacyclohepta[2,1-*a*;3,4-*a′*]dinaphthalen-4-yl)-dibenzo[*b*,*f*]azepine | 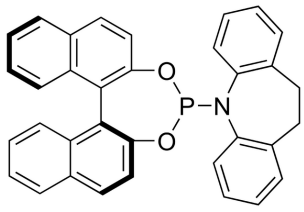 | -12.6 |
| Phthalocyanine | 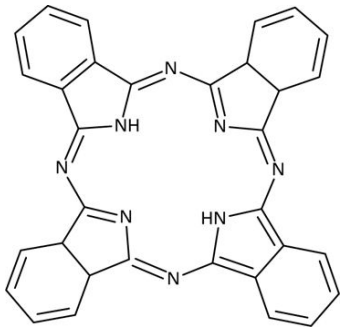 | -12.2 |
| 2-[3-({Methyl[1-(2-Naphthoyl)Piperidin-4-Yl]Amino}Carbonyl)-2-Naphthyl]-1-(1-Naphthyl)-2-Oxoethylphosphonic Acid | 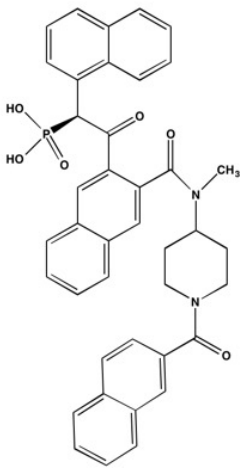 | -12.0 |

Table S2. continued

| | | |
|---|---|---|
| Dihydroergotamine | 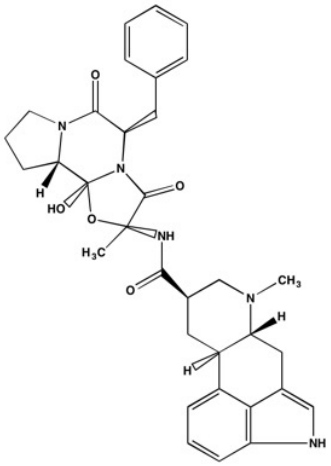 | -11.8 |
| Bis(5*H*-dibenzo[*a*,*d*]cyclohepten-5-yl)phenylphosphine | 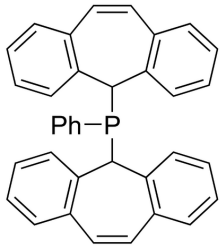 | -11.8 |
| 6((S)-3-Benzylpiperazin-1-Yl)-3-(Naphthalen-2-Yl)-4-(Pyridin-4-Yl)Pyrazine | 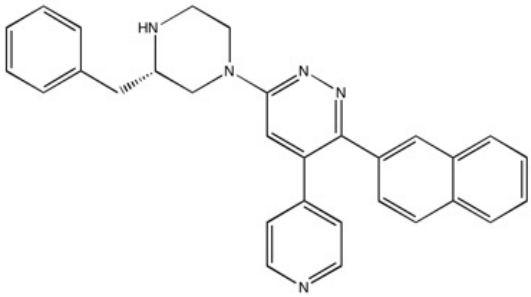 | -11.7 |

Table S2. continued

| | | |
|---|---|---|
| Difenacoum | 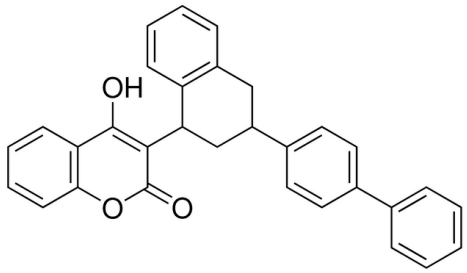 | -11.7 |
| N-(1,3-benzodiazol-2-yl)-3-{[(4S,5S,6S,7R)-3-({3-[(1,3-benzodiazol-2-yl)carbamoyl]phenyl}methyl)-4,7-dibenzyl-5,6-dihydroxy-2-oxo-1,3-diazepan-1-yl]methyl}benzamide | 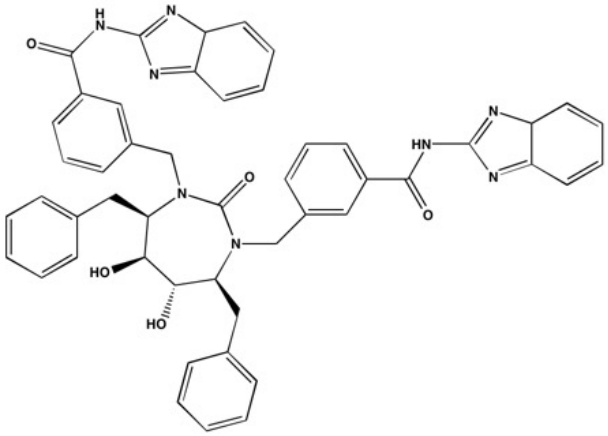 | -11.6 |
| Dibenzo[*a,h*]pyrene | 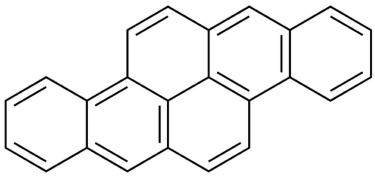 | -11.6 |
| Nitrate Ionophore V | 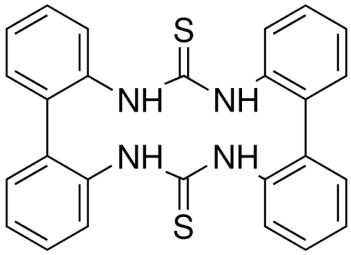 | -11.6 |

Table S3. Primers.

| Probe | Forward primer | Reverse primer |
|---|---|---|
| 1218-1 | TCAGCCGACATGTGCTTCTCC | CACGACATGGTGCTGCCTTCC |
| 1218-2 | GATGACCAATGCCGCGCTCAC | CATGCGTTCAGCCGATCTGAC |
| 1219 | GAATCCGTGCCGACCGAACTG | CTTATCGCCGAGGATGAACG |

# CHAPTER 3. CRYSTAL STRUCTURE OF A HOPANOID TRANSPORTER OF *BURKHOLDERIA*

A manuscript in preparation

Nitin Kumar[1,ψ], Chih-Chia Su[2,ψ], Tsung-Han Chou[2], Abhijith Radhakrishnan[1], Jared A. Delmar[2], Kanagalaghatta R. Rajashankar[3], and Edward W. Yu[1,2*]

[1]Department of Chemistry, Iowa State University, Ames, IA 50011, USA

[2]Department of Physics and Astronomy, Iowa State University, IA 50011, USA

[3]NE-CAT and Department of Chemistry and Chemical Biology, Cornell University, Bldg. 436E, Argonne National Laboratory, 9700 S. Cass Avenue, Argonne. IL 60439.

[ψ]N.K. and C.S. contributed equally to this work.

* To whom correspondence should be addressed. E-mail: ewyu@iastate.edu

## Abstract

Strains of the *Burkholderia cepacia* complex (Bcc) are Gram-negative opportunisitic bacteria that are capable of causing serious diseases, mainly in immunocompromised individuals. Bcc pathogens are intrinsically resistant to multiple antibiotics, including β-lactams, aminoglycosides, fluoroquinolones and polymyxins.[1-4] They are major pathogens in patients with cystic fibrosis (CF) and can cause severe necrotizing pneumonia, which is often fatal.[5] Hopanoid biosynthesis is one of the major mechanisms involved in multiple antimicrobial resistance of Bcc pathogens.[2] The *hpnN* gene of *B. multivorans* encodes an integral membrane protein of the HpnN family of transporters, which is responsible for shuttling hopanoids to the outer membrane.[6] Here, we report crystal structures of *B. multivorans* HpnN, revealing a dimeric molecule with an overall butterfly shape. Each subunit of the transporter contains 12 transmembrane helices and two periplasmic loops that suggest a plausible pathway for substrate transport. Further analyses indicate that HpnN is capable of shuttling hopanoid virulence factors from the outer leaflet of the inner membrane to the periplasm. Taken together, our data suggest that the HpnN transporter is critical for multidrug resistance and cell wall remodeling in *Burkholderia*.


## Introduction

*Burkholderia multivorans* is a successful human pathogen and a member of the *B. cepacia* complex (Bcc) that causes pneumonia in immunocompromised individuals with underlying lung diseases, such as cystic fibrosis (CF) and chronic granulomatous disease (CGD).[7] Bcc consists of a group of at least 17 closely-related Gram-negative bacteria with extreme genetic capacity and metabolic diversity. All Bcc members can trigger chronic airway infections in CF patients and have emerged as opportunistic pulmonary pathogens.[8] *B. cenocepacia* and *B. multivorans* are the two most commonly isolated species,[9,10] which are

threats for outbreaks. Bcc infections in CF patients are associated with enhanced morbidity and mortality. They also have the capacity to cause rapid clinical deterioration with septicemia that leads to death. Several outbreaks of *B. multivorans* causing severe morbidity and mortality in both CF and non-CF patients have occurred.[11-13] In 2013, the rapid emergence of a ceftazidime-resistant strain of *B. multivorans* in a CF patient was identified in the United States.[12] It was found that the resistant strain maintained dominance, resulting in an overall decline in patient health and treatment efficiency. Subsequently, a widespread outbreak of infection caused by *B. multivorans* was reported from the Czech Republic.[13] Surprisingly, this outbreak of *B. multivorans* affected non-CF victims with 24% mortality rate, indicating that *B. multivorans* is a significant and emerging threat beyond CF patients.

Bcc pathogens are intrinsically resistant to a broad range of antimicrobials, including β-lactams, fluoroquinolones, aminoglycosides, polymyxins and cationic peptides, creating a major challenge to the treatment of Bcc pulmonary infections.[2] It has been reported that hopanoids play a predominant role in supporting membrane stability and barrier function in *B. multivorans*, thus participating in multidrug resistance.[2,3] A mutant strain of *B. multivorans* lacking the ability to synthesize hopanoids exhibits hypersensitivity to polymyxin B and colistin.[2] Hopanoids are pentacyclic triterpenoid lipids that are sterol analogues in prokaryotic membranes.[14-16] Like cholesterols in eukaryotic membranes, hopanoids are capable of inserting in bacterial membranes and contributing to their stability and stiffness.[17] Hopanoids help membranes withstand damaging stress conditions, including high temperature, low pH and the presence of antibiotics.[2-4,17] Not all bacteria produce hopanoids, but they play a vital role in those that do make them. It has been shown that hopanoid production plays an important role in the physiology and pathogenesis of *B. cenocepacia*.[4,18]

In spite of the importance of hopanoids in bacteria, the mechanism of intracellular hopanoid trafficking for cell wall remodeling has not been explored. A subfamily of the

resistance-nodulation-cell division (RND) superfamily of transporters,[19] termed hopanoid biosynthesis-associated RND (HpnN) transporters,[20] are responsible for shuttling hopanoids from the cytoplasmic membrane to outer membrane of Gram-negative bacteria. As an initial step to elucidate the mechanism of hopanoid transport, we here present the crystal structure of the *B. multivorans* HpnN transporter that is essential for cell wall biogenesis in this pathogen. A combination of the three-dimensional structure and genetic analysis allows us to identify important residues for the function of this membrane protein.

## Results

### Overall structure of HpnN

*B. multivorans* HpnN consists of 877 amino acids (Fig. 1). Two distinct conformations of HpnN (forms I and II) were captured in two different forms of crystals (Table S1). In each structure, two monomers were found in the asymmetric unit arranged as a dimer (Figs. S1 and S2). Overall, the topology of HpnN is unique. The HpnN dimer is butterfly-shaped with a twofold symmetry axis perpendicular to the membrane plane (Fig. 2a). The overall structure of HpnN indicates that this membrane protein mainly constitutes the transmembrane and periplasmic domains. Viewed in parallel to the membrane, the dimer is about 110 Å tall, 100 Å wide and 52 Å thick.

Each protomer of HpnN in the dimer contains 12 transmembrane helices (TMs 1-12 and TMs 1′-12′, respectively). In addition, the monomer possesses a large periplasmic domain formed by two periplasmic loops between TMs 1 and 2 (loop 1), and between TMs 7 and 8 (loop 2). Loop 1 is composed of 11 α-helices and four β-strands, whereas loop 2 constitutes 10 α-helices and three β-strands. The TMs, α-helices and β-strands are designated numerically from the N- to C-termini: TM1 (a (2-13) and b (17-37)), α1 (45-48), α2 (56-65), α3 (67-70), β1 (73-79), α4 (82-102), β2 (106-109), α5 (115-124), α6 (127-149), α7 (153-170), α8 (175-

194), β3 (215-222), α9 (236-247), α10 (249-253), β4 (255-260), α11 (262-273), TM2 (277-295), TM3 (299-322), TM4 (331-359), TM5 (363-393), TM6 (398-429), TM7 (a (443-452) and b (454-474)), α12 (482-484), α13 (490-500), β5 (509-513), α14 (516-528), β6 (534-536), α15 (538-541), α16 (547-564), α17 (574-594), α18 (598-614), α19 (618-643), α20 (655-661), β7 (668-673), α21 (686-698), TM8 (705-738), TM9 (742-766), TM10 (775-796), TM11 (a (803-810) and b (812-828)) and TM12 (832-858). The N-terminal and C-terminal halves of the transmembrane region are assembled in a pseudo-symmetrical fashion. The TMs are membrane embedded. However, TM8 is significantly longer and protrudes into the periplasm. TM2 and TM8 directly tether the periplasmic subdomains PD1 and PD2, respectively (Fig. 2b). A hairpin is formed in the middle section of each periplasmic loop (loops 1 and 2). These two α-helical hairpins contact one another through a coiled-coil interaction and form a four α-helix bundle, contributing to the hairpin subdomain PD4. PD4 is connected to PD1 and PD2 through an elongated α-helical subdomain PD3, which is composed of three α-helices (Fig. 2b). Several long flexible loops are found to link each periplasmic subdomain, suggesting that the periplasmic domain of HpnN is quite flexible in nature.

The crystal structure reveals that TMs 7, 8 and 9 are involved in the formation of the dimer. Dimerization occurs mainly through hydrophobic interactions, as the interaction surface is mostly hydrophobic in nature. Surprisingly, each protomer of HpnN forms a channel spanning the outer leaflet of the inner membrane and up to the periplasmic domain (Figs. 2b and S3). A cavity is formed within TMs 2, 4 and 11, which also creates the beginning section of the channel. This cavity runs horizontally along the surface of the outer leaflet of the inner membrane and then directly connects to the vertical portion of channel, leading to the periplasm. Potentially, this cavity may form a hopanoid binding site. Interestingly, within the vicinity of this cavity, L826 is conserved (Fig. 1). This residue may play an important role in recognizing hopanoids. The end of this channel is located at the top portion of PD1 and PD2,

where the short helix α5 is also involved in forming this exit. Alignment of protein sequences indicates that several conserved aromatic residues, including F117, F541 and W661 (Fig. 1), are found to line the wall of this exiting site. These conserved residues may play an important functional role for transporting hopanoids in this membrane protein.

Transport of substrates by the RND family of transporters is driven by the proton-motive-force (PMF). Within the transmembrane region, we found that the conserved residues D344, T818 and T819 (Fig. 1) of HpnN are in close proximity and seem to interact with each other to form a triad. These three residues probably create a proton-relay network to translocate protons for energy coupling.

A comparison of the dimeric structures of forms I and II suggests that these two structures depict two different transient states of the transporter. Superimposition of the form I and form II structures of HpnN results in an overall rms deviation of 2.6 Å (Fig. 3). The major difference between these two structures is in the periplasmic domain of the transporter. This conformational change can be interpreted as a rigid-body swinging motion of the periplasmic domain with respect to the transmembrane domain (Fig. 3). Based on the structural information, this rotational motion may govern the opening and closing of the elongated channel formed by HpnN. The two flexible loops connecting TM1 and TM2 to the periplasmic domain appear to form the hinge, which also creates the narrowest region of the elongated channel. The conserved residue L48 is found in the vicinity of the narrowest region. This residue may be important for the gating of this transporter.

**Hopanoid screening using AutoDock Vina**

To elucidate if *B. multivorans* HpnN has the capacity to bind hopanoids, AutoDock Vina[21] was used to calculate the potential binding modes of HpnN with a variety of hopanoids, including diploptene, 17β(H),21β(H)-hopane, 17α(H),21β(H)-hopane, and 17α(H)-22,29,30-

trisnorhopan. Vina suggested that all of these ligands prefer to bind at the cavity formed within TMs 2, 4 and 11 (Fig. S4). Interestingly, the conserved residue L826 is frequently involved in contacting these four hopanoid compounds. The predicted binding free energies are between -7.7 and -8.2 kcal/mol for these hopanoids.

**Mutagenesis studies**

As *B. multivorans* HpnN and *B. thailandensis* HpnN share 82% identity (Fig. S5), we turned to the null mutant strain *B. thailandensis* E264Δ*hpnN*, which lacks the *hpnN* gene, for our mutagenesis studies and to elucidate the important function of the conserved HpnN amino acids. We made a plasmid pHERD20TΩ*hpnN* that contains the *hpnN* gene of *B. thailandensis*. We then transformed these E264Δ*hpnN* cells with pHERD20TΩ*hpnN*, expressing *B. thailandensis* HpnN, or the empty vector pHERD20T. The knockout *B. thailandensis* E264Δ*hpnN* cells, either alone or transformed with the empty vector pHERD20, could not grow in liquid Luria-Bertani broth (LB) in the presence of various antibiotics, including chloramphenicol, novobiocin and polymyxin B (Fig. 4). Surprisingly, *B. thailandensis* E264Δ*hpnN* cells transformed with pHERD20TΩ*hpnN* were capable of growing in liquid LB under these damaging conditions. The experiment suggests that HpnN is critical for mediating multidrug resistance and the expression of *B. thailandensis hpnN* in E264Δ*hpnN* is able to compensate for the loss of the *B. thailandensis hpnN* gene.

To determine whether the conserved residue D344, which forms a salt-bridge triad with T818 and T819, is important for the function of the transporter, we mutated this corresponding residue in *B. thailandensis* HpnN to tyrosine (D344Y) (Table S2). In *B. multivorans* HpnN, residues D344, T818 and T819 most likely establish the proton-relay network and translocate protons for energy coupling (Fig. 4). We therefore also replaced the corresponding residues of T818 and T819 in *B. thailandensis* HpnN by alanines to create the T818A and T819A mutant

transporters (Table S2). We expressed these mutant HpnN transporters in *B. thailandensis* E264Δ*hpnN* cells. We then monitored the growth of these cells harboring the mutant transporter D344Y, T818A or T819A over time in liquid LB supplemented with chloramphenicol, novobiocin or polymyxin B. Similar to the knockout E264Δ*hpnN* cells transformed with the empty vector, growth of cells expressing these mutant transporters was severely attenuated in these liquid media (Figs. 4 and 5). The data indicate that a mutation on residue D344, T818 or T819 abolishes the function of the HpnN transporter.

To understand if the conserved HpnN residues L48 and L826 that line the wall of the channel are crucial for transport function, we mutated these two corresponding leucines in *B. thailandensis* HpnN into phenylalanines to produce the single-point mutant transporters L48F and L826F. We found that mutations on these two residues abrogate cell growth in liquid LB supplemented with chloramphenicol, novobiocin or polymyxin B (Figs. 4 and 5), demonstrating that these two residues are necessary for the function of the transporter.
The three conserved aromatic residues F117, F541 and W661 likely create the exiting site of the channel within the transporter. Therefore, we replaced each corresponding residue in *B. thailandensis* HpnN by arginine or histidine to make single-point mutants F117R, F541R and W661H. Again, *B. thailandensis* E264Δ*hpnN* cells harboring these mutant transporters are retarded in growth in liquid LB supplemented with chloramphenicol, novobiocin or polymyxin B (Figs. 4 and 5), indicating the important role of these amino acids.

## Discussion

In this paper, we reported crystal structures of the *B. multivorans* HpnN transporter, revealing a dimeric assembly of this membrane protein. Each subunit of HpnN creates a channel spanning the outer leaflet of the inner membrane and up to the periplasmic space. Based on additional experimental data, we believe that HpnN is capable of transferring

hopanoid lipids from the inner membrane to the periplasm. We suspect that the opening and closing of this channel is governed by a rigid-body swinging motion of the periplasmic domain of HpnN with respect to its transmembrane domain. Within the *hpnN* operon of *B. multivorans*, there is a smaller gene *vacJ* (virulence-associated chromosome locus J),[6] encoding a periplasmic chaperone protein VacJ. It is likely that hopanoid trafficking in Gram-negative bacteria is a stepwise process and involves more than one protein machine to achieve the task.

We propose that HpnN plays a major role in the intrinsic antimicrobial resistance of *B. multivorans* by shuttling hopanoids from the cytoplasmic membrane to outer membrane via a specific interaction with the periplasmic protein VacJ, which transfers hopanoids from HpnN to the outer membrane. To this point, the exiting area of the HpnN channel may also form a distinctive protein-protein interaction site for binding VacJ, allowing HpnN to directly transfer the bound hopanoid molecule to the VacJ chaperone. The final step may require the dissociation of HpnN and VacJ, which vehicles the bound hopanoid molecule to the outer membrane.

## Materials and Methods

### Cloning, expression and purification of *B. multivorans* HpnN

Briefly, the full-length HpnN membrane protein containing a 6xHis tag at the C-terminus was overproduced in *E. coli* BL21(DE3)*ΔacrB* cells, which harbors a deletion in the chromosomal *acrB* gene, possessing pET15bΩ*hpnN*. Cells were grown in 12 l of LB medium with 100 μg/ml ampicillin at 25°C. When the $OD_{600\ nm}$ reached 0.5, the culture was treated with 0.2 mM isopropyl-β-D-thiogalactopyranoside (IPTG) to induce *hpnN* expression, and cells were harvested within 15 h. The collected bacteria were resuspended in low salt buffer containing 100 mM sodium phosphate (pH 7.2), 10 % glycerol, 1 mM ethylenediaminetetraacetic acid (EDTA) and 1 mM phenylmethanesulfonyl fluoride (PMSF),

and then disrupted with a French pressure cell. The membrane fraction was collected and washed twice with high salt buffer containing 20 mM sodium phosphate (pH 7.2), 2 M KCl, 10 % glycerol, 1 mM EDTA and 1 mM PMSF, and once with 20 mM HEPES-NaOH buffer (pH 7.5) containing 1 mM PMSF as described previously.[22] The membrane protein was then solubilized in 2% (w/v) n-dodecyl-β-D-maltoside (DDM). Insoluble material was removed by ultracentrifugation at 100,000 x g. The extracted protein was purified with a $Ni^{2+}$-affinity column. The purified protein was dialyzed and concentrated to 20 mg/ml in a buffer containing 20 mM Na-HEPES (pH 7.5) and 0.05% DDM. A final purification step was performed using a G200 size exclusion column loaded with buffer solution containing 20 mM Na-HEPES (pH 7.5) and 0.05% DDM. The purity of the HpnN protein (>95%) was judged using 10% SDS-PAGE stained with Coomassie Brilliant Blue. The purified protein was then concentrated to 20 mg/ml in a buffer containing 20 mM Na-HEPES (pH 7.5) and 0.05% DDM.

For 6xHis selenomethionyl-substituted (SeMet)-HpnN protein expression, a 10 ml LB broth overnight culture containing *E. coli* BL21(DE3)*ΔacrB*/pET15bΩ*hpnN* cells was transferred into 120 ml of LB broth containing 100 μg/ml ampicillin and grown at 37°C. When the $OD_{600\ nm}$ value reached 1.2, cells were harvested by centrifugation at 6000 rev/min for 10 min, and then washed two times with 20 ml of M9 minimal salts solution. The cells were re-suspended in 120 ml of M9 media and then transferred into a 12 l pre-warmed M9 solution containing 100 μg/ml ampicillin. The cell culture was incubated at 25°C with shaking. When the $OD_{600\ nm}$ reached 0.4, 100 mg/l of lysine, phenylalanine and threonine, 50 mg/l isoleucine, leucine and valine, and 60 mg/l of L-selenomethionine were added. The culture was induced with 0.2 mM IPTG after 15 min. Cells were then harvested within 15 h after induction. The procedures for purifying SeMet-HpnN were identical to those of the native protein.

**Crystallization of *B. multivorans* HpnN**

Crystals of the HpnN protein were obtained using sitting-drop vapor diffusion. The forms I crystals were grown at room temperature in 24-well plates with the following procedures. A 2 μl protein solution containing 20 mg/ml HpnN in 20 mM Na-HEPES (pH 7.5) and 0.05% (w/v) DDM was mixed with a 2 μl of reservoir solution containing 16% PEG 2000, 0.1 M sodium citrate (pH 3.5) and 0.2 M $Li_2SO_4$. The resultant mixture was equilibrated against 500 μl of the reservoir solution at 25°C. For the form II crystals, a 2 μl protein solution containing 20 mg/ml HpnN in 20 mM Na-HEPES (pH 7.5) and 0.05% (w/v) DDM was mixed with a 2 μl of reservoir solution containing 15% PEG 2000, 0.1 M sodium citrate (pH 4.0) and 0.2 M $(NH_4)_2SO_4$. The resultant mixture was equilibrated against 500 μl of the reservoir solution at 25°C. The crystallization conditions for SeMet-HpnN were the same as those for crystallizing the form II crystals. Crystals of HpnN (both forms I and II) and SeMet-HpnN grew to a full size in the drops within a month. Typically, the dimensions of the crystals were 0.2 mm x 0.2 mm x 0.2 mm. Cryoprotection of these crystals was achieved by raising the glycerol concentration stepwise to 30% with a 5% increment in each step. Crystals of the tungsten cluster derivative were prepared by incubating the form I crystals in solution containing 18% PEG 2000, 0.1 M sodium citrate (pH 3.5), 0.2 M $Li_2SO_4$, 0.05% (w/v) DDM and 0.5 mM $(NH_4)_2W_6(\mu\text{-}O)_6(\mu\text{-}Cl)_6Cl_6$ for 5 hours at 25°C.

**Data collection, structural determination and refinement**

All diffraction data were collected at 100K at beamline 24ID-C located at the Advanced Photon Source, using a Platus 6M detector (Dectris Ltd., Switzerland). Diffraction data were processed using DENZO and scaled using SCALEPACK.[23] The form I crystals of HpnN belong to space group $P2_1$ (Table S1). Based on the molecular weight of HpnN (93.6 kDa), the asymmetric unit is expected to contain two transporter molecules with a solvent content of

69.2%. The heavy-atom derivative ($W_6(\mu\text{-}O)_6(\mu\text{-}Cl)_6Cl_6^{2-}$ cluster) was isomorphous with the native crystal (Table S1). 12 tungsten cluster sites were identified using SHELXC and SHELXD[24] as implemented in the HKL2MAP package.[25] These heavy-atom sites were refined by single isomorphous replacement with anomalous scattering (SIRAS), using the program AutoSol implemented in PHENIX.[26] These phases were then subjected to density modification, non-crystallographic symmetry (NCS) averaging and phase extension to the full resolution (3.39 Å) of the native data using the program RESOLVE.[27] The resulting phases were of excellent quality, which allowed us to trace most of the molecules. After tracing the initial model manually using the program Coot,[28] the model was refined using PHENIX[26] leaving 5% of reflections in Free-R set. Iterations of refinement using PHENIX[26] and CNS[29] and model building in Coot[28] lead to the 3.39 Å-resolution structural model of the HpnN transporter with excellent geometrical characteristics (Table S1).

The form II crystals of HpnN also took the space group $P2_1$ (Table S1). The SeMet data were employed to collect additional phase information. Molecular replacement with single-wavelength anomalous diffraction (MR-SAD) phasing, using the program Phaser,[30] were utilized to obtain phases. A monomer of the form I structure was used as the search model. Two HpnN molecules were found in the asymmetric unit. The full-length HpnN protein consists of 16 methionine residues and all of these 16 selenium sites were identified in each protomer of the protein (32 total selenium sites in the asymmetric unit). The phases were then subjected to density modification and phase extension to native 3.77 Å-resolution using the program RESOLVE.[27] The SeMet data not only augmented the experimental phases but also helped in tracing the molecules by anomalous difference Fourier maps in which we could ascertain the proper registry of SeMet residues. The model was constructed using Coot.[28] Iterations of refinement using PHENIX[26] and CNS[29] and model building using Coot[28] lead to the final form II structural model of the HpnN transporter at a resolution of 3.77 Å (Table S1).

**Construction of complementing plasmid for *B. thailandensis***

*B. thailandensis* E264 and its null mutant strain E264Δ*hpnN* [BTH_II2350-111::ISlacZ-PrhaBo-Tp/FRT)],[31] which lacks the *hpnN* gene, were obtained from the *Burkholderia thailandensis* Mutant Library (Department of Genome Sciences, University of Washington, Seattle). The deletion of *hpnN* in the null mutant strain was confirmed by PCR.[31,32] The *hpnN* (*BTH_II2350*) ORF from genomic DNA of *B. thailandensis* E264 was amplified by PCR using the primers 5′-CATACCCATGGGATCTGATAAGAATTCATGCTGACTTCCGTCCTCGTC-3′ and 5′-GATCCCCGGGTACCGAGCTCTTAATGATGATGATGGTGATGTTCATCGATTCCTTGCGATTGGTTTAAACTCAATGGTGATGGTGATGATGGACGGCCTTGTGTGATTTGACC-3′ to produce a product that would encode the *B. thailandensis* HpnN recombinant protein containing a 6xHis tag at the C-terminus. The corresponding PCR product was extracted from agarose gel. The vector pHERD20T[33] was digested with EcoRI (NEB, MA) and gel purified. The purified product was inserted into the linearized pHERD20T vector using the SLiCE[34] method. The resulting recombinant plasmid, pHERD20TΩ*bt_hpnN*, was transformed into DH10b cells and the transformants were selected on LB agar plates containing 100 μg/ml ampicillin. The presence of the correct *hpnN* sequence of *B. thailandensis* in the plasmid construct was verified by DNA sequencing.

**Site-directed mutagenesis**

We performed site-directed mutagenesis on residues L48, F117, D344, F541, W661, T818, T819 and L826 of *B. thailandensis* HpnN to generate single point mutant transporters L48F, F117R, D344Y, F541R, W661H, T818A, T819A and L826F. The primers used for these mutations are listed in Table S2. All oligonucleotides were purchased from Integrated DNA Technologies, Inc. (Coralville, IA) in a salt-free grade.

**Plasmid mobilization**

The plasmid pHERD20TΩ*bt_hpnN* was introduced into E264Δ*hpnN* by triparental mating, utilizing the helper plasmid pRK2013. Overnight cultures of the donor (DH10b/pHERD20TΩ*bt_hpnN*), helper (DH5α/pRK2013) and recipient (E264Δ*hpnN*) cells were grown in LB supplemented with 100 μg/ml ampicillin, 50 μg/ml kanamycin and 15 μg/ml polymyxin B, respectively. The cultures were individually diluted 100 fold using LB supplemented with 100 μg/ml ampicillin, 50 μg/ml kanamycin and 15 μg/ml polymyxin B, respectively. Cells were then individually grown at 37°C until $OD_{600\ nm}$ reached 0.5. An aliquot of 400 μl of each culture was taking from each culture. These three aliquots were mixed together and incubated for 1 h at 37°C without shaking. 100 μl of the mixture was placed onto an LB agar plate supplemented with 10 mM $MgSO_4$ and incubated for 16 h at 37°C. Bacterial colonies were then scraped from the agar plate and suspended in 1 ml LB medium. Five 10-fold serial dilutions were performed. 100 μl of the resulting cell suspension was plated on LB agar containing 15 μg/ml polymyxin B and 100 μg/ml carbenicillin. The plate was then incubated for 2-3 days at 37°C to obtain colonies of E264Δ*hpnN*/pHERD20TΩ*bt_hpnN* cells. The triparental mating procedures for cells carrying the mutant transporters were identical to those as described above.

**Cell growth in the presence of antibiotics**

The sensitivity to chloramphenicol, novobiocin and polymyxin B of *B. thailandensis* E264Δ*hpnN* harboring pHERD20TΩ*bt_hpnN*, expressing the wild-type or mutant transporters, or carrying the pHERD20T empty vector were tested in liquid LB. Cells were grown overnight in LB medium containing 15 μg/ml polymyxin B and 100 μg/ml carbenicillin at 37°C. Cells were adjusted to an $OD_{600\ nm}$ of 0.005 in LB supplemented with 5 μg/ml chloramphenicol, 1

μg/ml novobiocin or 1 mg/ml polymyxin B. Cells were inoculated in 96-well microtiter plates (Corning, NY) and incubated in a 37$^{o}$C shaker at 200 rpm. Growth was recorded every 20 min using a Bio Tek plate recorder (Winooski, VT).

## Accession Codes

Atomic coordinates and structure factors for the structures of HpnN have been deposited at the RCSB Protein Data Bank with accession codes 5KHN (form I) and 5KHS (form II).

## Acknowledgements

This work was supported by an NIH Grant R01AI114629 (E.W.Y.). We *thank* Dr. Miguel A. Valvano (Queen's University Belfast, UK) and Dr. Silvia Cardona (University of Manitoba, Canada) for *providing us the plasmid* pScrhaB2. We also thank Hongwei D. Yu (Marshall University, USA) for sharing the plasmid pHERD20T. This work is based upon research conducted at the Northeastern Collaborative Access Team beamlines of the Advanced Photon Source, supported by an award GM103403 from the National Institutes of General Medical Sciences. Use of the Advanced Photon Source is supported by the U.S. Department of Energy, Office of Basic Energy Sciences, under Contract No. DE-AC02-06CH11357.

## References


1) Aaron, S. D., Ferris, W., Henry, D. A., Speert, D. P. & Macdonald, N. E. Multiple combination bactericidal antibiotic testing for patients with cystic fibrosis infected with Burkholderia cepacia. *Am J Respir Crit Care Med* **161**, 1206-1212, doi:10.1164/ajrccm.161.4.9907147 (2000).
2) Malott, R. J., Steen-Kinnaird, B. R., Lee, T. D. & Speert, D. P. Identification of hopanoid biosynthesis genes involved in polymyxin resistance in Burkholderia multivorans. *Antimicrob Agents Chemother* **56**, 464-471, doi:10.1128/aac.00602-11 (2012).
3) Malott, R. J. *et al.* Fosmidomycin decreases membrane hopanoids and potentiates the effects of colistin on Burkholderia multivorans clinical isolates. *Antimicrob Agents Chemother* **58**, 5211-5219, doi:10.1128/aac.02705-14 (2014).
4) Schmerk, C. L., Bernards, M. A. & Valvano, M. A. Hopanoid production is required for low-pH tolerance, antimicrobial resistance, and motility in Burkholderia cenocepacia. *J Bacteriol* **193**, 6712-6723, doi:10.1128/jb.05979-11 (2011).
5) Sajjan, U. *et al.* Immunolocalisation of Burkholderia cepacia in the lungs of cystic fibrosis patients. *J Med Microbiol* **50**, 535-546, doi:10.1099/0022-1317-50-6-535 (2001).
6) Daligault, H. E. *et al.* Whole-genome assemblies of 56 burkholderia species. *Genome Announc* **2**, doi:10.1128/genomeA.01106-14 (2014).
7) Mahenthiralingam, E., Urban, T. A. & Goldberg, J. B. The multifarious, multireplicon Burkholderia cepacia complex. *Nat Rev Microbiol* **3**, 144-156, doi:10.1038/nrmicro1085 (2005).
8) Ledson, M. J., Gallagher, M. J., Corkill, J. E., Hart, C. A. & Walshaw, M. J. Cross infection between cystic fibrosis patients colonised with Burkholderia cepacia. *Thorax* **53**, 432-436 (1998).

9) Zlosnik, J. E. *et al.* Burkholderia species infections in patients with cystic fibrosis in British Columbia, Canada. 30 years' experience. *Ann Am Thorac Soc* **12**, 70-78, doi:10.1513/AnnalsATS.201408-395OC (2015).

10) Drevinek, P. & Mahenthiralingam, E. Burkholderia cenocepacia in cystic fibrosis: epidemiology and molecular mechanisms of virulence. *Clin Microbiol Infect* **16**, 821-830, doi:10.1111/j.1469-0691.2010.03237.x (2010).

11) Whiteford, M. L. *et al.* Outcome of Burkholderia (Pseudomonas) cepacia colonisation in children with cystic fibrosis following a hospital outbreak. *Thorax* **50**, 1194-1198 (1995).

12) Stokell, J. R., Gharaibeh, R. Z. & Steck, T. R. Rapid emergence of a ceftazidime-resistant Burkholderia multivorans strain in a cystic fibrosis patient. *J Cyst Fibros* **12**, 812-816, doi:10.1016/j.jcf.2013.01.009 (2013).

13) Hanulik, V. *et al.* An outbreak of Burkholderia multivorans beyond cystic fibrosis patients. *J Hosp Infect* **84**, 248-251, doi:10.1016/j.jhin.2013.04.001 (2013).

14) Ourisson, G., Rohmer, M. & Poralla, K. Prokaryotic hopanoids and other polyterpenoid sterol surrogates. *Annu Rev Microbiol* **41**, 301-333, doi:10.1146/annurev.mi.41.100187.001505 (1987).

15) Mahato, S. B. & Sen, S. Advances in triterpenoid research, 1990-1994. *Phytochemistry* **44**, 1185-1236 (1997).

16) Saenz, J. P. *et al.* Hopanoids as functional analogues of cholesterol in bacterial membranes. *Proc Natl Acad Sci U S A* **112**, 11971-11976, doi:10.1073/pnas.1515607112 (2015).

17) Welander, P. V. *et al.* Hopanoids play a role in membrane integrity and pH homeostasis in Rhodopseudomonas palustris TIE-1. *J Bacteriol* **191**, 6145-6156, doi:10.1128/jb.00460-09 (2009).

18) Tseng, S. P. *et al.* The contribution of antibiotic resistance mechanisms in clinical Burkholderia cepacia complex isolates: an emphasis on efflux pump activity. *PLoS One* **9**, e104986, doi:10.1371/journal.pone.0104986 (2014).

19) Tseng, T. T. *et al.* The RND permease superfamily: an ancient, ubiquitous and diverse family that includes human disease and development proteins. *J Mol Microbiol Biotechnol* **1**, 107-125 (1999).

20) Doughty, D. M. *et al.* The RND-family transporter, HpnN, is required for hopanoid localization to the outer membrane of Rhodopseudomonas palustris TIE-1. *Proc Natl Acad Sci U S A* **108**, E1045-1051, doi:10.1073/pnas.1104209108 (2011).

21) Trott, O. & Olson, A. J. AutoDock Vina: improving the speed and accuracy of docking with a new scoring function, efficient optimization, and multithreading. *J Comput Chem* **31**, 455-461, doi:10.1002/jcc.21334 (2010).

22) Long, F. *et al.* Crystal structures of the CusA efflux pump suggest methionine-mediated metal transport. *Nature* **467**, 484-488, doi:10.1038/nature09395 (2010).

23) Otwinowski, Z. & Minor, W. [20] Processing of X-ray diffraction data collected in oscillation mode. *Methods in enzymology* **276**, 307-326 (1997).

24) Schneider, T. R. & Sheldrick, G. M. Substructure solution with SHELXD. *Acta Crystallogr D Biol Crystallogr* **58**, 1772-1779 (2002).

25) Pape, T. & Schneider, T. R. HKL2MAP: a graphical user interface for macromolecular phasing with SHELX programs. *Journal of applied crystallography* **37**, 843-844 (2004).

26) Adams, P. D. *et al.* PHENIX: building new software for automated crystallographic structure determination. *Acta Crystallogr D Biol Crystallogr* **58**, 1948-1954 (2002).

27) Terwilliger, T. C. Maximum-likelihood density modification using pattern recognition of structural motifs. *Acta Crystallogr D Biol Crystallogr* **57**, 1755-1762 (2001).

28) Emsley, P. & Cowtan, K. Coot: model-building tools for molecular graphics. *Acta Crystallogr D Biol Crystallogr* **60**, 2126-2132, doi:10.1107/s0907444904019158 (2004).

29) Brunger, A. T. *et al.* Crystallography & NMR system: A new software suite for macromolecular structure determination. *Acta Crystallogr D Biol Crystallogr* **54**, 905-921 (1998).

30) McCoy, A. J. *et al.* Phaser crystallographic software. *J Appl Crystallogr* **40**, 658-674, doi:10.1107/s0021889807021206 (2007).

31) Gallagher, L. A. *et al.* Sequence-defined transposon mutant library of Burkholderia thailandensis. *MBio* **4**, e00604-00613, doi:10.1128/mBio.00604-13 (2013).

32) Figurski, D. H. & Helinski, D. R. Replication of an origin-containing derivative of plasmid RK2 dependent on a plasmid function provided in trans. *Proc Natl Acad Sci U S A* **76**, 1648-1652 (1979).

33) Qiu, D., Damron, F. H., Mima, T., Schweizer, H. P. & Yu, H. D. PBAD-based shuttle vectors for functional analysis of toxic and highly regulated genes in Pseudomonas and Burkholderia spp. and other bacteria. *Appl Environ Microbiol* **74**, 7422-7426, doi:10.1128/aem.01369-08 (2008).

34) Zhang, Y., Werling, U. & Edelmann, W. SLiCE: a novel bacterial cell extract-based DNA cloning method. *Nucleic Acids Res* **40**, e55, doi:10.1093/nar/gkr1288 (2012).

# Figures and captions

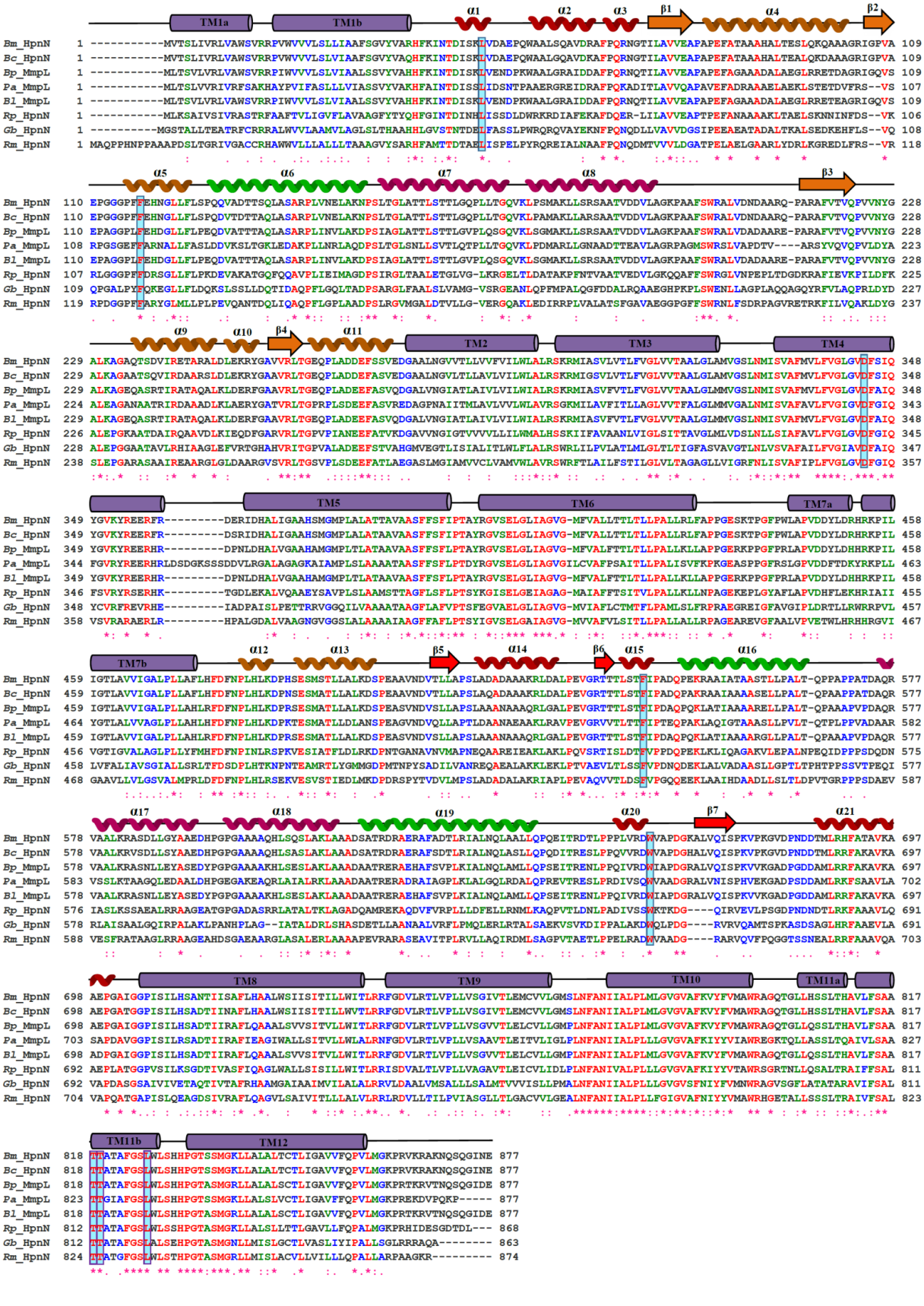

Fig. 1. Sequence and topology of *B. multivorans* HpnN. Alignment of the amino acid sequences was done using CLUSTAL W. *, identical residues; :, >60% homologous residues. Secondary structural elements are indicated: TM, transmembrane segment; α, helix; β, strand. The sequence and topology of *B. multivorans* HpnN are shown at the top (PD1, orange; PD2, red; PD3, green; PD4, magenta). Conserved residues involved in lining the channel or proton relay network of the protein are highlight with cyan bars. (HpnN, hopanoid biosynthesis associated RND; MmpL, mycobacterial membrane protein large; *Bm*, *B. multivorans*; *Bc*, *B. cenocepacia*; *Bp*, *B. pseudomallei*; *Pa*, *P. aeruginosa*; *Bl*, *B. mallei*; *Rp*, *R. palustris*; *Gb*, *G. bethesdensis*; *Rm*, *R. mucosa*).

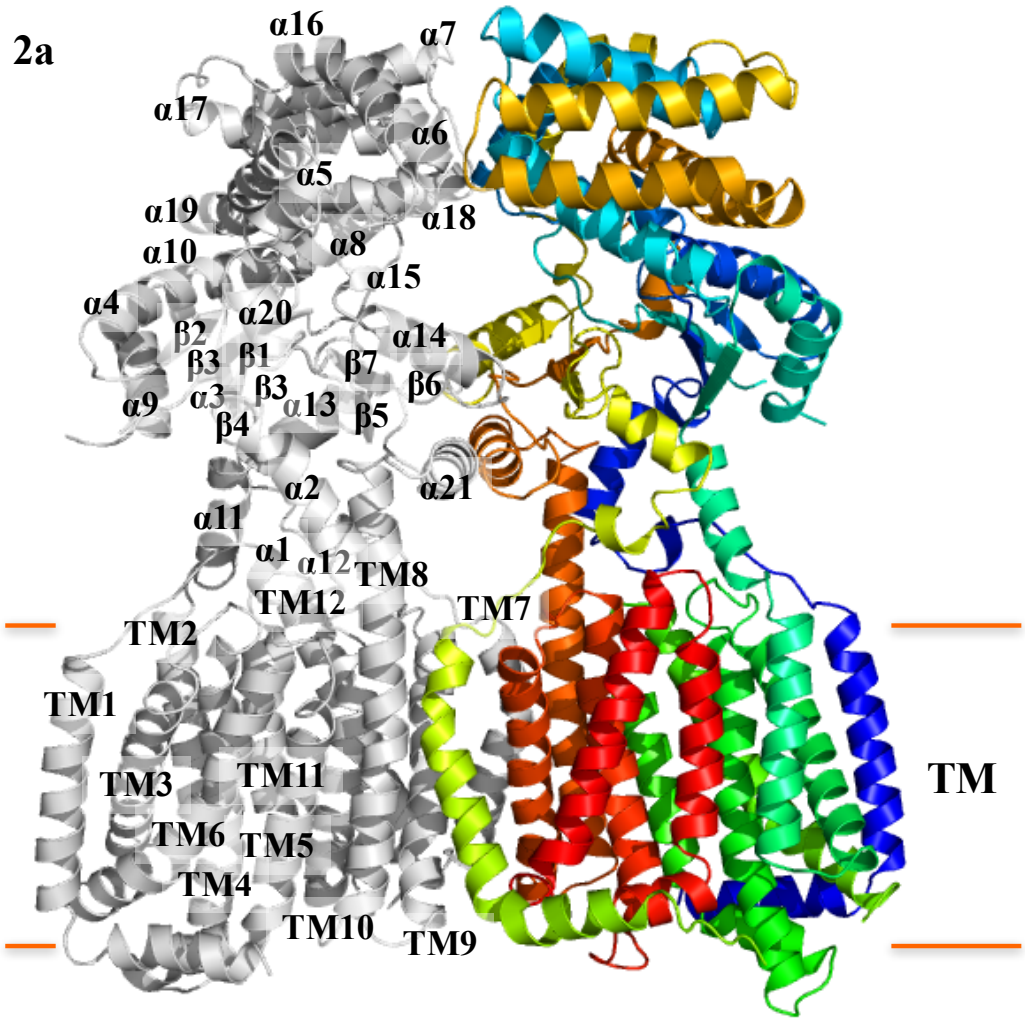

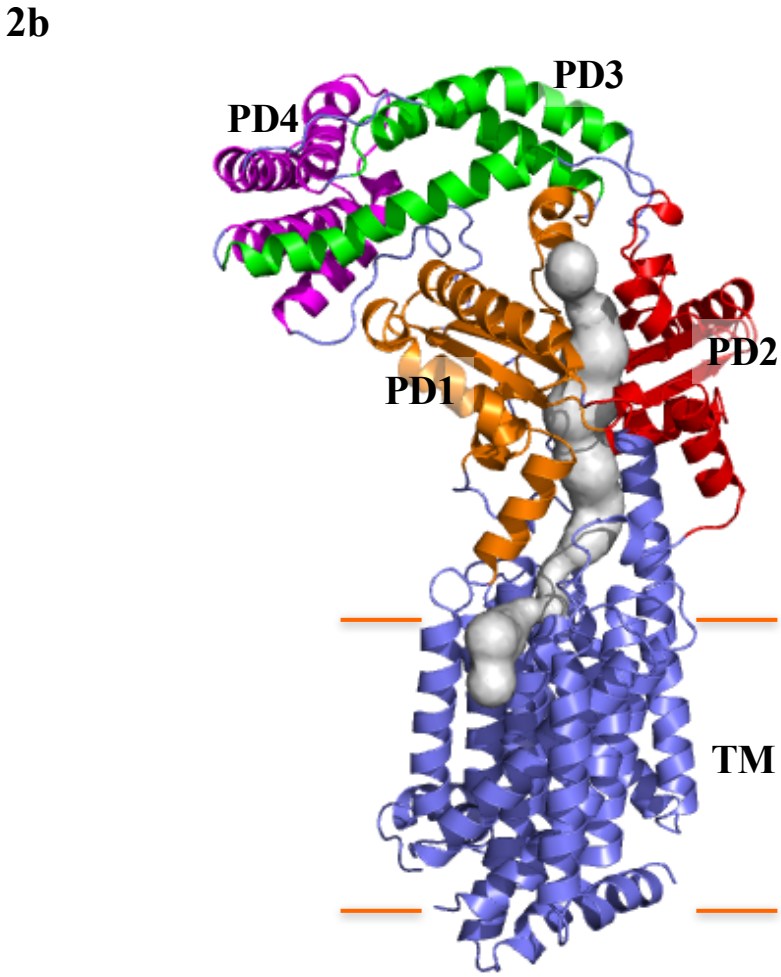


Fig. 2. Structure of the *B. mulitvorans* HpnN transporter. (a) Ribbon diagram of a dimer of HpnN viewed in the membrane plane. The right subunit of the dimer is colored using a rainbow gradient from the N-terminus (blue) to the C-terminus (red), whereas the left subunit is colored gray. Overall, the HpnN dimer forms a butterfly-shaped structure. (b) Each subunit of the HpnN transport forms a channel (colored gray) spanning the outer leaflet of the inner membrane and up to the periplasmic domain. This figure depicts the left subunit of the form I structure of the HpnN dimer. The orientation of this HpnN subunit has been rotated by 60$^{o}$ counterclockwise, based on the vertical C2 symmetry axis of the HpnN dimer, when compared with the orientation of (a). This channel was calculated using the program CAVER (http://loschmidt.chemi.muni.cz/caver). The transmembrane helices are colored slate. PD1, PD2, PD3 and PD4 are colored orange, red, green and magenta, respectively.

3a

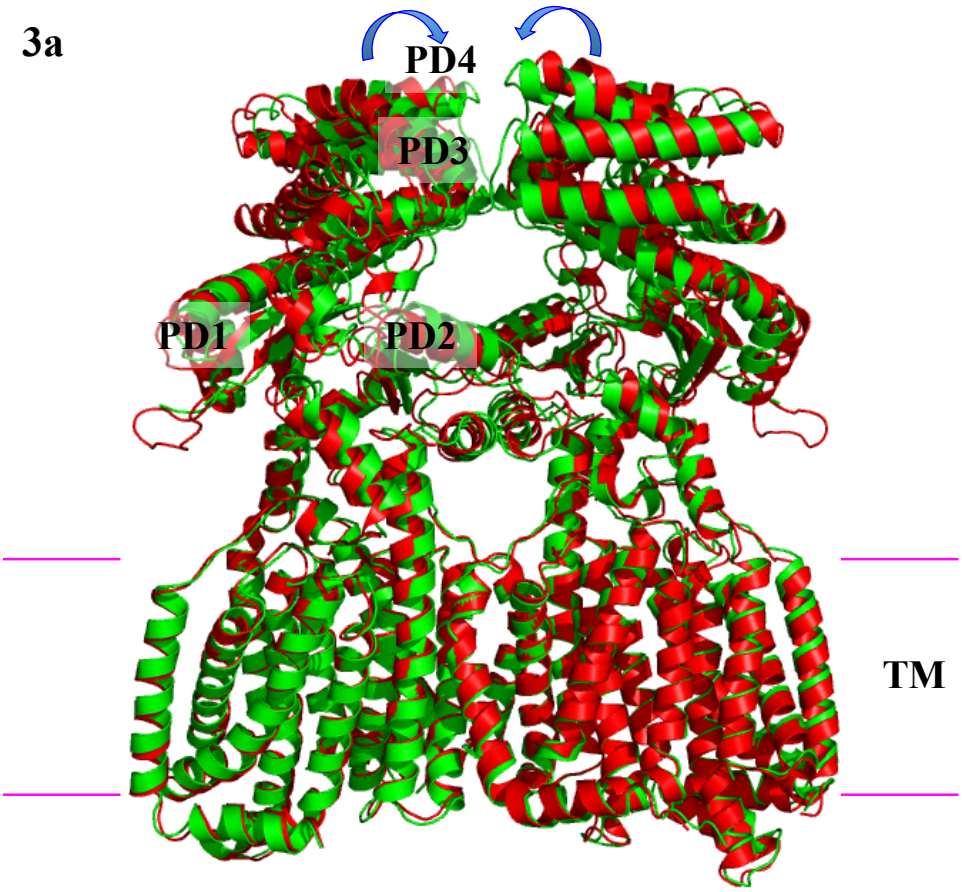


3b

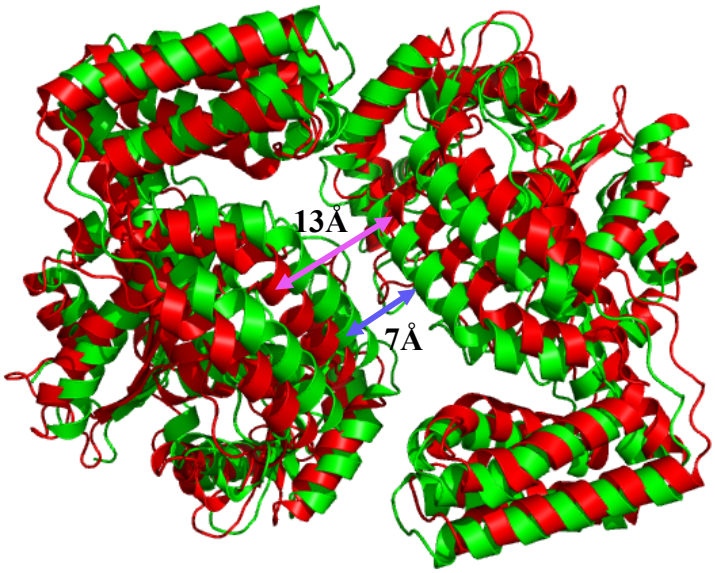

Fig. 3. Structural comparison of forms I and II of the HpnN transporter. (a) Superimposition of the dimeric structures of forms I and II (green, form I; red, form II). For clarity, only the left subunit, PD1-PD4, is labeled. Each arrow indicates a rigid body swinging motion of the periplasmic domain of each monomer, allowing it to come closer to the next subunit within the dimer. (b) Superimposition of the dimeric structures of forms I and II (green, form I; red, form II) viewed from the periplasmic side. This view depicts that the two monomers of the form I structure are at least 6 Å closer to each other at the dimer interface when compared with those of the form II structure.

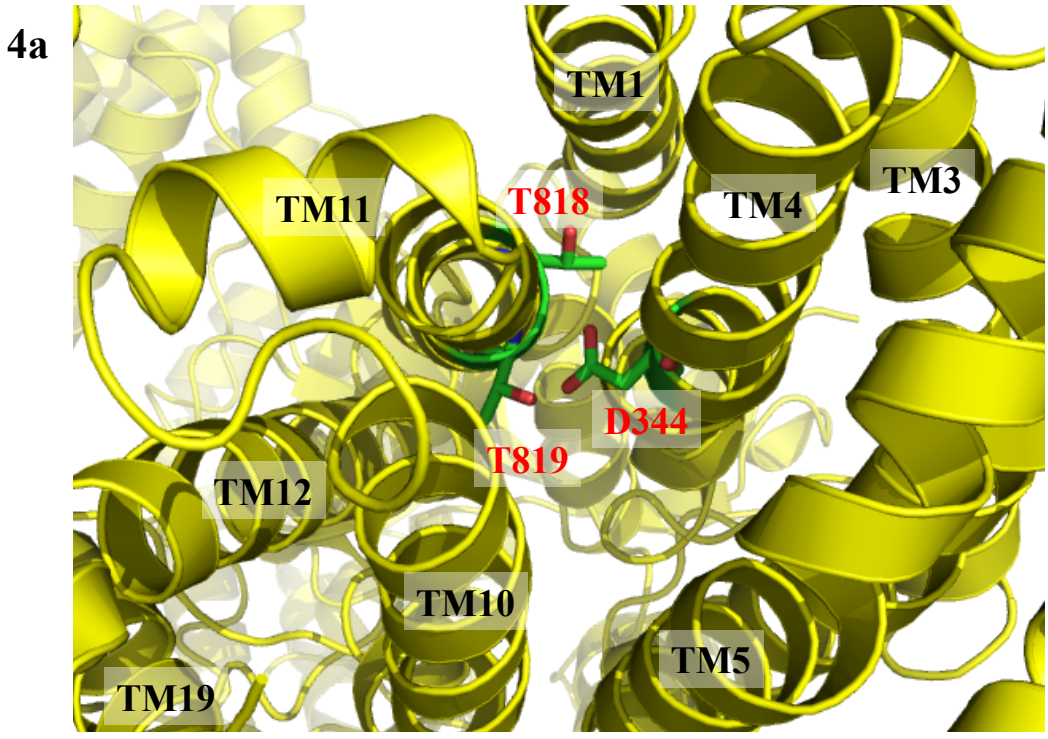

**4b**

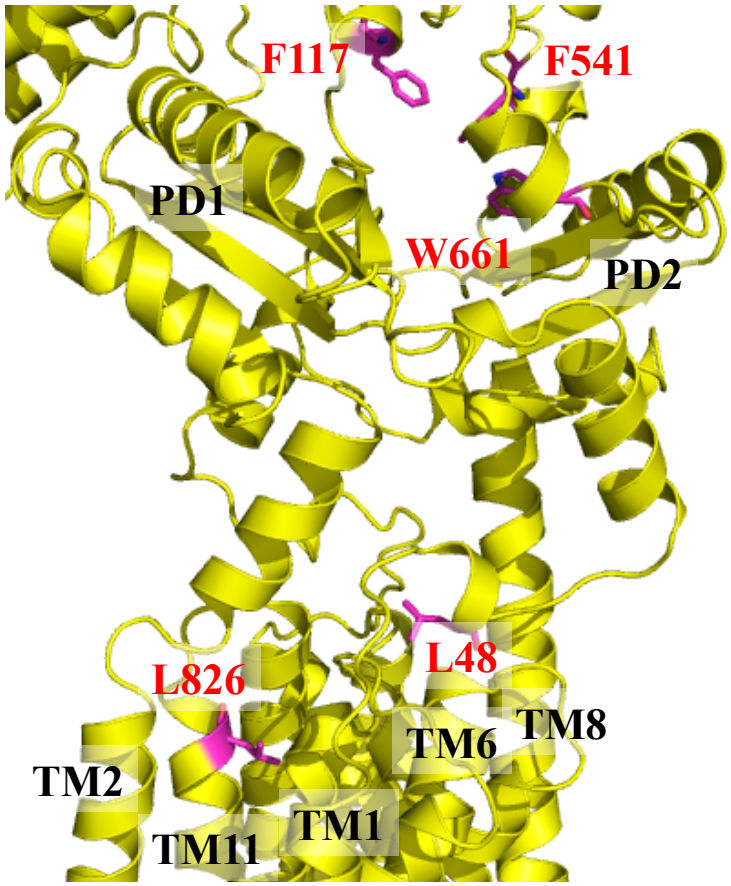
F117
F541
PD1
W661
PD2
L48
L826
TM8
TM6
TM2
TM1
TM11

**4c**

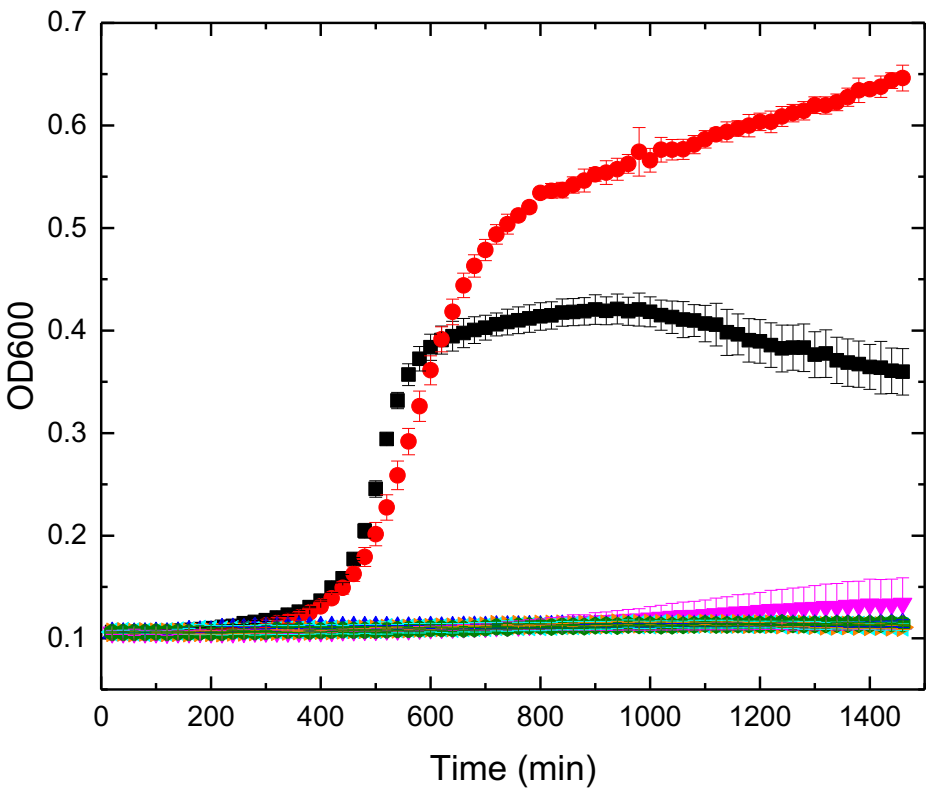
OD600
0.7
0.6
0.5
0.4
0.3
0.2
0.1
0
200
400
600
800
1000
1200
1400
Time (min)

**4d**

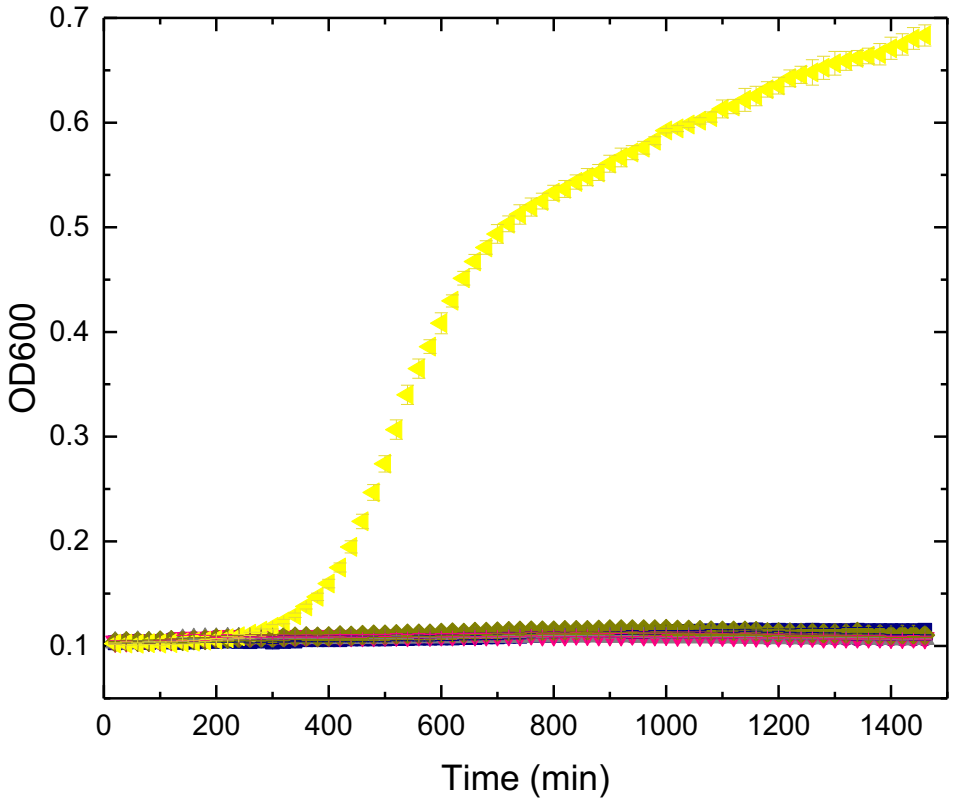


Fig. 4. Important conserved amino acids of HpnN. (a) Ion pairs in the transmembrane domain viewed from the cytoplasmic side. Residues D344 of TM4, and T818 and T819 of TM11 that form ion pairs, which may play an important role in proton translocation, are in green sticks. (b) Side view of a protomer of HpnN that forms a channel. Residues L48, F117, F541, W661 and L826, which line the wall of the channel are in magenta sticks. (c) Time course of the growth of *B. thailandensis* E264Δ*hpnN* cells harboring mutants of the proton relay network. Cells expressing the mutant transporter D344Y, T818A or T819A could not grow in liquid LB in the presence of 5 μg/ml chloramphenicol (black, E264 cells; red, E264Δ*hpnN*/pHERD20TΩ*bt_hpnN* cells expressing HpnN ;magneta, E264Δ*hpnN* cells; blue, E264Δ*hpnN*/pHERD20T cells; cyan, cells expressing D344Y; orange, T818A; green, T819A). Error bars represent standard deviation ($n$ = 3). (d) Time course of the growth of *B.*

*thailandensis* E264Δ*hpnN* cells harboring mutant transporters L48F, F117R, F541R, W661H L826F and G833F. Except mutant G833F, growth of cells expressing the other mutant transporters was severely attenuated in liquid LB supplemented with 5 μg/ml chloramphenicol (purple, L48F; gray, F117R; pink, F541R; dark yellow, W661H; navy blue, L826F; G833F, yellow). Growths of E264 cells, E264Δ*hpnN* cells, E264Δ*hpnN*/pHERD20TΩ*bt_hpnN* cells expressing *B. thailandensis* HpnN and E264Δ*hpnN*/pHERD20T cells carrying the empty vector are shown is (a). Error bars represent standard deviation ($n$ = 3).

**5a**

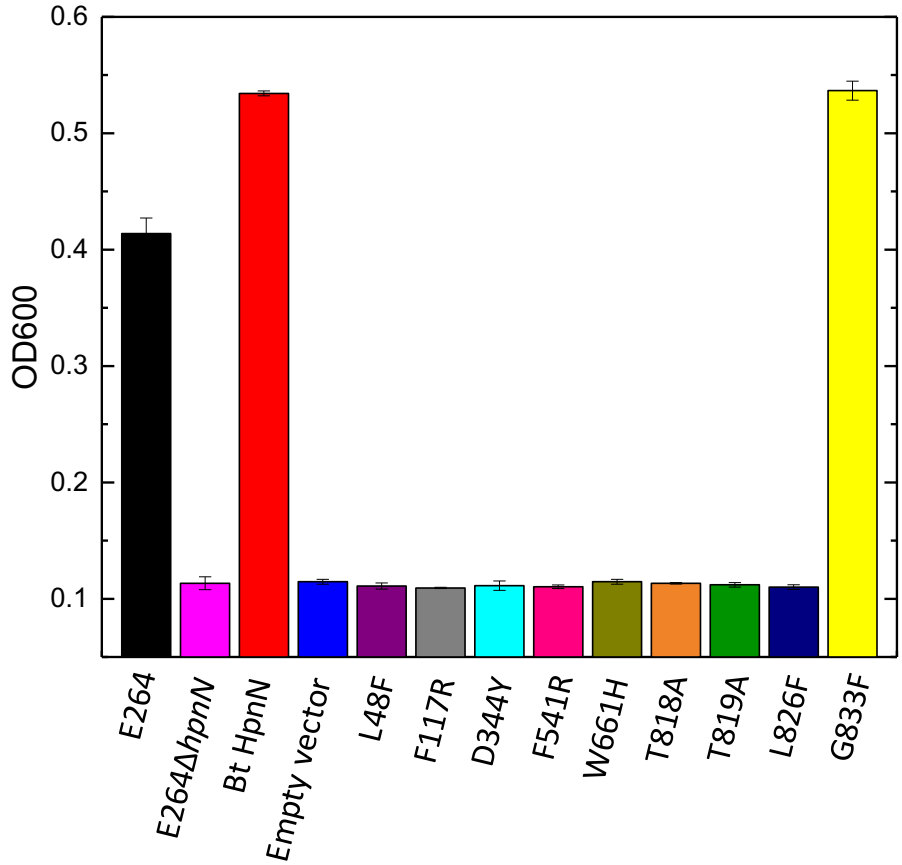

**5b**

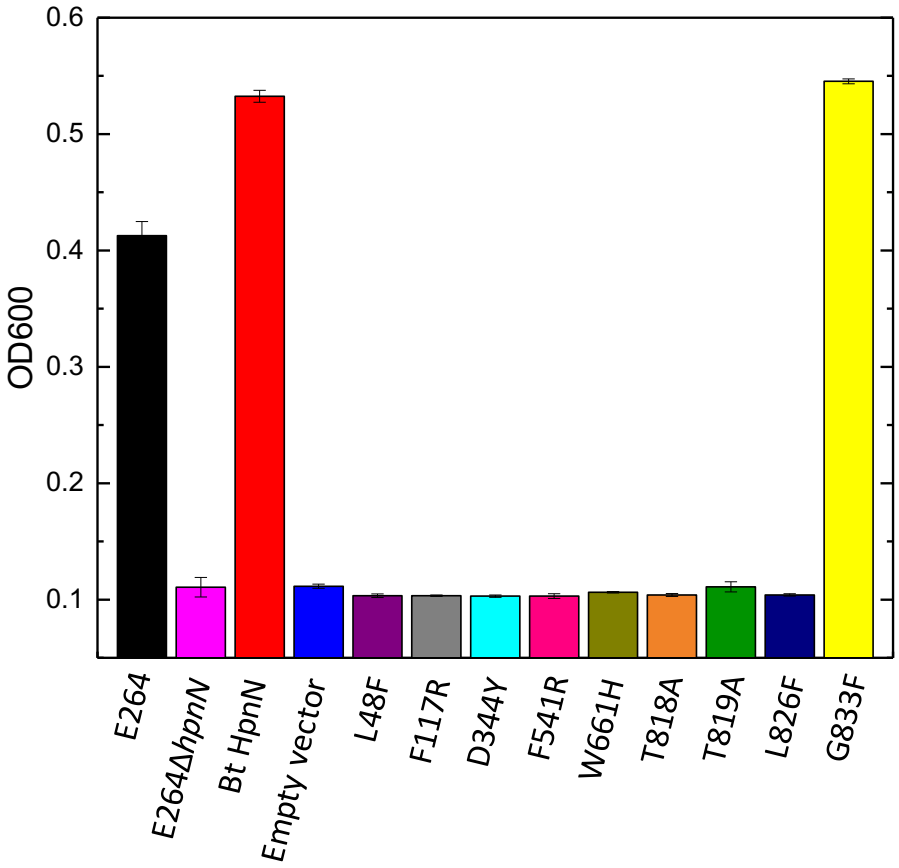
OD600
0.6
0.5
0.4
0.3
0.2
0.1
E264
E264ΔhpnN
Bt HpnN
Empty vector
L48F
F117R
D344Y
F541R
W661H
T818A
T819A
L826F
G833F

**5c**

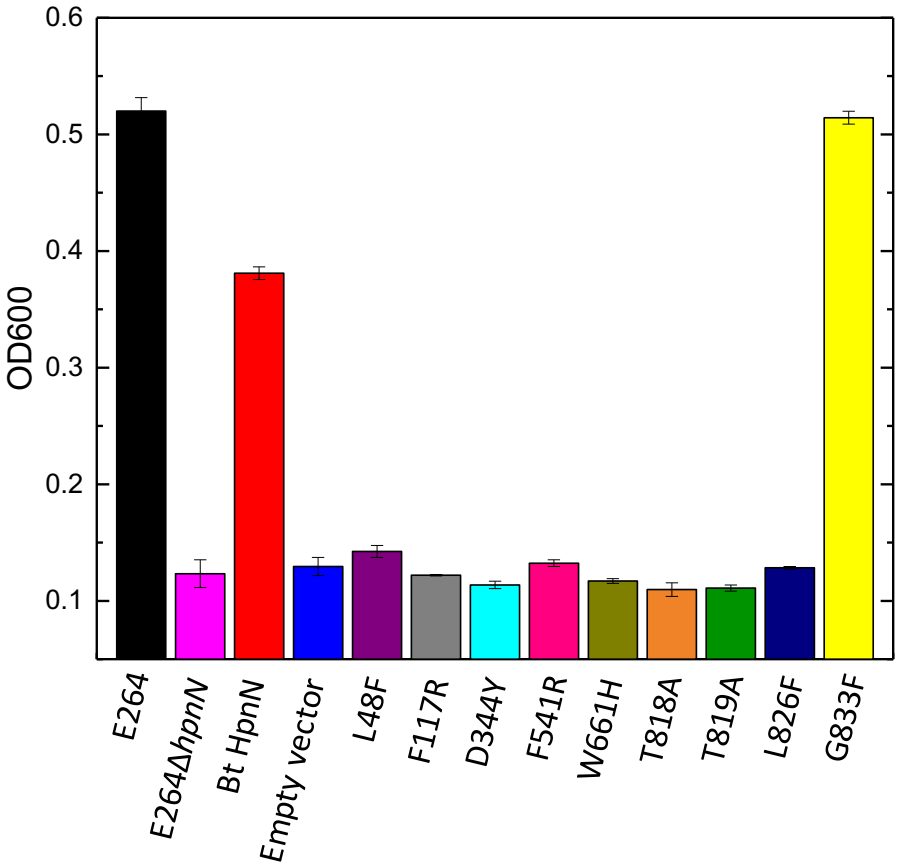
OD600
0.6
0.5
0.4
0.3
0.2
0.1
E264
E264ΔhpnN
Bt HpnN
Empty vector
L48F
F117R
D344Y
F541R
W661H
T818A
T819A
L826F
G833F

Fig. 5. Growth of cells in the presence of antibiotics. *B. thailandensis* E264Δ*hpnN* cells expressing the mutant transporter L48F, F117R, D344Y, F541R, W661H, T818A, T819A or L826F were retarded in growth in liquid LB supplemented with (a) 5 μg/ml chloramphenicol, (b) 1 μg/ml novobiocin or (c) 1 mg/ml polymyxin B compared with cells expressing wild-type *B. thailandensis* HpnN, whereas growth of mutant G833F did not get affected in presence of above three antibiotics. Error bars represent standard deviation ($n$ = 3). "*" indicates values of E264Δ*hpnN*/pHERD20T and E264Δ*hpnN* cells expressing the mutant transporters that are significantly lower than that of E264Δ*hpnN*/pHERD20TΩ*bt_hpnN* expressing wild-type HpnN ($P < 6 \times 10^{-6}$ for (a), $P < 2 \times 10^{-6}$ for (b) and $P < 7 \times 10^{-5}$ for (c); student's $t$-test).

# Supplemental Materials

## Supplemental Figures

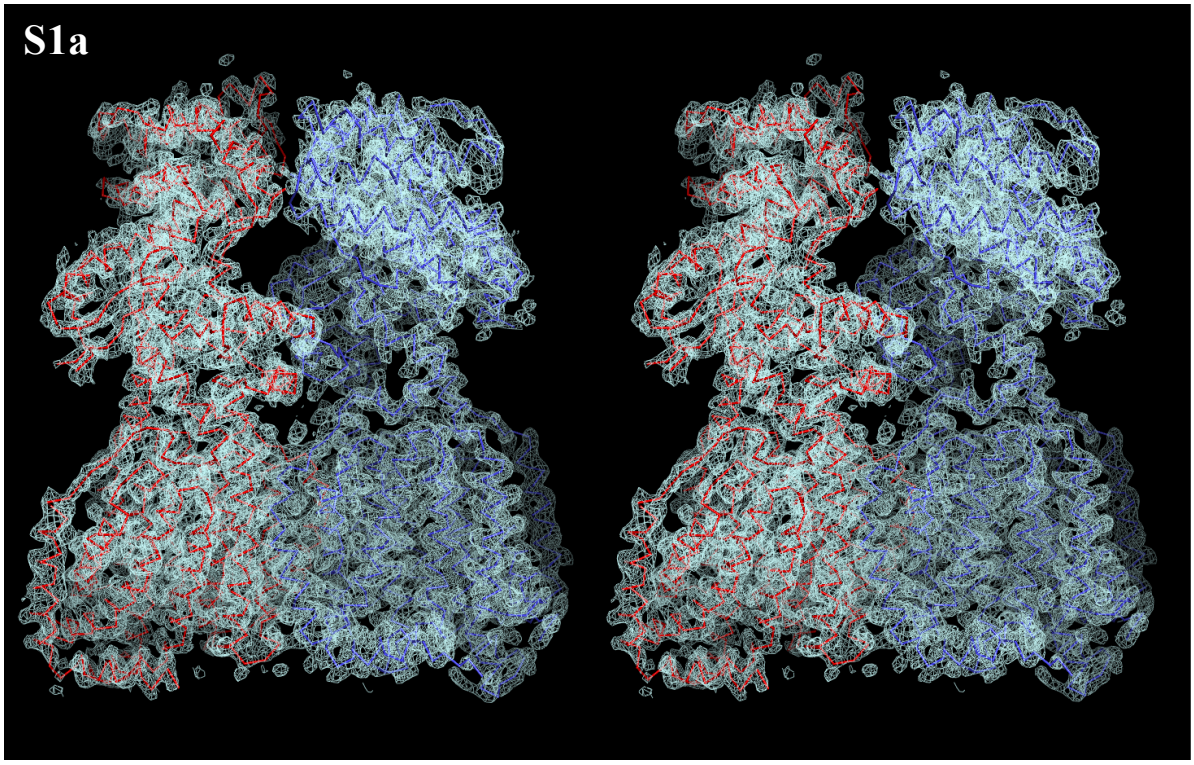


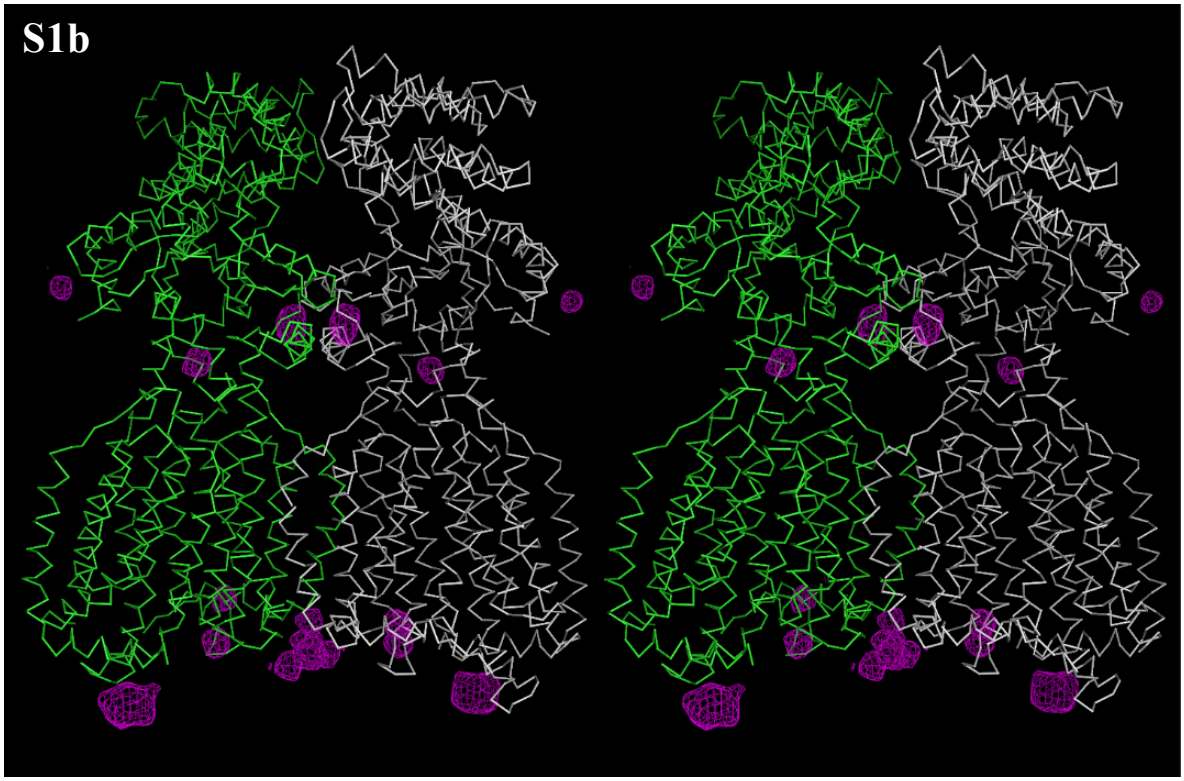

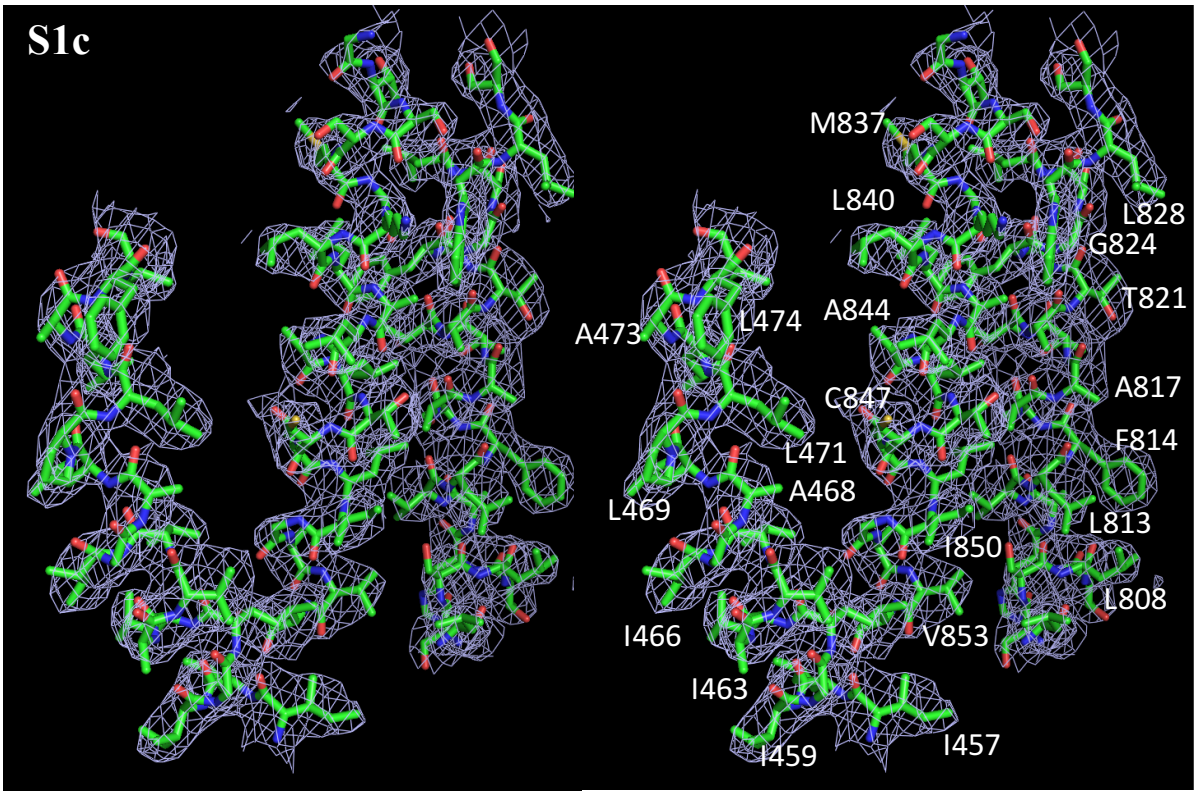


Fig. S1. Stereo view of the electron density maps of HpnN (form I) at a resolution of 3.39 Å. (a) The electron density maps are contoured at 1.2 σ. The Cα traces of the HpnN dimer in the asymmetric unit are included. (b) Anomalous signals of the 12 $W_6(\mu\text{-}O)_6(\mu\text{-}Cl)_6Cl_6^{2-}$ cluster sites (contoured at 3 σ) found in the asymmetric unit are colored magenta. The Cα traces of the two HpnN monomers are colored green and white. (c) Representative section of the electron density in the vicinity of TMs 7, 11 and 12 of HpnN. The electron density (colored light blue) is contoured at the 1.2 σ level and superimposed with the final refined model (green, carbon; red, oxygen; blue, nitrogen).

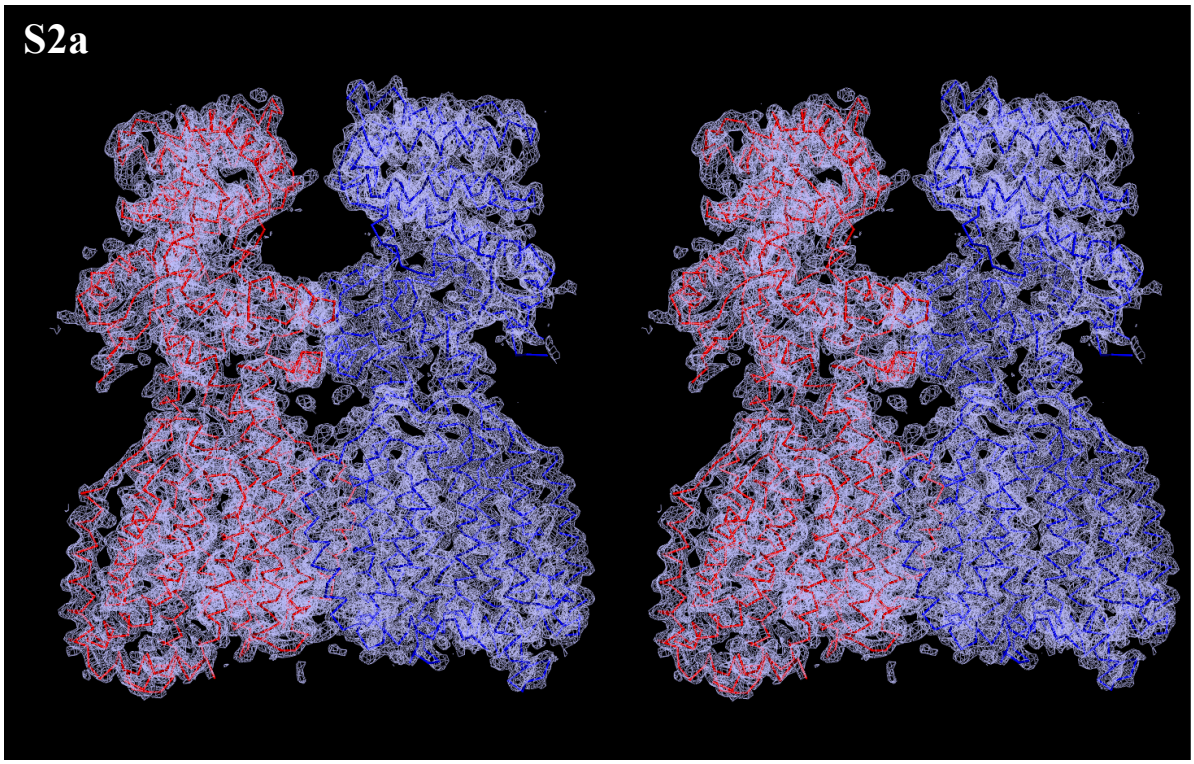
S2a

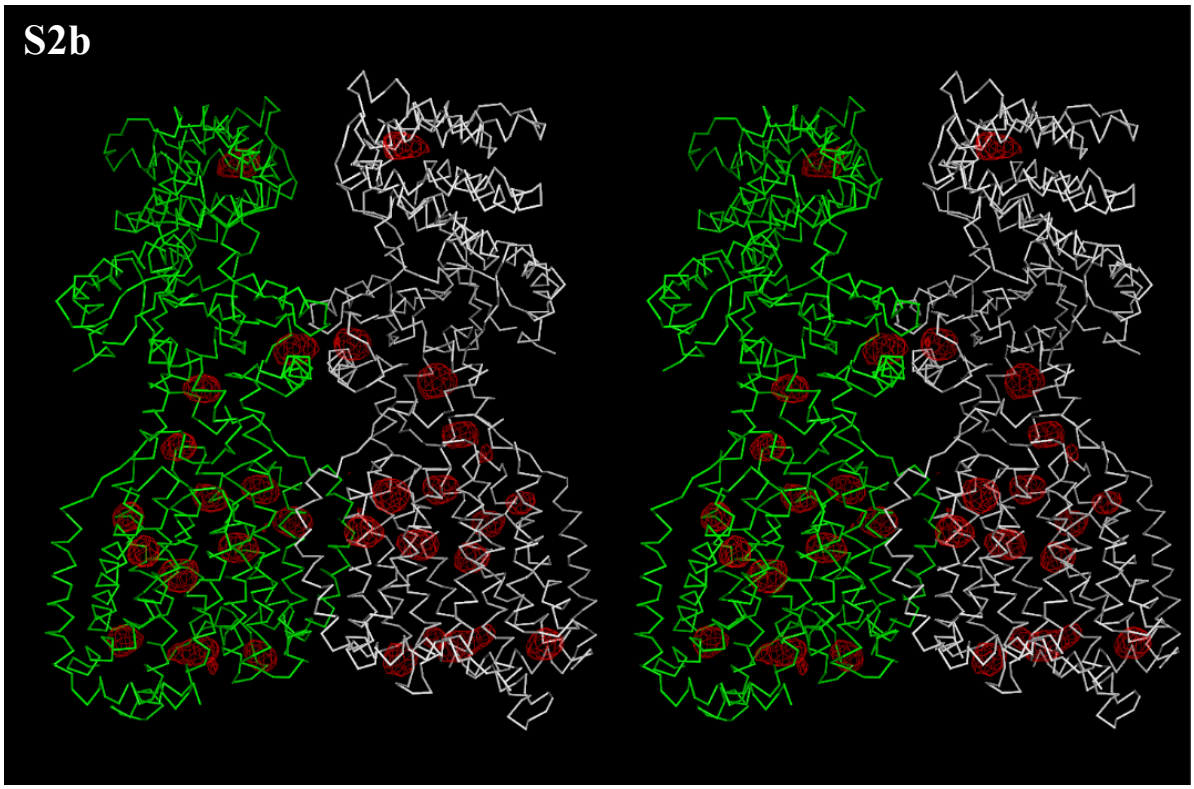
S2b

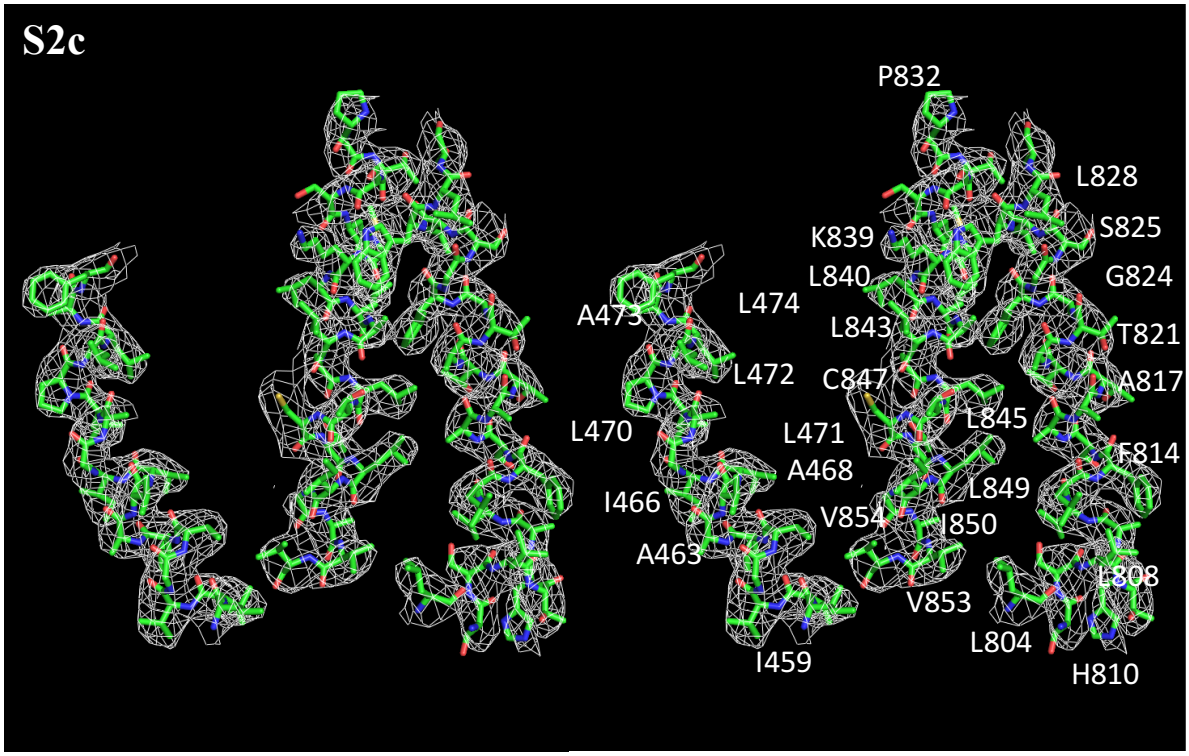
S2c
P832
L828
S825
K839
L840
G824
A473
L474
L843
T821
L472
C847
A817
L470
L471
L845
F814
A468
L849
I466
V854
I850
A463
L808
V853
L804
I459
H810

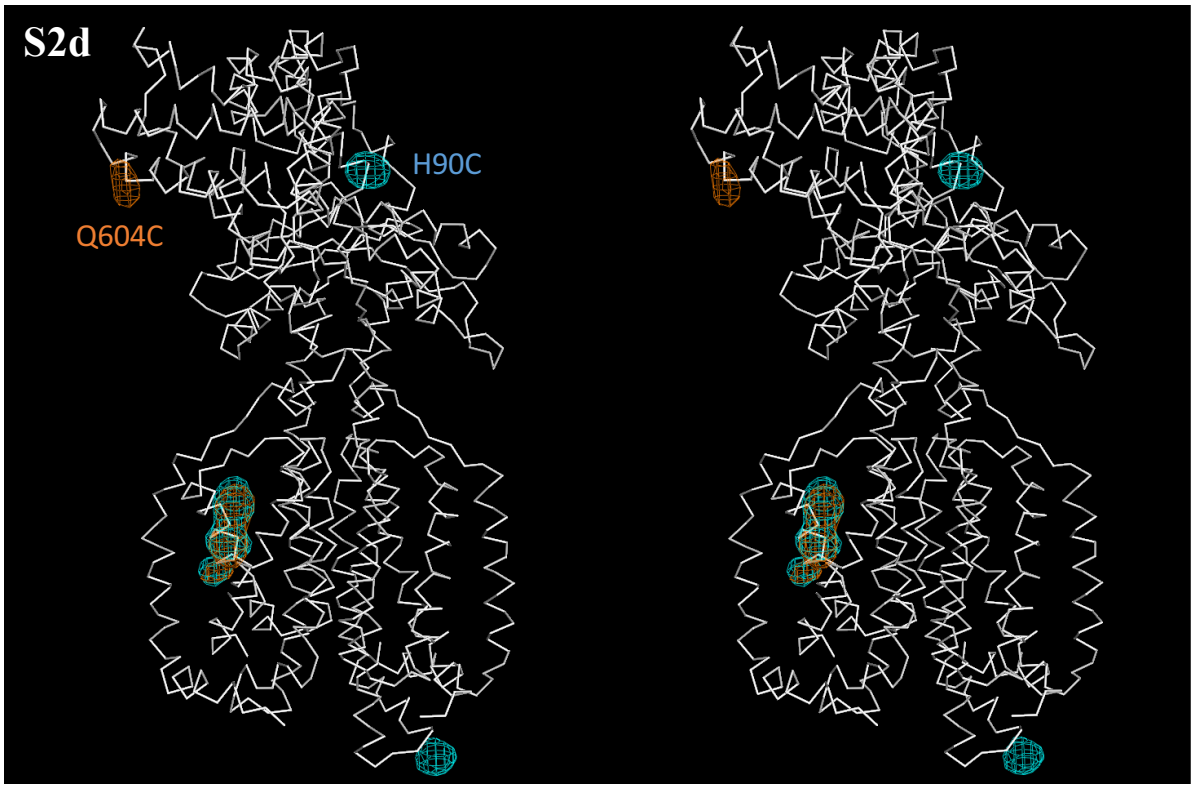
S2d
H90C
Q604C

Fig. S2. Stereo view of the electron density maps of HpnN (form II) at a resolution of 3.77 Å. (a) The electron density maps are contoured at 1.2 σ. The Cα traces of the HpnN dimer in the asymmetric unit are included. (b) Anomalous maps of the 32 selenium sites (contoured at 3 σ). Two protomers forming a dimer of HpnN are found in the asymmetric unit. Each protomer contributes 16 selenium sites corresponding to the 16 methionines (red). The Cα traces of the two HpnN monomers are colored green and white. (c) Representative section of the electron density in the vicinity of TMs 7, 11 and 12 of HpnN. The electron density (colored white) is contoured at the 1.2 σ level and superimposed with the final refined model (green, carbon; red, oxygen; blue, nitrogen). (d) Composite anomalous maps of the Hg sites (contoured at 3 σ) of the H90C and Q604C mutants. These Hg sites confirm the right location of residues H90 (cyan) and Q604 (orange), respectively.

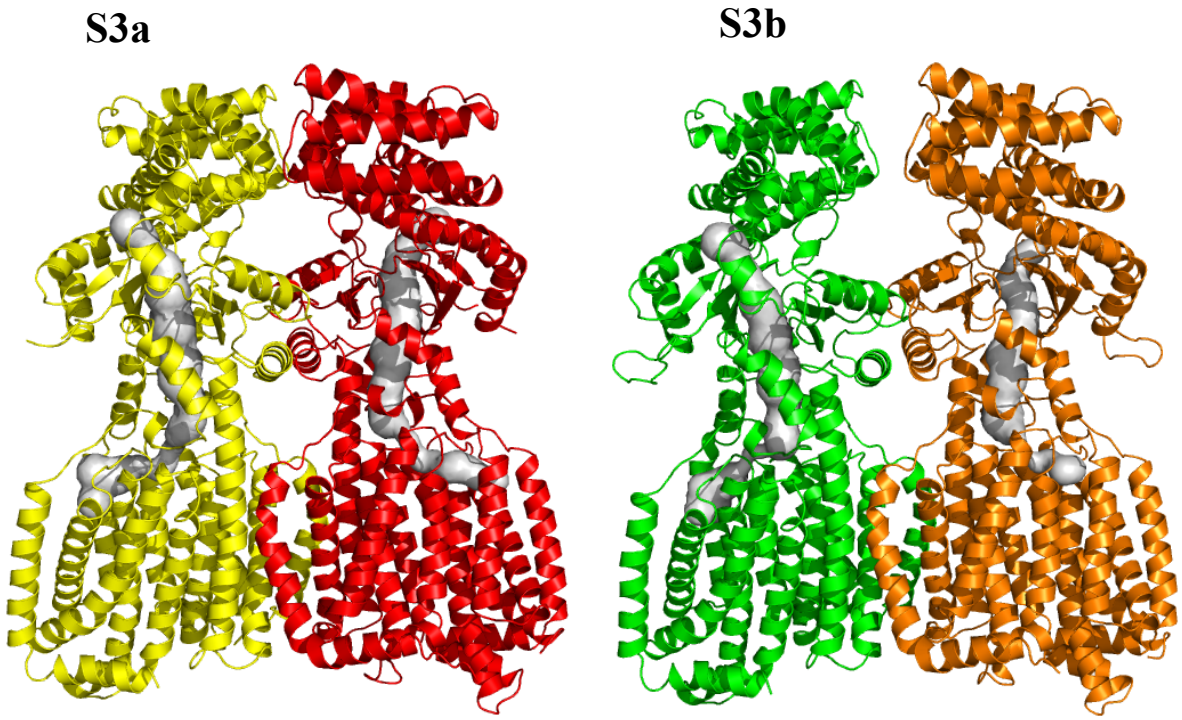

Fig. S3. Channel in the HpnN transporter. (a) Channel formed by each subunit of the form I structure of HpnN. Each channel is colored gray. The left and right subunits of HpnN are colored yellow and red, respectively. (b) Channel formed by each subunit of the form II structure of HpnN. Each channel is colored gray. The left and right subunits of HpnN are colored green and orange, respectively. The calculations were done using the program CAVER (http://loschmidt.chemi.muni.cz/caver).

## S4

```
Bm_HpnN    1 MVTSLIVRLVAWSVRRPVWVVVLSLLIAAFSGVYVARHFKINTDISKLVDAEPQWAALSQAVDRAFPQRNGTILAVVEAPAPEFATAAAHALTESLQKQAAAGRIGPVAEPGGGPFFEHN 120
Bt_HpnN    1 MLTSVLVRLVAWSVRRPIWVVVLSLVAAALSGVYVAHHFKINTDISKLVENDPKWAALGHAIDDAFPQRSQTILAVVEAPAPEFAAAAANALADGLRREAEAGRIGQVSEPGGGPLFEHD 120
           *:**::***********:*******: **:******:************: :*:****.:*:* *****. **************:***:**::.*:::* ***** *:******:***:

Bm_HpnN  121 GLLFLSPQQVADTTSQLASARPLVNELAKNPSLTGLATTLSTTLGQPLLTGQVKLPSMAKLLSRSAATVDDVLAGKPAAFSWRALVDNDAARQPARAFVTVQPVVNYGALKAGAQTSDVI 240
Bt_HpnN  121 GLLFLPEQDVATTTAQLASARPLINVLAKDPSIAGLATTLSTTLGVPLQSGQVKLSGMAKLLSRSAATVDDVLAGKPAAFSWRALVDADAAREPARAFVTVQPVVNYGALQAGEQASRTI 240
           *****. *:** **:********:* ***:**::*********** ** :*****..****************************** ****:******************:** *:* .*

Bm_HpnN  241 RETARALDLEKRYGAVVRLTGEQPLADDEFSSVEDGAALNGVVTLLVVFVILWLALRSKRMIASVLVTLFVGLVVTAALGLAMVGSLNMISVAFMVLFVGLGVDFSIQYGVKYREERFRD 360
Bt_HpnN  241 RATAQALKLDERFGAAVRLTGEQPLADEEFASVQDGALVNGIATLAIVLVILWIALRSKRMIAAVFVTLFVGLVVTAALGLMMVGSLNMISVAFMVLFVGLGVDFAIQYGVKYREERHRD 360
           * **:**.*::*:**.***********:**:**:*** :**:.** :*:****:*********:*:*************** ***********************:***********.**

Bm_HpnN  361 ERIDHALIGAAHSMGMPLALATTAVAASFFSFIPTAYRGVSELGLIAGVGMFVALLTTLTLLPALLRLFAPPGESKTPGFPWLAPVDDYLDRHRKPILIGTLAVVIGALPLLAFLHFDFN 480
Bt_HpnN  361 PNLEHALVGAAHAMGMPLTLATAAVAASFFSFLPTAYRGVSELGLIAGVGMFVALFTTLTLLPALLRLLAPPGERKPPGFPRLAPVDDYLDRHRKPILIGTLAVVIGALPLLAHLRFDFN 480
             .::***:*****:******:***:*********:**********************:************:***** *.**** ******************************.*:****

Bm_HpnN  481 PLHLKDPHSESMSTLLALKDSPEAAVNDVTLLAPSLADADAAAKRLDALPEVGRTTTLSTFIPADQPEKRAAIATAASTLLPALTQPPAPPATDAQRVAALKRASDLLGYAAEDHPGPGA 600
Bt_HpnN  481 PLHLKDPHSESMATLLALKDSPEASVNDVSLLAPSLAAANAAAQRLGALPEVGRTTTLSTFIPDAQPQKLATIAAAARELLPALTQPAAAPVSDAQRVAALKRASNLLEYAAEDYPGPGA 600
           ************:***********:****:******* *:***:**.***************  **:* *:**:**  ********.*.*.:*************:** *****:*****

Bm_HpnN  601 AAAQHLSQSLAKLAAADSATRDRAERAFADTLRIALNQLAALLQPQEITRDTLPPPLVRDWVAPDGKALVQISPKVPKGVDPNDDTMLRHFATAVKAAEPGAIGGPISILHSANTIISAF 720
Bt_HpnN  601 AAAKHLSESLAKLAAADAATRERAEHAFSAPLKIALNQLAMLLQPSEITRKNLPPQIVRDWVAPDGRALVQISPKVPKGADPGDDAMLRRFAKAVKAAEPGTIGGPISILHSADTIIRAF 720
           ***:***:*********:***:***:**: .*:******* ****.****.:*** :*********:************.**.**:***:**.********:***********:*** **

Bm_HpnN  721 LHAALWSIISITILLWITLRRFGDVLRTLVPLLVSGIVTLEMCVVLGMSLNFANIIALPLMLGVGVAFKVYFVMAWRAGQTGLLHSSLTHAVLFSAATTATAFGSLWLSHHPGTSSMGKL 840
Bt_HpnN  721 LQAAALSVVSITVLLWITLRRFGDVLRTLVPLLVSGVVTLELCVLLGMPLNFANIIALPLMLGVGVAFKVYFVMAWRAGQTGLLQSSLTHAVLFSAATTATAFGSLWLSHHPGTASMGRL 840
           *:**  *::***:************************:****:**:***.*************************************:**************************:***:*

Bm_HpnN  841 LALALTCTLIGAVVFQPVLMGKPRVKRAKNQSQGINE 877
Bt_HpnN  841 LALALSCTLIGAVVFQPVLMGKPRTKRVTNQSQGIDE 877
           *****:******************.**..******:*
```

Fig. S4. Protein sequence alignment of *B. multivorans* HpnN and *B. thailandensis* HpnN. Alignment of the amino acid sequences was done using CLUSTAL W. *, identical residues; :, >60% homologous residues. The alignment indicates that these two proteins share 82% identity. Conserved amino acids that are important for the function of these two transporters are highlighted with yellow bars (*Bm*, *B. multivorans*; *Bt*, *B. thailandensis*).

**S5**

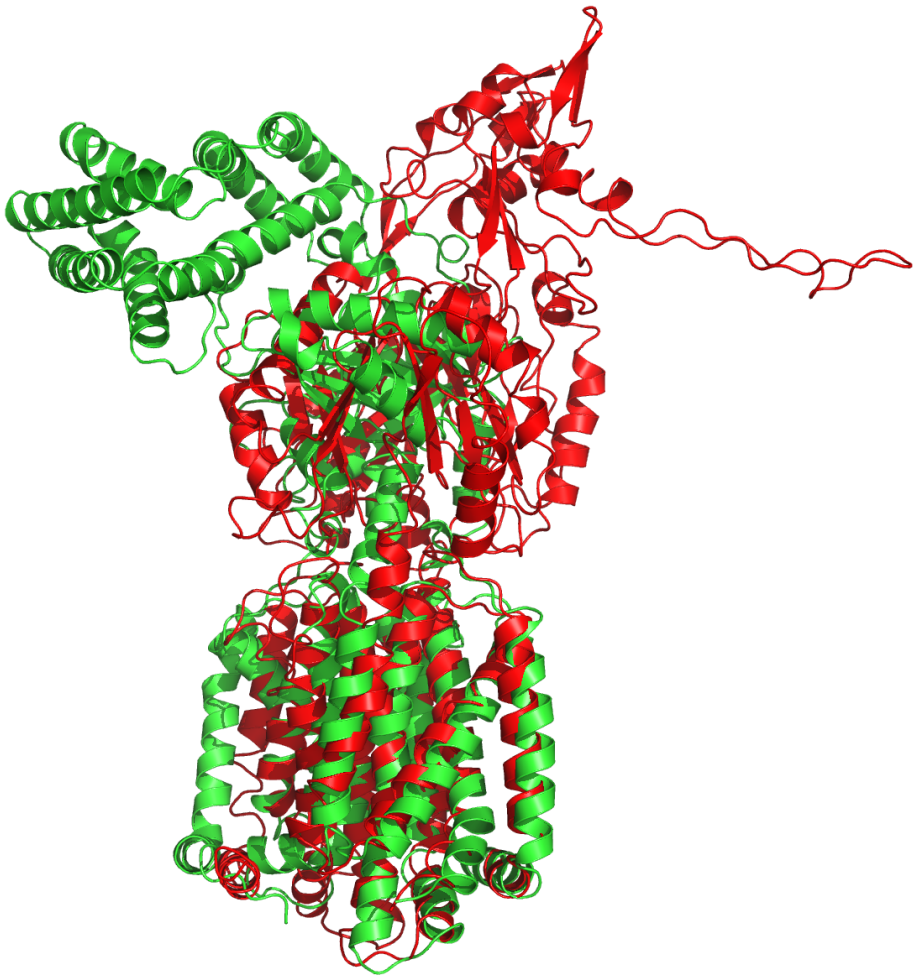

Fig. S5. Comparison of the structures of HpnN and AcrB. Superimposition of a subunit of HpnN (green) onto a subunit of AcrB (red) (pdb code: 2DRD), resulting in a high RMSD of 43.8 Å for 832 $C^{\alpha}$ atoms.

**S6**

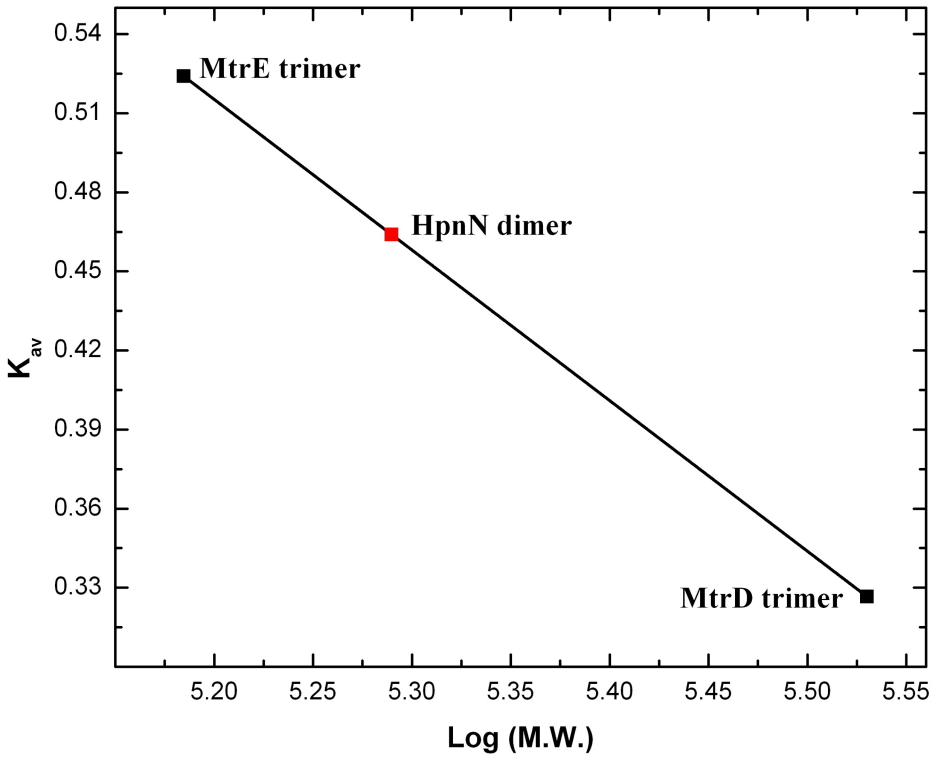


Fig. S6. Representative gel filtration experiment. The experiment demonstrated that HpnN exists as a dimer in solution. The *y* axis values were defined as: $K_{av} = (V_e - V_0)/(V_T - V_0)$, where $V_T$, $V_e$, and $V_0$ are the total column volume, elution volume, and void volume of the column, respectively. Standards used were the trimeric *N. gonorrhoeae* MtrE channel ($M_r$ 145,408) and monomeric *N. gonorrhoeae* MtrD efflux pump ($M_r$ 341,712). The void volume was measured using blue dextran ($M_r$ 2,000,000).

**S7a**

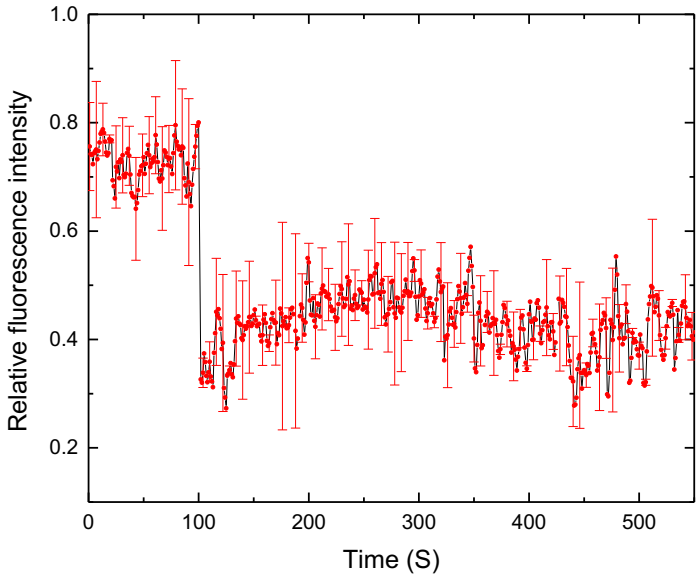
Relative fluorescence intensity
1.0
0.8
0.6
0.4
0.2
0
100
200
300
400
500
Time (S)

**S7b**

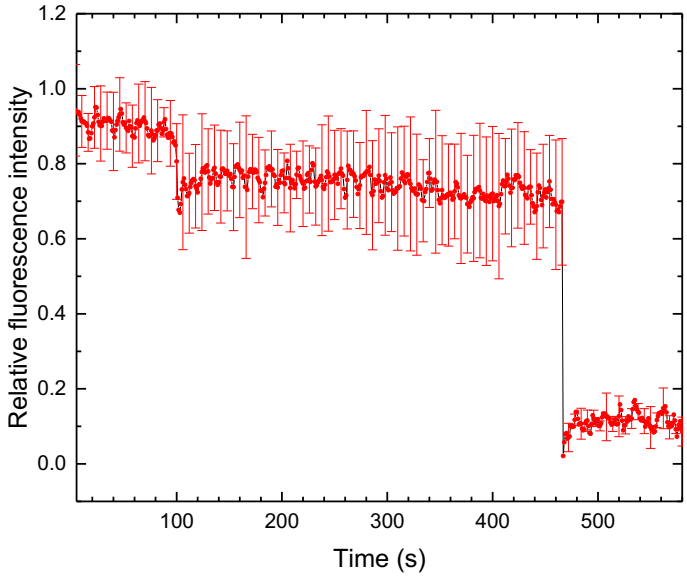
Relative fluorescence intensity
1.2
1.0
0.8
0.6
0.4
0.2
0.0
100
200
300
400
500
Time (s)

**S7c**

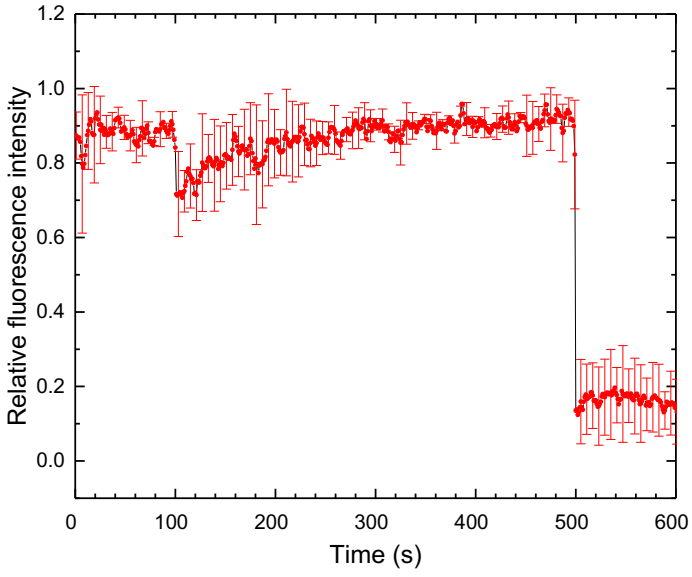
Relative fluorescence intensity
1.2
1.0
0.8
0.6
0.4
0.2
0.0
0
100
200
300
400
500
600
Time (s)

Fig. S7. PMF-dependence of the HpnN transporter. Intravesicular pH changes of the (a) wild-type HpnN proteoliposomes, (b) D344Y HpnN proteoliposomes and (c) empty vesicles were monitored by the BCECF fluorescence. Before the addition of HCl, both the extravesicular and intravesicular pHs were at 7.5.

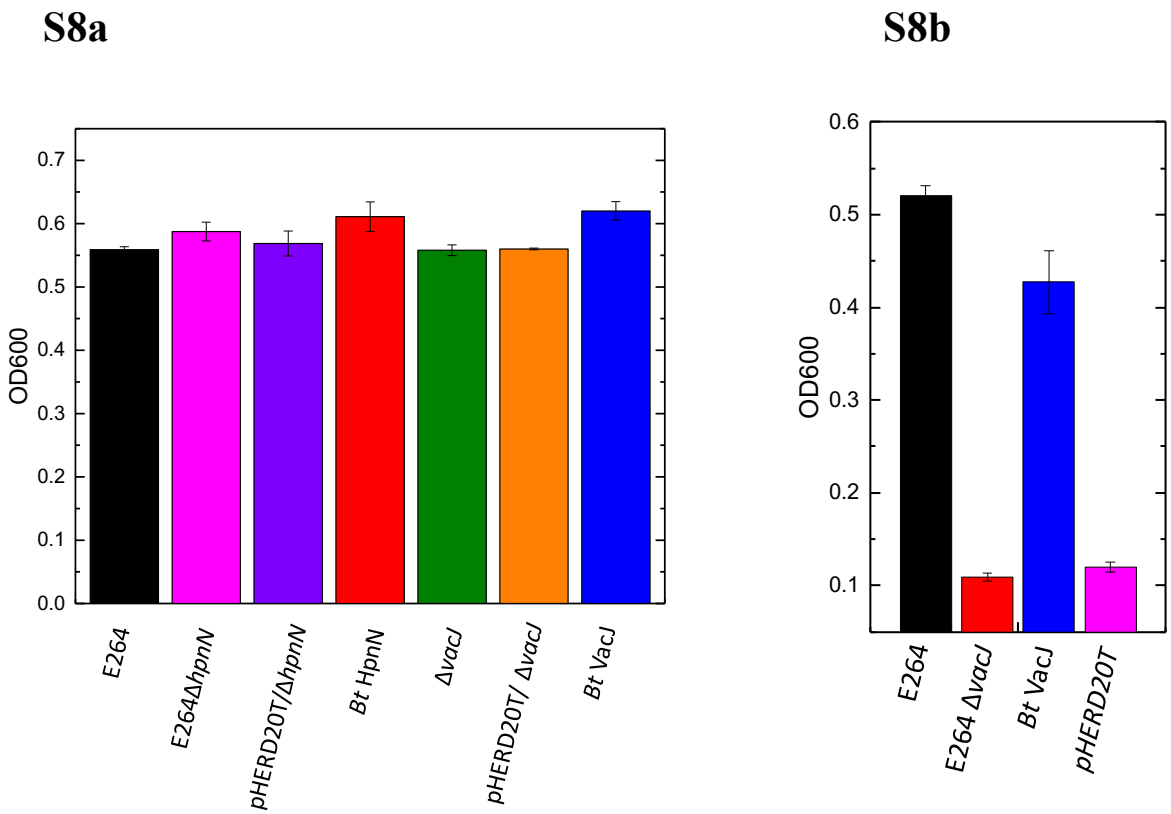


Fig. S8. Growth of cells in the absence and presence of antibiotics. (a) The knockout *B. thailandensis* E264Δ*hpnN* and E264Δ*vacJ* cells, either alone or transformed with the empty vector pHERD20T, were capable of growing in liquid LB (black, E264; magenta, E264Δ*hpnN*; purple, E264Δ*hpnN*/pHERD20T; red, E264Δ*hpnN*/pHERD20TΩ*bt_hpnN*; green, E264Δ*vacJ*;

orange, E264Δ*vacJ*/pHERD20T; blue, E264Δ*hpnN*/pHERD20TΩ*bt_vacJ*. (b) The knockout *B. thailandensis* E264Δ*vacJ* cells, either alone or transformed with the empty vector pHERD20T, were retarded in growth in liquid LB supplemented with 1 mg/ml polymyxin B. Error bars represent standard deviation ($n$ = 3).

## S9

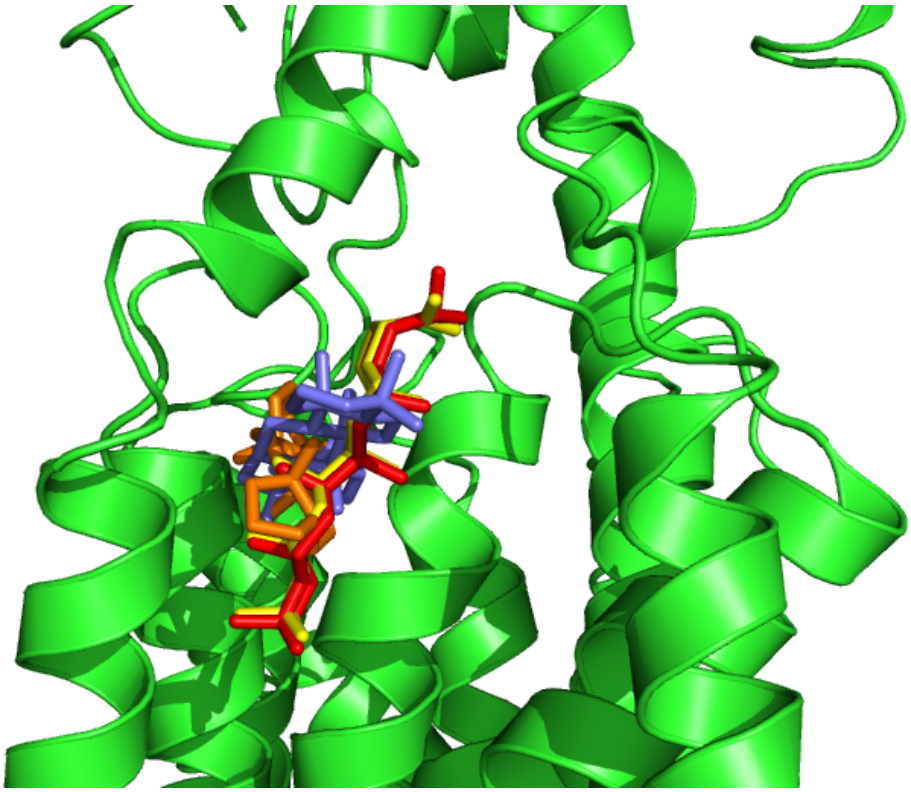

Fig. S9. Binding site prediction for HpnN. The predicted bound diploptene, 17β(H),21β(H)-hopane, 17α(H),21β(H)-hopane, and 17α(H)-22,29,30-trisnorhopan are colored yellow, red, slate and orange, respectively.

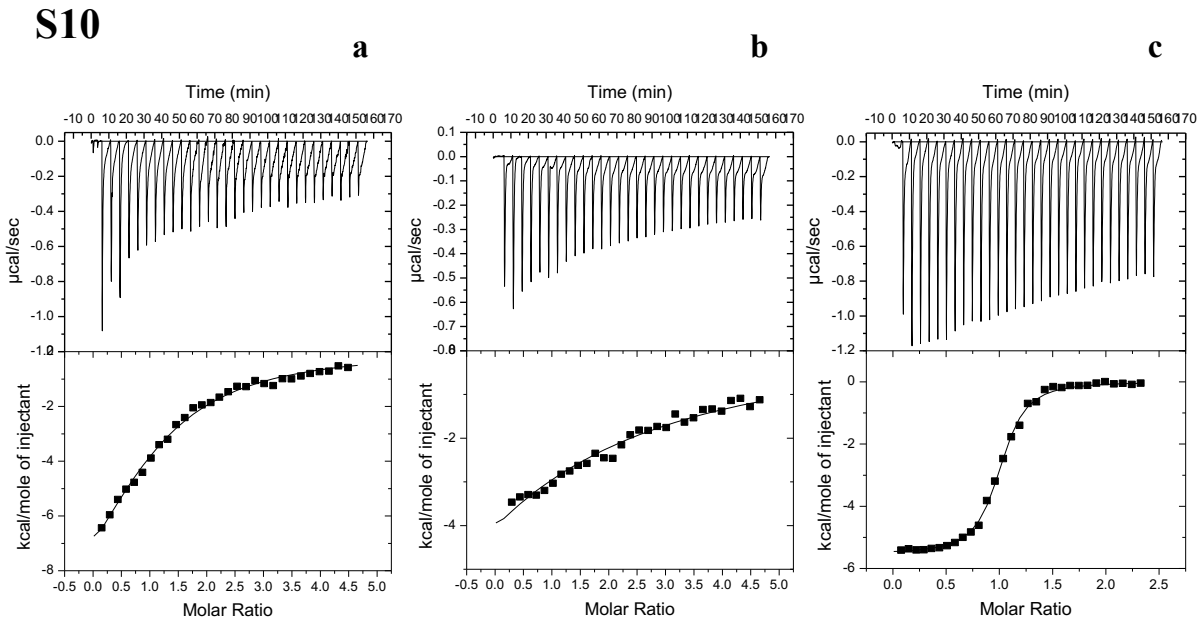


Fig. S10. Isothermal titration calorimetry for the binding of 17β(H),21β(H)-hopane. (a) Representative isothermal titration calorimetry for the binding of 17β(H),21β(H)-hopane to HpnN. (Upper Panel) Each peak corresponds to the injection of 10 µl of 200 µM HpnN in buffer containing 20 mM Tris-HCl pH 7.5, 0.03% DDM and 3% DMSO into the reaction containing 10 µM 17β(H),21β(H)-hopane in the same buffer. (Lower Panel) Cumulative heat of reaction is displayed as a function of the injection number. The solid line is the least-square fit to the experimental data, giving a $K_D$ of 9.1 ± 1.2 µM. (b) Representative isothermal titration calorimetry for the binding of 17β(H),21β(H)-hopane to the L826F mutant. (Upper Panel) Each peak corresponds to the injection of 10 µl of 200 µM L826F in buffer containing 20 mM Tris-HCl pH 7.5, 0.03% DDM and 3% DMSO into the reaction containing 10 µM 17β(H),21β(H)-hopane in the same buffer. (Lower Panel) Cumulative heat of reaction is displayed as a function of the injection number. The solid line is the least-square fit to the experimental data, giving a $K_D$ of 59.2 ± 14.5 µM. (C) Representative isothermal titration calorimetry for the binding of 17β(H),21β(H)-hopane to VacJ. (Upper Panel) Each peak

corresponds to the injection of 10 μl of 200 μM VacJ in buffer containing 20 mM Tris-HCl pH 7.5, 0.03% DDM and 3% DMSO into the reaction containing 10 μM 17β(H),21β(H)-hopane in the same buffer. (Lower Panel) Cumulative heat of reaction is displayed as a function of the injection number. The solid line is the least-square fit to the experimental data, giving a $K_D$ of 0.3 ± 0.02 μM.

**S11**

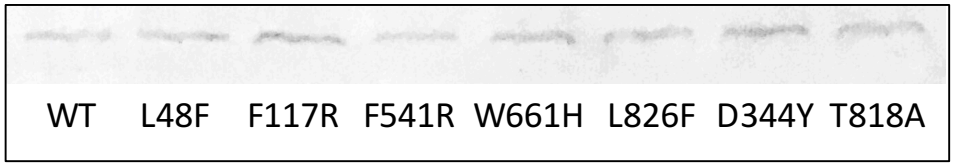


Fig. S11. Expression level of the HpnN transporters. An immunoblot against HpnN of crude extracts from 50 μg dry cells of strain *B. thailandensis* E264Δ*hpnN* expressing the HpnN transporters (wild-type, lane 1; L48F, lane 2; F117R, lane 3; F541R, lane 4; W661H, lane 5; L826F, lane 6; D344Y, lane 7; T818A) is shown.

Table S1. Data collection, phasing and structural refinement statistics of HpnN.

| | Form I | Form II | $[W_6(\mu\text{-}O)_6(\mu\text{-}Cl)_6Cl_6]^{2-}$ | Se (peak) |
|---|---|---|---|---|
| **Data Collection** | | | | |
| Wavelength (Å) | 0.98 | 0.98 | 1.25 | 0.98 |
| Space group | $P2_1$ | $P2_1$ | $P2_1$ | $P2_1$ |
| Resolution (Å) | 100 – 3.39 (3.53 – 3.39) | 100 – 3.77 (3.90 – 3.77) | 100 – 3.42 (3.55 – 3.42) | 100 – 4.80 (4.97 – 4.80) |
| Cell constants (Å) | | | | |
| a | 111.85 | 112.16 | 112.07 | 112.61 |
| b | 130.25 | 143.37 | 131.14 | 146.13 |
| c | 112.06 | 112.66 | 112.09 | 112.57 |
| α, β, γ (°) | 90, 113.6, 90 | 90, 114.1, 90 | 90, 90, 90 | 90, 113.4, 90 |
| Molecules in ASU | 2 | 2 | 2 | 2 |
| Redundancy | 10.5 (10.3) | 3.8 (3.8) | 3.2 (2.6) | 10.5 (4.8) |
| Total reflections | 9,992,420 | 2,649,297 | 48,922 | 1,019,156 |
| Unique reflections | 39,354 | 33,109 | 14,543 | 16,358 |
| Completeness (%) | 99.9 (100) | 99.5 (99.5) | 95.5 (90.7) | 98.6 (98.9) |
| $CC_{½}$ (%) | 99.4 (50.9) | 99.8 (50.9) | 97.5 (58.6) | 99.5 (58.9) |
| I / σ | 12.9 (1.2) | 13.5 (1.1) | 12.0 (1.4) | 13.6 (1.1) |
| **Phasing** | | | | |
| Number of sites | | | 12 | 32 |
| Figure of merit | | | 0.50 | 0.61 |
| **Refinement** | | | | |
| Resolution (Å) | 50 – 3.39 | 50 – 3.77 | | |
| $R_{work}$ (%) | 26.96 | 26.20 | | |
| $R_{free}$ (%) | 32.06 | 30.72 | | |
| RMSD bond lengths (Å) | 0.004 | 0.003 | | |
| RMSD bond angles (°) | 0.691 | 0.637 | | |
| **Ramachandran plot** | | | | |
| most favoured (%) | 91.6 | 90.9 | | |
| additional allowed (%) | 7.5 | 8.3 | | |
| generously allowed (%) | 1.0 | 0.8 | | |
| disallowed (%) | 0 | 0 | | |

Table S2. Data collection of the H90C and Q604C mutants.

| | H90C | Q604C |
|---|---|---|
| **Data Collection** | | |
| Wavelength (Å) | 0.98 | 0.98 |
| Space group | $C222_1$ | $C222_1$ |
| Resolution (Å) | 100 – 3.85 (3.99 – 3.85) | 100 – 4.00 (4.14 – 4.00) |
| Cell constants (Å) | | |
| a | 124.20 | 123.81 |
| b | 189.77 | 189.19 |
| c | 142.49 | 143.25 |
| α, β, γ (°) | 90, 90, 90 | 90, 90, 90 |
| Molecules in ASU | 1 | 1 |
| Redundancy | 12.2 (8.8) | 8.8 (8.1) |
| Total reflections | 5,333,281 | 1.063,659 |
| Unique reflections | 15,969 | 14,594 |
| Completeness (%) | 97.4 (85.4) | 100 (100) |
| $CC_{½}$ (%) | 99.4 (75.7) | 99.7 (67.4) |
| I / σ | 21.2 (1.5) | 17.8 (1.5) |

Table S3. Thermodynamic parameters for 17β(H),21β(H)-hopane binding.

| | $K_D$ (μM) | ΔH (kcal/mol) | ΔS (cal•mol•deg$^{-1}$) | N |
|---|---|---|---|---|
| HpnN | 9.1 ±1.2 | -12.5 ± 1.0 | -19.0 | 1.08 ± 0.07 |
| L826F | 59.2 ± 14.5 | -26.0 ± 9.0 | -67.7 | 1.06 ± 0.16 |
| VacJ | 0.3 ± 0.02 | -5.5 ± 36.7 | 11.3 | 0.99 ± 0.01 |

Table S4. Primers for site-directed mutagenesis.

| Primer | Sequence |
|---|---|
| L48 forward | 5′-CATCAGCAAGTTCGTCGAGAACGACCCGAAATG-3′ |
| L48 reverse | 5′-CGTTCTCGACGAACTTGCTGATGTCGGTGTTG-3′ |
| F117R forward | 5′-CCGCTCCACGAGCACGACGGGCTGCTG-3′ |
| F117R reverse | 5′-GTCGTGCTCGTGGAGCGGGCCGCCTCC-3′ |
| D344Y forward | 5′-CTCGGCGTCTATTTCGCGATCCAGTACGGCGTC-3′ |
| D344Y reverse | 5′-GATCGCGAAATAGACGCCGAGACCGACGAAC-3′ |
| F541R forward | 5′-GCTGTCGACCCGCATTCCCGATGCGCAGCC-3′ |
| F541R reverse | 5′-CATCGGGAATGCGGGTCGACAGCGTCGTCGTG-3′ |
| W661H forward | 5′-CGTGCGCGACCATGTCGCGCCGGACGGCC-3′ |
| W661H reverse | 5′-GTCCGGCGCGACATGGTCGCGCACGATCTGCGG-3′ |
| T818A forward | 5′-CAGCGCCGCGGCGACGGCCACCGCGTTCG-3′ |
| T818A reverse | 5′-GTGGCCGTCGCCGCGGCGCTGAACAGCAC-3′ |
| T819A forward | 5′-CAGCGCCGCGACGGCTGCCACCGCGTTCGGCAGC-3′ |
| T819A reverse | 5′-GAACGCGGTGGCAGCCGTCGCGGCGCTGAACAGC-3′ |
| L826F forward | 5′-GTTCGGCAGCTTTTGGCTGTCGCATCATCCG-3′ |
| L826F reverse | 5′-CGACAGCCAAAAGCTGCCGAACGCGGTGG-3′ |

# CHAPTER 4. STRUCTURES AND TRANSPORT DYNAMICS OF A MULTIDRUG EFFLUX PUMP

A manuscript in preparation

Chih-Chia Su[1,ψ], Nitin Kumar[2,ψ], Linxiang Yin[3,ψ], Abhijith Radhakrishnan[2], Tsung-Han Chou[1], Lei Dai[4], Jared A. Delmar[1], Qijing Zhang[4], Yeon-Kyun Shin[3] and Edward W. Yu[1,2*]

[1]Department of Physics and Astronomy, Iowa State University, IA 50011, USA

[2]Department of Chemistry, Iowa State University, Ames, IA 50011, USA

[3]Department of Biochemistry, Biophysics and Molecular Biology, Iowa State University, Ames, IA 50011, USA

[4]Department of Veterinary Microbiology, College of Veterinary Medicine, Iowa State University, Ames, IA 50011, USA

[ψ]C.S., N.K. and L.Y. contributed equally to this work.

* To whom correspondence should be addressed. E-mail: ewyu@iastate.edu

## Abstract

Resistance-nodulation-cell division (RND) efflux pumps are integral membrane proteins that catalyze the export of substrates across cell membranes. Within the hydrophobe/amphiphile efflux (HAE) subfamily, these RND proteins largely form trimeric efflux pumps. The drug efflux process has been proposed to entail a synchronized motion between subunits of the trimer to advance the transport cycle, leading to the extrusion of drug molecules. Here we use X-ray crystallography and single-molecule fluorescence resonance energy transfer (sm-FRET) imaging to elucidate the structures and functional dynamics of the *Campylobacter jejuni* CmeB multidrug efflux pump. We find that the CmeB trimer displays a very unique conformation. A direct observation of transport dynamics in individual CmeB trimers embedded in membrane vesicles indicates that each CmeB subunit undergoes conformational transitions uncoordinated and independent of each other. Further analyses allow us to propose a simple model for transport mechanism that the CmeB protomers function independently within the trimer.


## Introduction

*Campylobacter jejuni* is a major causative agent of human enterocolitis and is responsible for more than 400 million cases each year worldwide (*1, 2*). The infection can trigger an autoimmune response that is associated with the development of Guillain-Barre syndrome, an acute flaccid paralysis caused by degeneration of the peripheral nervous system (*2*). *C. jejuni* is widely distributed in the intestinal tracts of animals and is transmitted to humans via contaminated food, water or raw milk. Fluoroquinolones and macrolides are frequently prescribed for the treatment of human campylobacteriosis (*3*). Unfortunately, *Campylobacter* has developed resistance to these antimicrobials, especially fluoroquinolones (*4-6*). Recently, the Centers for Disease Control and Prevention have designated antibiotic-

resistant *Campylobacter* as a serious antibiotic resistance threat in the USA. Resistance of *Campylobacter* to antibiotics is mediated by multiple mechanisms (*5, 7*). However, multidrug efflux is an effective mechanism and one of the major causes of failure of drug-based treatments of infectious diseases. In *C. jejuni*, these multidrug efflux pumps contribute significantly to both intrinsic and acquired resistance to a broad range of antimicrobials and toxic compounds. Antibiotic resistance not only compromises the effectiveness of clinical therapy, but also affects the duration of clinical treatment. It has been shown that acquisition of fluoroquinolone resistance confers a fitness advantage on *C. jejuni* in the animal host (*8*). Thus, novel strategies are needed to combat antibiotic resistant *Campylobacter*.

The best characterized multidrug efflux system in *C. jejuni* is the Cme (*Campylobacter* multidrug efflux) tripartite system (*9-11*). The Cme locus consists of three tandemly linked genes (*cmeABC*) encoding protein components of the tripartite Cme efflux pump (CmeA, CmeB and CmeC), where all three components are absolutely required for substrate expulsion. This tripartite system is composed of the CmeB efflux pump, an inner membrane resistance-nodulation-cell division (RND) (*12*) transport protein that contains substrate binding sites and transduces the electrochemical energy required for pumping drugs out of the cell; the CmeA periplasmic protein, a member of the membrane fusion protein family; and the CmeC outer membrane associated protein that is integral to the outer membrane. Mutations on this tripartite system have been found to have a drastic effect on drug susceptibility (*9, 13*).

To understand the transport mechanism of the CmeB efflux pump from *C. jejuni*, we here define the X-ray structures of this membrane protein, which assembles as a trimer. Using sm-FRET imaging, we demonstrate that each CmeB protomer within the trimer is able to export drugs independently.

## Results

### Overall structure of CmeB

Two distinct conformations of CmeB with space groups C2 (form I) and P1 (form II) were captured in two different forms of crystals (Figs.1, S1, S2 and Table 1). Overall, CmeB adopts the fold of a typical RND-type protein and forms a homotrimer, with its pseudo threefold symmetrical axis positioning perpendicular to the membrane surface. Each subunit of CmeB contains 12 transmembrane helices (TM1-TM12) and a large periplasmic domain created by two extracellular loops between TM1 and TM2, and between TM7 and TM8, respectively. This periplasmic domain can be divided into six subdomains: PN1, PN2, PC1, PC2, DN and DC (Fig. 1a). Subdomains PN1, PN2, PC1 and PC2 form the pore domain, with PN1 making up the central pore and stabilizing the trimeric organization. Subdomains DN and DC, however, contribute to form the docking domain of the pump.

A cleft is formed between subdomains PC1 and PC2. This cleft creates an entrance, allowing for substrates to move into the pump through the periplasm. Deep inside the cleft, the CmeB pump forms a large internal cavity. In AcrB, this cavity has been shown to form an important binding site, which plays a predominant role in recognizing substrates for export (*14, 15*). Recently, a drug resistance-enhanced variant of CmeB has been identified in clinical isolates of *C. jejuni*. This mutant pump is able to confer high-level bacterial resistance to multiple antibiotics, including chloramphenicol, ciprofloxacin, erythromycin and tetracycline (Yao et al., 2016). Interestingly, 22 mutated residues are found to localize within this drug-binding cavity. The corresponding amino acids of many of these mutated residues, including M607L, A152D, T88Q, M292I and M571L, have been observed to be critical for multidrug binding in AcrB (*14, 15*).

The structures of AcrB indicate that this multidrug efflux pump is capable of forming an asymmetric trimer, in which the three protomers are distinct and display different

conformational states (“access”, “binding” and “extrusion”) (*14, 16, 17*). This structural dissimilarity has led to a proposed transport mechanism that the three protomers of an RND transporter must cooperate and synchronize to go through these three different states to export drugs. In both the “access” and “binding” protomers of AcrB, the periplasmic cleft created by subdomains PC1 and PC2 are open. However, this cleft is closed in the “extrusion” protomer. Thus, the asymmetric trimer of AcrB features a conformational state of two periplasmic clefts open and one cleft closed. During drug binding and extrusion, it was proposed that the three periplasmic clefts within the trimer have to open and close accordingly in order to advance the transport cycle.

Both crystal structures of CmeB depict that this pump also forms an asymmetric trimer. In the form I structure, the three periplasmic clefts of the CmeB trimer are closed (Fig. 1b). Although the conformations of the three monomers are different from each other, they are more similar to the “extrusion” form of AcrB. A channel for extrusion is found in each protomer of our form I structure (Fig. 2a and b). We therefore assigned the conformational state of these three protomers as the “extrusion” form.

Surprisingly, in the form II structure, the periplasmic cleft of one of the protomers is open (Fig. 1c), albeit similar to the conformation of the “binding” state of AcrB. An elongated channel is found in the periplasmic domain of this protomer. It was observed that this channel leads through the opening of the periplasmic cleft, exposed to solvent in the periplasm (Fig. 2c and d). We labeled this conformer as the “binding” form of CmeB. However, the periplasmic clefts of the other two protomers are closed in conformation. One of these two CmeB molecules is more related to the structure of the “extrusion” conformers of the form I structure. Like the three protomers of the form I structure, the periplasmic domain of this conformer also creates an extrusion channel (Fig. 2c and d). Thus, this conformer was classified as the “extrusion” form. Interestingly, the other CmeB molecule displays a distinct conformation,

forming a new state that is different from the "extrusion" form. No channel was found in this conformer (Fig. 2c and d). This conformation probably represents one of the intermediates that the CmeB pump must go through during the transport cycle. However, the conformation of this protomer is similar to the "resting" state of apo-CusA (*18, 19*), a specific heavy-metal RND efflux pump that recognizes Cu(I) and Ag(I) ions. We thus designated this conformation as the "resting" state of the CmeB efflux pump.

Our structures of CmeB do not show the typical conformation of an asymmetric trimer with two periplasmic clefts open and one cleft closed. We then went through the existing crystal structures of these RND proteins, including AcrB (*14, 15, 20-22*), MexB (*23*), MtrD (*24*) and CusA (*18, 25*), available in the protein data bank. We found that the trimer can have three periplasmic clefts open or closed at a time, in addition to the asymmetric conformation of the AcrB trimer (Fig. S3). Based on this structural information, we postulated that individual protomers of these trimeric RND pumps could bind and export substrates independently instead of operating in a synchronized fashion. Thus, each protomer may autonomously go through a sequence of conformational transitions, which lead to the extrusion of substrates through a particular protomer. This is evidenced through the heterotrimeric $MdtB_2C$ efflux pump, where the MdtB and MdtC subunits function differently (*26*). It was found that MdtC is likely to be responsible for recognizing and transporting drugs by itself within the heterotrimeric efflux pump (*26*). Thus, the structures of individual protomers of AcrB and CmeB captured by crystallography may simply reflect the conformation of various transient states that these protomers may go through within the transport cycle. To this point, the conformations of the three protomers within the trimeric pump can be identical with three periplasmic clefts open or closed as shown in the case of the symmetric structures of AcrB (*20*) and CusA (*18*). However, the structures of individual protomers of the trimeric pump can also be distinct from each other as indicated in the cases of the asymmetric AcrB structures (*14, 16,*

*17*), where the three protomers are in different transient states with two open and one closed periplasmic clefts within the trimer. For the asymmetric CmeB trimer, the conformations of the three protomers display in such a way that either only one out of the three periplasmic clefts is open or all of these clefts are closed.

**Single-molecule FRET studies**

To elucidate if a CmeB protomer can export drugs individually within the trimer, we decided to directly observe the transport dynamics and conformational changes of the periplasmic domain movements using total internal reflection sm-FRET imaging. Based on the crystal structures of CmeB, we introduced a single cysteine mutation at a position of high solvent accessibility as well as low sequence conservation. The resulting three cysteine residues within each CmeB trimer were derivatized with a mixture of maleimide-activatived Alexa Fluor 546 (AF546) and Alexa Fluor 647 (AF647), which served as a molecular ruler for measuring the distance between two inter-subunit cysteines. As CmeB is a proton-motive-force (PMF)-dependent transporter, we reconstituted the purified and derivatized CmeB protein into liposomes, where we could generate the proton gradient required for substrate translocation. These proteoliposomes were immobilized on streptavidin-decorated surfaces for FRET signal recording (Fig. 3a).

We chose to mutate residue K843 to a cysteine in order to anchor the dyes. This residue is located right outside subdomain PC2, facing the periplasm, and at a position where the inter-subunit distances are quite different between the conformations as suggested by the crystal structures (Fig. 3b and c). We selected the CmeB trimers that only contained one donor (AF546) and one acceptor (AF647) dyes for FRET measurements. If CmeB functions by means of the proposed rotating mechanism (*14, 16, 17*), sequentially transitioning through three different states, then the distance between the two inter-subunit K843 residues should

sequentially vary in a manner of ~74 Å, ~79 Å and ~69 Å, respectively. This should lead to the observation of three distinct signals, which correspond to the intermediate-, low- and high-FRET states, in the FRET trajectory and transition density plot (Fig. 3d and e). However, if CmeB employs a different mechanism to recognize and export substrates, the characteristic of this transition density plot should be different.

We adjusted the inter- and intra-vesicular pHs to 6.5 and 7.5, respectively. We then performed sm-FRET experiments both in the absence and presence of 1 or 10 μM taurodeoxycholate (Tdc), which is the CmeB substrate. In the absence and presence of Tdc, the FRET state values are very similar. We also find that the frequency of transitions is more or less the same with and without the substrate Tdc. The majority of the populations of apo-CmeB are largely in favor of the low FRET state. However, the addition of substrates seems to shift the state occupancies more favorable to the higher FRET states (Fig. 4). At least four distinct states can be observed, indicating that the trimeric pump is transitioning between various states. These four states are labeled as low (L), intermediate-1 ($I_1$), intermediate-2 ($I_2$) and high (H) FRET states, which correspond to ~0.20, ~0.35, ~0.45 and ~0.60 FRET efficiencies. Interestingly, our sm-FRET data do not seem to agree with the proposed rotating mechanism. Based on the traces and symmetrical nature of the density plots, it is more likely that the three protomers function independently of each other.

Drug export by RND transporters depends upon the PMF (*12*). In the transmembrane region of CmeB, the conserved charged residues D409, D410 and K935 form a salt-bridge triad, which most probably establishes the proton-relay network and relays proton translocation for energy coupling. A single point mutation on these corresponding residues in MexB (*27*), AcrB (*28*) and CusA (*18, 25*) has been found to impair the function of these pumps. To disrupt this proton relay network in the CmeB pump, we replaced D409 by an alanine to form a K843C-D409A double-point mutant. This double-point mutant was then purified, derivatized

with AF546 and AF647 and reconstituted into liposomes for FRET signal recording. Again, all of these sm-FRET experiments were done in the presence of a proton gradient with the inter- and intra-vesicular pHs at 6.5 and 7.5, respectively. As expected, this double mutant did not show much activity in terms of its dynamic movement. In the absence of Tdc, the frequency of transitions of the K843C-D409A mutant was reduced by at least seven times compared with that of the K843C transporter. Within 20 min of FRET trajectories, the data contain only 139 transitions for the K843C-D409A double mutant. Most of the population of this K843C-D409A mutant is found to cluster in the low FRET state regardless of the presence of ligand (Fig. 5). This low FRET state is also seen in the K843C mutant. The FRET data indicate that the distance between the donor and acceptor dyes at this low FRET state is ~85 Å, corresponding to the 0.2 FRET efficiency. This distance is significantly longer than the distances observed in our crystal structures. However, this distance is similar to that depicted in the crystal structure of the "resting" state of apo-CusA (*18, 19*). In this state, the three periplasmic clefts of the CusA heavy-metal efflux pump are closed within the trimer. The data suggest that the CmeB protomers may prefer the "resting" conformation, in the absence of the PMF, and the process of transitioning from the "resting" to "binding" states may be energy dependent.

Hidden Markov modeling (HMM) (*29*) was then used to quantify the transition rates of these various FRET states. In the absence of Tdc, the transition density plot of the K843C mutant indicates that the predominant FRET transitions are L → $I_1$ and $I_1$ → L, which correspond to the reversible transitions between the "resting-resting" and "resting-binding" subunits. A histogram derived from a population of dwell times was fitted with a single exponential decay, resulting in $k_{L \rightarrow II} = 1.64\ s^{-1}$ (0.61 s) and $k_{II \rightarrow L} = 3.22\ s^{-1}$ (0.31 s) transition

rates for the processes “resting-resting” → “resting-binding” and “resting-binding” → “resting-resting”, respectively (Table 2 and Fig. S4). The data suggest that the kinetics of CmeB are quite simple and can be described with a single rate constant.

In the presence of 1 μM Tdc, there is a significant decrease in the reverse transition $I_1$ → L. The rate for this reverse transition is $k_{I1 \rightarrow L}$ = 1.82 $s^{-1}$ (0.55 s), which is almost two times slower than the same process without the substrate. In addition, there is a substantial increase in the forward transition $I_1$ → $I_2$, suggesting that the K843C mutant may prefer to advance the transport cycle by shifting the “resting-binding” to “resting-extrusion” or “binding-binding” states. Apparently, this process is reversible as indicated by the observation of the reverse transition $I_2$ → $I_1$. The forward and reverse transition rates were calculated to be $k_{I1 \rightarrow I2}$ = 1.61 $s^{-1}$ (0.62 s) and $k_{I2 \rightarrow I1}$ = 3.45 $s^{-1}$ (0.29 s), respectively (Table 2 and Fig. S5).

As the Tdc concentration increased to 10 μM, the transition between $I_2$ and H was observed, suggesting that the transporter continues to move forward the transport cycle by switching from the “resting-extrusion” to the “binding-extrusion” forms. This process is also reversible and the transition rates for these forward and reverse processes are $k_{I2 \rightarrow H}$ = 1.59 $s^{-1}$ (0.63 s) and $k_{H \rightarrow I2}$ = 2.86 $s^{-1}$ (0.35 s) (Table 2 and Fig. S6).

For the K843C-D409A mutant pump, the density plots are much simpler and their characteristics are more or less the same regardless of the presence of Tdc. Both in the absence and presence of substrate, the only observed transitions are the reversible conformational change between the “resting-resting” and “resting-binding” forms, as indicated by the L → $I_1$ and $I_1$ → L transitions. However, the rates of forward transitions are much slower than those for the K843C mutant. Specifically, in the absence of Tdc, the rates for the forward and reverse transitions in the K843C-D409A pump are $k_{L \rightarrow I1}$ = 0.54 $s^{-1}$ (1.85 s) and $k_{I1 \rightarrow L}$ = 2.86 $s^{-1}$ (0.35 s)

(Table 2 and Fig. S7), suggesting that the transition process "resting-resting" → "resting-binding" may be energy dependent and needs to couple with the PMF. All of these observed transition rates are listed in Table 2.

We have defined the crystal structures of CmeB and directly observed the transport dynamics of this membrane protein reconstituted in proteoliposomes at the single-molecule level. These data lead us to propose a simple model for the CmeB transport mechanism (Fig. 6), in which the protomers export substrates independently of each other within the trimer. In the absence of the PMF, the CmeB protomers may prefer the "resting" conformation, which is evidenced through our FRET data that the inter-subunit distance of the K843C-D409A double mutant measured between the two K843 residues is relatively long in comparison with that of the K843C mutant. It was found that there are relatively very little motions going on in this double mutant, suggesting that a transition from the "resting" to "binding" states may need to couple with the PMF. In the presence of the PMF, it appears that there are a few more observed transitions, suggesting that the pump can easily continue to advance the transport cycle by coupling with the proton-relay network. Our data indicate that the CmeB protomers can independently progress to "binding" and then "extrusion" conformations. The populations of these two states can be greatly enhanced by the addition of the Tdc ligand. Our data allow us to uncover the mechanism of drug export, where the three CmeB subunits undergo conformational changes independently of each other.

## Accession Code

Atomic coordinates and structure factors for the structures of CmeB have been deposited at the RCSB Protein Data Bank with accession codes 5T0O (form I) and 5LQ3 (form II).

**Acknowledgements**

This work was supported by NIH Grants R01AI114629 (E.W.Y.), R01GM051290 (Y.K.S.) and R01AI118283 (Q.Z.).

## Materials and Methods

### Cloning, expression and purification of the CmeB efflux pump

The full-length CmeB membrane protein containing a 6xHis tag at the N-terminus was overproduced in *E. coli* BL21(DE3)*ΔacrB* cells, which harbors a deletion in the chromosomal *acrB* gene, possessing pET15bΩ*cmeB*. Cells were grown in 12 L of LB medium with 100 μg/ml ampicillin at 37°C. When the $OD_{600}$ reached 0.5, the culture was treated with 1 mM IPTG to induce *cmeB* expression, and cells were harvested within 3 h. The collected bacteria were resuspended in low salt buffer containing 100 mM sodium phosphate (pH 7.2), 10 % glycerol, 1 mM ethylenediaminetetraacetic acid (EDTA) and 1 mM phenylmethanesulfonyl fluoride (PMSF), and then disrupted with a French pressure cell. The membrane fraction was collected and washed twice with high salt buffer containing 20 mM sodium phosphate (pH 7.2), 2 M KCl, 10 % glycerol, 1 mM EDTA and 1 mM PMSF, and once with 20 mM HEPES-NaOH buffer (pH 7.5) containing 1 mM PMSF. The membrane protein was then solubilized in 1 % (w/v) 6-cyclohexyl-1-hexyl-β-D-maltoside (Cymal-6). Insoluble material was removed by ultracentrifugation at 100,000 x g. The extracted protein was purified with a $Ni^{2+}$-affinity column. The purity of the CmeB protein (>95%) was judged using 10% SDS-PAGE stained with Coomassie Brilliant Blue. The purified protein was then dialyzed and concentrated to 20 mg/ml in a buffer containing 20 mM Na-HEPES (pH 7.5) and 0.05% Cymal-6.

**Crystallization of CmeB**

The 6xHis CmeB crystals were grown at room temperature using sitting-drop vapor diffusion with the following procedures. For the form I crystals, a 2 μl protein solution containing 20 mg/ml CmeB protein in 20 mM Na-HEPES (pH 7.5) and 0.05% (w/v) Cymal-6 was mixed with a 2 μl of reservoir solution containing 4% PEG 8000, 0.1 M Na-MES (pH 6.5) and 0.1 M $MgSO_4$. Similarly, the form II crystals were crystallized in reservoir solution containing 6% PEG 8000, 50 mM M Na-MES (pH 6.5) and 60 mM $MnCl_2$.The resultant mixture was equilibrated against 500 μl of the reservoir solution. Crystals of both forms I and II grew to a full size in the drops within a month. Typically, the dimensions of the crystals were 0.2 mm x 0.2 mm x 0.2 mm. Cryoprotection was achieved by raising the glycerol concentration stepwise to 25% with a 5% increment in each step.

**Data collection, structural determination and refinement**

All diffraction data were collected at 100K at beamline 24ID-C located at the Advanced Photon Source, using a Platus 6M detector. Diffraction data were processed using DENZO and scaled using SCALEPACK (*30*).

The form I crystals of CmeB belong to space group C2 (Table S1). Based on the molecular weight of CmeB (114.99 kDa), three molecules per asymmetric unit with a solvent content of 67.7% were expected. The structure of CmeB was phased using molecular replacement, utilizing the structure of AcrB (*14*) as a search model. After tracing the initial model manually using the program Coot (*31*), the model was refined against the native data at 3.15 Å-resolution using TLS refinement techniques adopting a single TLS body as implemented in PHENIX (*32*) leaving 5% of reflections in Free-R set. Iterations of refinement

were done using PHENIX (*32*) and CNS (*33*). Model building was performed using Coot (*31*). The final model of the CmeB pump consists of 3,105 residues in the asymmetric unit with excellent geometrical characteristics (Table S1).

The form II crystals took the space group P1 (Table S1). This structure was determined using molecular replacement, utilizing the structure of form I as an initial search model. After tracing the initial model using the program Coot (*31*), the model was refined against the native data at 3.63 Å-resolution. The remaining procedures for model building and structural refinement were identical to those for the form I structure.

**Protein reconstitution into lipopsomes**

Single cysteine mutations were introduced to produce a cysteineless CmeB variant, in which the three natural cysteine residues located in the transmembrane region have been replaced with serines, using site-directed mutagenesis. Constructs were verified by DNA sequencing and transformed into *E. coli* BL21(DE3)Δ*acrB* cells. Proteins were expressed as N-terminal 6xHis fusions and purified as described above. The purified proteins were then dialyzed, concentrated to 20 μM in a buffer containing 20 mM Na-HEPES (pH 7.5) and 0.03% DDM, and labeled with a mixture of maleimide-activated AF546 and AF647 at final concentrations of 20 and 100 μM, respectively. Labeled proteins were quenched with 10 mM 2-mercaptoethanol and subsequently purified away from excess reagents using size exclusion chromatography.

The labeled CmeB variants were reconstituted into liposomes made of 74.5% *E. coli* total lipid, 24.5% egg-yolk phosphatidylcholine and 1% 1,2-dioleoyl-*sn*-glycero-3-phosphoethanolamine-N-(cap biotinyl) (biotin-DOPE) (Avanti Polar Lipids, Alabaster, AL) in a buffer containing 20 mM Na-HEPES (pH 7.5). Each CmeB variant was mixed with unilamellar liposomes in 20 mM Na-HEPES (pH 7.5) and 0.2% n-dodecyl-β-D-maltoside

(DDM) at a protein-to-lipid ratio of 1:10,000 (w/w) to ensure a high probability of having only one single CmeB trimer per liposome. The liposome/protein mixture was incubated for 1 hour at room temperature under gentle agitation. Subsequently, this mixture was diluted stepwise three times within 45 min. The final concentration of DDM should be below the critical micelle concentration of ~0.008%. Detergents were then removed by SM2 Biobeads (Bio-Rad) and PD-10 desalting column (GE Healthcare Bio-Sciences, Pittsburgh, PA).

**Single-molecule FRET experiments**

All sm-FRET experiments were performed using a home-built prism-based total internal reflection fluorescence microscope constructed around an inverted microscope body (Olympus IX71). The samples were illuminated with a 532 nm solid-state laser to excite the AF546 donor dye. A 635 nm helium-neon laser was used to ensure the presence of the AF647 acceptor dye. The AF546 and AF647 fluorescence signals were collected using a water-immersion lens (Olympus UPLSAPO 60XW) and separated using a dichroic mirror (Chroma T6601pxr). Imaging data were acquired using smCamera acquisition software and an electron-multiplying charged-coupled device camera (Andor Technology iXon3 DU879E).
Quartz slide (Chemglass Life Sciences, Vineland, NJ) and micro cover glass (VWR Life Sciences, Radnor, PA) were extensively cleaned and functionalized by coating the surface with methoxy-PEG-5000 and Biotin-PEG- 5000 (100:1) (Laysan Bio, Arab, AL). These slides and cover glasses were assembled to form a flow-cell device. This flow cell was then incubated with a solution containing 20 mM Na-HEPES (pH 7.5) and 100 μg/ml streptavidin from *Streptomyces avidinii* (Sigma-Aldrich, St. Louis, MO) for 5 min. Unbound streptavidin was subsequently washed out with 20 mM Na-HEPES (pH 7.5). Next, a suspension of proteoliposomes (100 μg/ml lipid concentration) extruded through a 100-nm pore-size

polycarbonate filter (GE Healthcare Bio-Sciences, Pittsburgh, PA) was flushed in, followed by a 4-min incubation to allow the liposomes to adhere to the surface. Unbound proteoliposomes were washed away with buffer containing 20 mM Na-HEPES (pH 7.5).

All imaging experiments were performed in solution containing 20 mM HEPES (pH 6.5), 2 mM cyclooctatetraene (Sigma-Aldrich, St. Louis, MO) and 5 mM β-mercaptoethanol (Sigma-Aldrich, St. Louis, MO). To avoid unwanted pH drop causing by common enzymatic oxygen scavengers, such as glucose oxidase and catalase and protocatechuate dioxygenase, during data collection, we used a pH stable pyranose oxidase and catalase (*34*) in all of our experiments. Thus, the solution was supplemented with a pH stable enzymatic oxygen scavenger system comprising 3 units/ml pyranose oxidase, 8 units/ml catalase and 0.8% glucose (Sigma-Aldrich, St. Louis, MO). All data were collected at an imaging rate of 10 $s^{-1}$ (100 ms integration time). At the beginning of each experiment, a 10 s (100 frames) movie was recorded with an alternation of 532-nm and 637-nm excitation. This alternating laser excitation (ALEX) scheme (*35*) allowed us to separate the fluorescence contributions of the green and red dyes, thus permitting us to identify the CmeB trimers that contain only one green and one red dyes.

**Single-molecule FRET data analysis.**

The movies acquired in single-molecule imaging were processed with smCamera program (https://cplc.illinois.edu/software/) to identify and extract donor and acceptor fluorescence intensity profiles of individual molecules. Traces extracted from the movies were interactively selected with the following criteria: (i) only a single AF546 and a single AF647 dyes in a proteoliposome determined by the alternating laser excitation (ALEX) scheme (*35*) was used; (ii) no more than one bleaching step for the donor and acceptor fluorophores was allowed; (iii) only those data indicate a clear anti-correlated pattern between the donor and

acceptor fluorescence intensities were used; and (iv) vesicles that contain a constant total fluorescence intensity from the donor and acceptor before photobleaching were selected. The FRET trajectories were calculated from the acquired intensities, $I_{AF546}$ and $I_{AF647}$, using the formula FRET = $I_{AF647}/(I_{AF546} + I_{AF647})$. Individual single-molecule traces were analyzed using HaMMy (*29*) to generate idealized traces. Transition density plots (TDPs) were generated using the MATLAB code (*36*), which was kindly provided by Professor Jong-Bong Lee from POSTECH, Korea. The histograms were calculated using the Origin Pro software (OriginLab, Northampton, MA). The bin size of all sm-FRET histograms was set at 0.02.

## References


1. G. M. Ruiz-Palacios, in *Clin Infect Dis*. (United States, 2007), vol. 44, pp. 701-703.

2. P. A. van Doorn, L. Ruts, B. C. Jacobs, Clinical features, pathogenesis, and treatment of Guillain-Barre syndrome. *Lancet Neurol* **7**, 939-950 (2008).

3. M. J. Blaser, J. Engberg, in *Campylobacter, Third Edition*. (American Society of Microbiology, 2008), pp. 99-121.

4. A. Gibreel, D. E. Taylor, Macrolide resistance in Campylobacter jejuni and Campylobacter coli. *J Antimicrob Chemother* **58**, 243-255 (2006).

5. T. Luangtongkum *et al.*, Antibiotic resistance in Campylobacter: emergence, transmission and persistence. *Future Microbiol* **4**, 189-200 (2009).

6. J. Engberg, F. M. Aarestrup, D. E. Taylor, P. Gerner-Smidt, I. Nachamkin, Quinolone and macrolide resistance in Campylobacter jejuni and C. coli: resistance mechanisms and trends in human isolates. *Emerg Infect Dis* **7**, 24-34 (2001).

7. D. E. Taylor, P. Courvalin, Mechanisms of antibiotic resistance in Campylobacter species. *Antimicrobial Agents and Chemotherapy* **32**, 1107 (1988).

8. N. Luo *et al.*, Enhanced in vivo fitness of fluoroquinolone-resistant Campylobacter jejuni in the absence of antibiotic selection pressure. *Proc Natl Acad Sci U S A* **102**, 541-546 (2005).

9. J. Lin, L. O. Michel, Q. Zhang, CmeABC functions as a multidrug efflux system in Campylobacter jejuni. *Antimicrobial agents and chemotherapy* **46**, 2124-2131 (2002).

10. J. Lin, O. Sahin, L. O. Michel, Q. Zhang, Critical role of multidrug efflux pump CmeABC in bile resistance and in vivo colonization of Campylobacter jejuni. *Infect Immun* **71**, 4250-4259 (2003).

11. L. Pumbwe, L. J. Piddock, Identification and molecular characterisation of CmeB, a Campylobacter jejuni multidrug efflux pump. *FEMS Microbiol Lett* **206**, 185-189 (2002).

12. T. T. Tseng *et al.*, The RND permease superfamily: an ancient, ubiquitous and diverse family that includes human disease and development proteins. *J Mol Microbiol Biotechnol* **1**, 107-125 (1999).

13. M. Yan, O. Sahin, J. Lin, Q. Zhang, Role of the CmeABC efflux pump in the emergence of fluoroquinolone-resistant Campylobacter under selection pressure. *J Antimicrob Chemother* **58**, 1154-1159 (2006).

14. S. Murakami, R. Nakashima, E. Yamashita, T. Matsumoto, A. Yamaguchi, Crystal structures of a multidrug transporter reveal a functionally rotating mechanism. *Nature* **443**, 173-179 (2006).

15. R. Nakashima, K. Sakurai, S. Yamasaki, K. Nishino, A. Yamaguchi, Structures of the multidrug exporter AcrB reveal a proximal multisite drug-binding pocket. *Nature* **480**, 565-569 (2011).

16. M. A. Seeger *et al.*, Structural asymmetry of AcrB trimer suggests a peristaltic pump mechanism. *Science* **313**, 1295-1298 (2006).

17. G. Sennhauser, P. Amstutz, C. Briand, O. Storchenegger, M. G. Grutter, Drug export pathway of multidrug exporter AcrB revealed by DARPin inhibitors. *PLoS Biol* **5**, e7 (2007).

18. F. Long *et al.*, Crystal structures of the CusA efflux pump suggest methionine-mediated metal transport. *Nature* **467**, 484-488 (2010).

19. C. C. Su *et al.*, Charged amino acids (R83, E567, D617, E625, R669, and K678) of CusA are required for metal ion transport in the Cus efflux system. *J Mol Biol* **422**, 429-441 (2012).

20. S. Murakami, R. Nakashima, E. Yamashita, A. Yamaguchi, Crystal structure of bacterial multidrug efflux transporter AcrB. *Nature* **419**, 587-593 (2002).

21. E. W. Yu, G. McDermott, H. I. Zgurskaya, H. Nikaido, D. E. Koshland, Jr., Structural basis of multiple drug-binding capacity of the AcrB multidrug efflux pump. *Science* **300**, 976-980 (2003).

22. R. Nakashima *et al.*, Structural basis for the inhibition of bacterial multidrug exporters. *Nature* **500**, 102-106 (2013).

23. G. Sennhauser, M. A. Bukowska, C. Briand, M. G. Grutter, Crystal structure of the multidrug exporter MexB from Pseudomonas aeruginosa. *J Mol Biol* **389**, 134-145 (2009).

24. J. R. Bolla *et al.*, Crystal structure of the Neisseria gonorrhoeae MtrD inner membrane multidrug efflux pump. *PLoS One* **9**, e97903 (2014).

25. C. C. Su *et al.*, Crystal structure of the CusBA heavy-metal efflux complex of Escherichia coli. *Nature* **470**, 558-562 (2011).

26. H. S. Kim, H. Nikaido, Different functions of MdtB and MdtC subunits in the heterotrimeric efflux transporter MdtB(2)C complex of Escherichia coli. *Biochemistry* **51**, 4188-4197 (2012).

27. L. Guan, T. Nakae, Identification of essential charged residues in transmembrane segments of the multidrug transporter MexB of Pseudomonas aeruginosa. *J Bacteriol* **183**, 1734-1739 (2001).

28. Y. Takatsuka, H. Nikaido, Threonine-978 in the transmembrane segment of the multidrug efflux pump AcrB of Escherichia coli is crucial for drug transport as a probable component of the proton relay network. *J Bacteriol* **188**, 7284-7289 (2006).

29. S. A. McKinney, C. Joo, T. Ha, Analysis of single-molecule FRET trajectories using hidden Markov modeling. *Biophysical journal* **91**, 1941-1951 (2006).

30. Z. Otwinowski, W. Minor, [20] Processing of X-ray diffraction data collected in oscillation mode. *Methods in enzymology* **276**, 307-326 (1997).

31. P. Emsley, K. Cowtan, Coot: model-building tools for molecular graphics. *Acta Crystallogr D Biol Crystallogr* **60**, 2126-2132 (2004).

32. P. D. Adams *et al.*, PHENIX: building new software for automated crystallographic structure determination. *Acta Crystallogr D Biol Crystallogr* **58**, 1948-1954 (2002).

33. A. T. Brunger *et al.*, Crystallography & NMR system: A new software suite for macromolecular structure determination. *Acta Crystallogr D Biol Crystallogr* **54**, 905-921 (1998).

34. M. Swoboda *et al.*, Enzymatic oxygen scavenging for photostability without pH drop in single-molecule experiments. *ACS Nano* **6**, 6364-6369 (2012).

35. A. N. Kapanidis *et al.*, Alternating-laser excitation of single molecules. *Accounts of chemical research* **38**, 523-533 (2005).

36. J. Park *et al.*, Single-molecule analysis reveals the kinetics and physiological relevance of MutL-ssDNA binding. *PloS one* **5**, e15496 (2010).

## Figures and captions

**Fig. 1a**

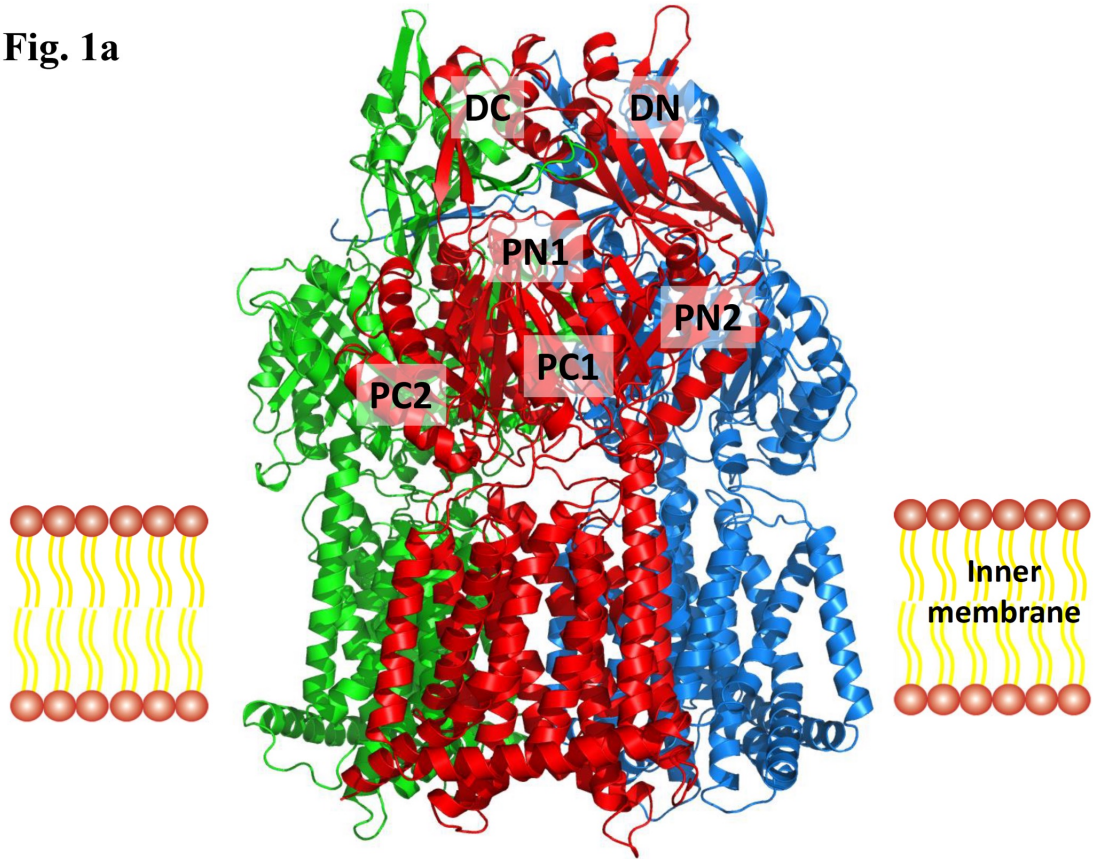


**Fig. 1b**

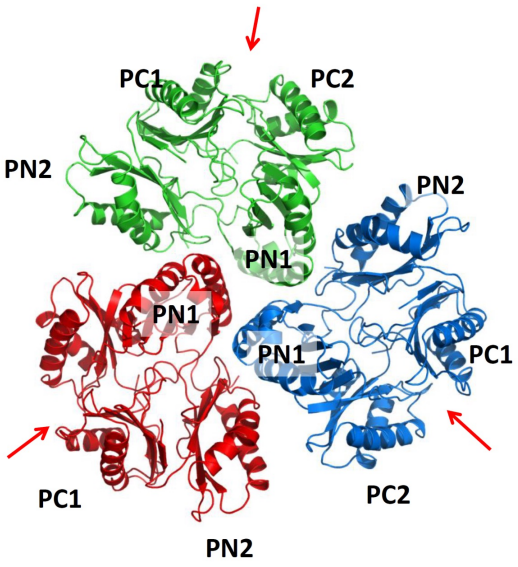


**Fig. 1c**

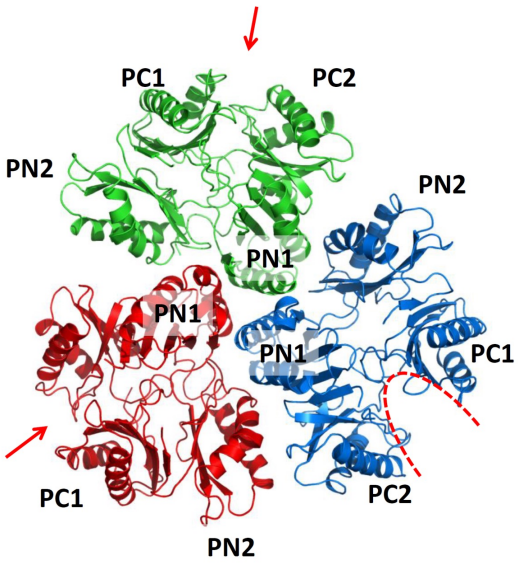

Fig. 1. Structure of the CmeB efflux pump. (a) Ribbon diagram of the form I structure of the CmeB homotrimer viewed in the membrane plane. Each subunit of CmeB is labeled with a different color. Sub-domains DN, DC, PN1, PN2, PC1 and PC2 are labeled on the front protomer (red). (b) Top view of the form I CmeB trimer. Each subunit of CmeB is colored differently. The six sub-domains DN, DC, PN1, PN2, PC1 and PC2 are labeled. In this conformation, the periplasmic cleft between PC1 and PC2 is closed in each protomer. (c) Top view of the form II CmeB trimer. In this conformation, only one out of the three periplasmic clefts formed between PC1 and PC2 is open.

**Fig. 2a**

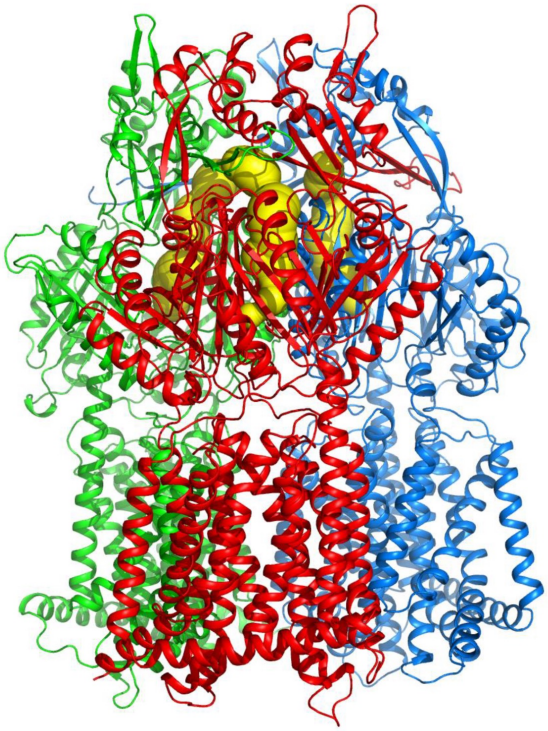

**Fig. 2b**

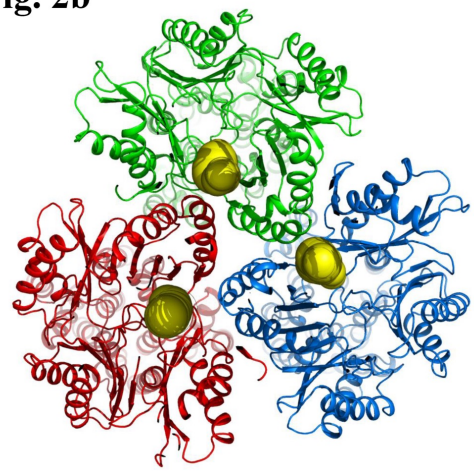

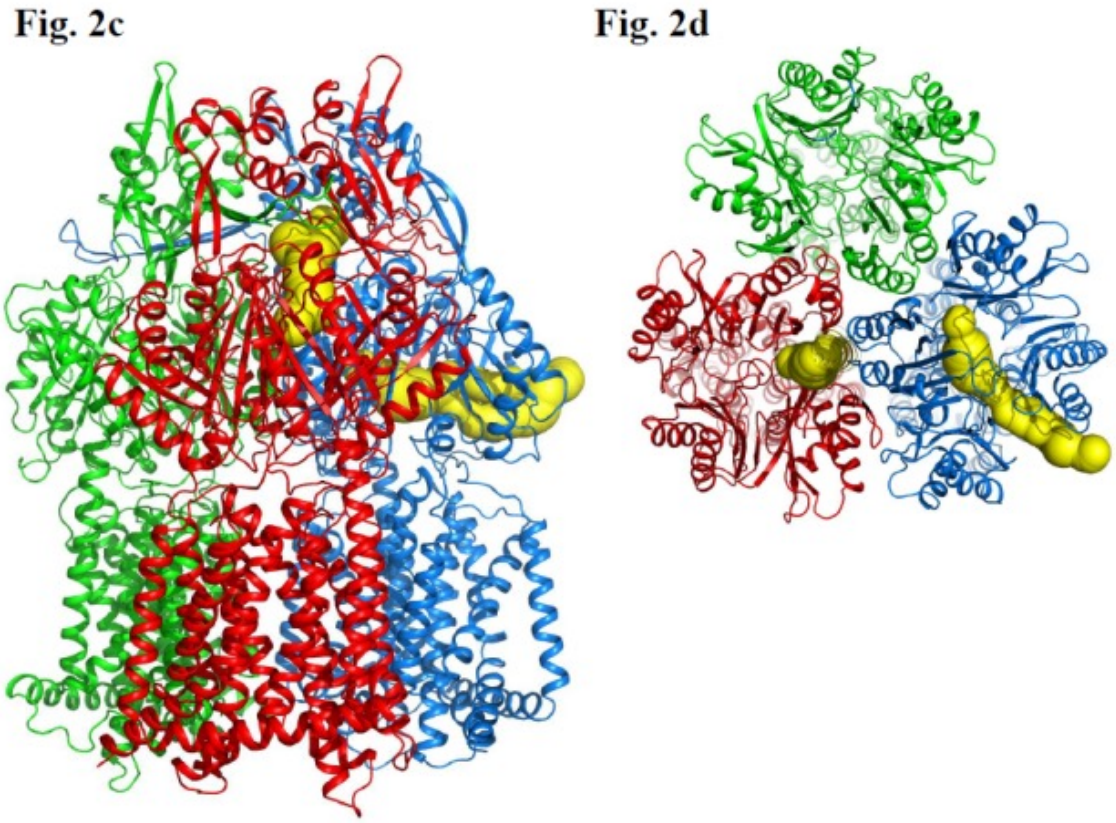


Fig. 2. Channels in the CmeB pump. (a) Side view and (b) top view of the channels formed by the periplasmic domain of the form I structure of the CmeB trimer. Each protomer creates an extrusion channel for drug export. (c) Side view and (d) top view of the channels formed by the periplasmic domain of the form II structure of the CmeB trimer. The "extrusion" protomer generates an extrusion channel that is similar to those observed in the form I structure. The "binding" protomer constitutes a channel, which leads through the opening of the periplasmic cleft and is exposed to solvent. The "resting" protomer does not form any channel. These channels were calculated using the program CAVER (http://loschmidt.chemi.muni.cz/caver).

Fig. 3a

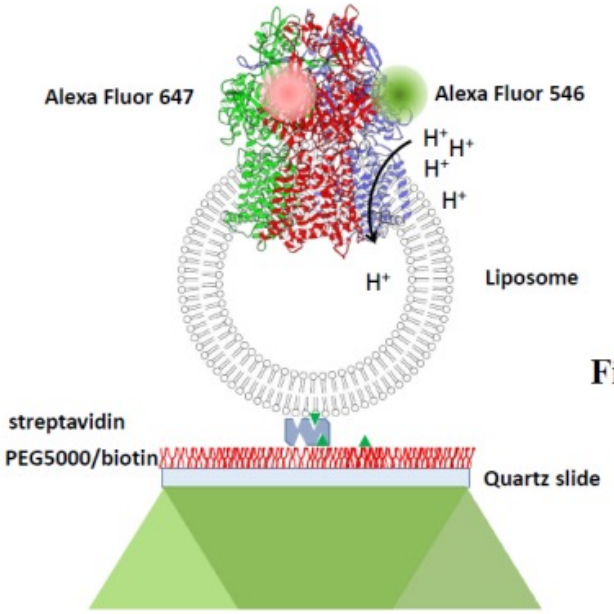


Fig. 3b

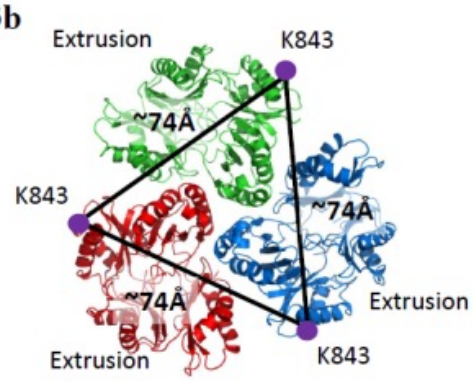


Fig. 3c

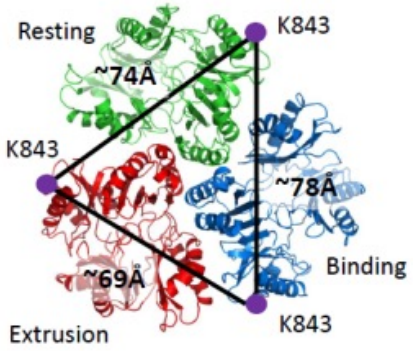


Fig. 3d

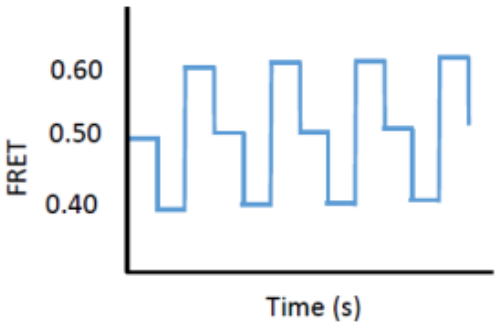


Fig. 3e

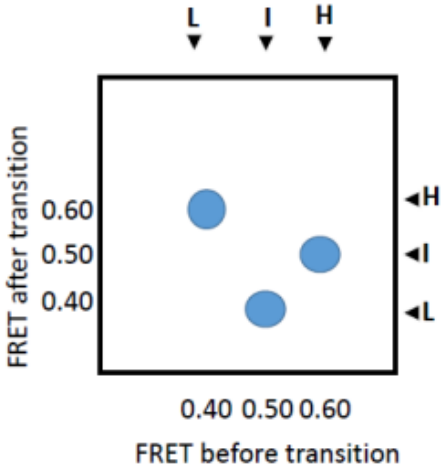

Fig. 3. Schematic diagram for visualizing the dynamics of the trimeric CmeB pump incorporated in proteoliposomes using total internal reflection smFRET imaging. (a) The three subunits of CmeB embedded in the lipid vesicle are colored differently. The AF546 and AF647 dyes are in green and magenta, respectively. (b) Inter-subunit distances measured between the two K843 residues of the form I CmeB trimer. (c) Inter-subunit distances measured between the two K843 residues of the form II CmeB trimer. (d) The predicted FRET trajectory and (e) predicted density plot of the transport dynamics of the CmeB pump if this pump functions via the proposed rotating mechanism.

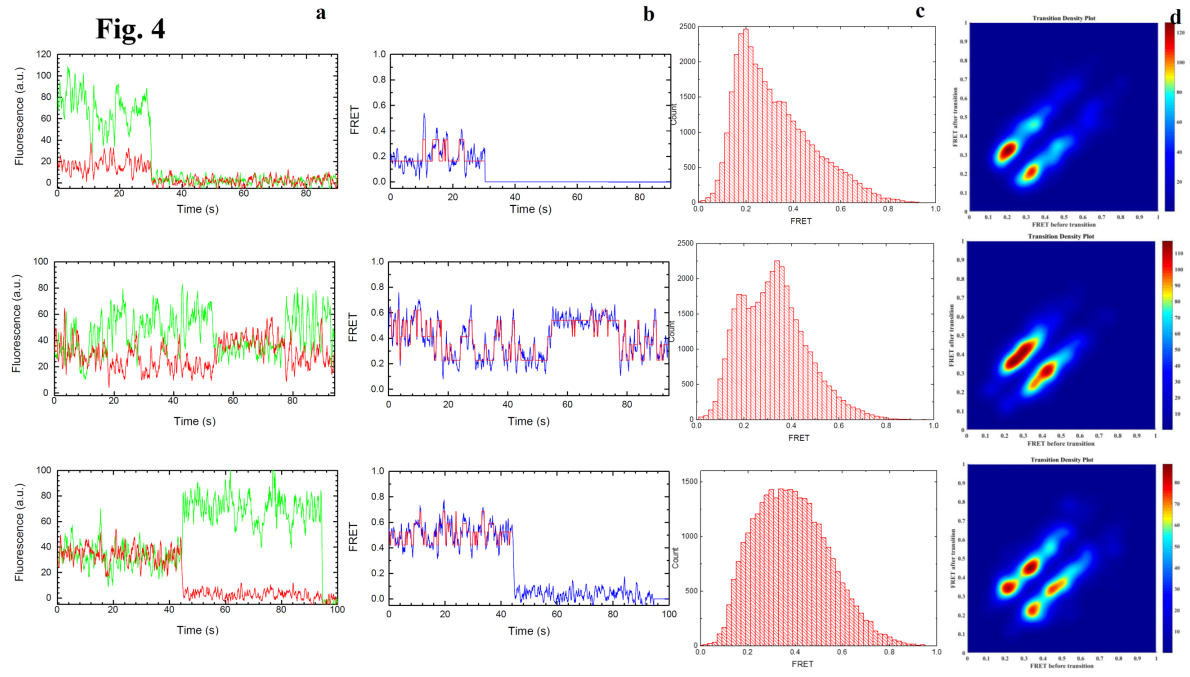


Fig. 4. Dynamics in the apo and substrate bound CmeB pump. (a) Experimental trace of CmeB single-molecule dynamics with donor (green) and acceptor (red) fluorescence (in the absence of Tdc, top panel; in the presence of 1 μM Tdc, middle panel; in the presence of 10 μM Tdc, bottom panel). (b) FRET trajectories (blue) and idealization of these FRET efficiencies (red)

(in the absence of Tdc, top panel; in the presence of 1 μM Tdc, middle panel; in the presence of 10 μM Tdc, bottom panel). (c) FRET efficiency population histograms of CmeB (in the absence of Tdc (*n* = 69 traces), top panel; in the presence of 1 μM Tdc (*n* = 77 traces), middle panel; in the presence of 10 μM Tdc (*n* = 73 traces), bottom panel). (d) Transition density plots for the CmeB efflux pump (in the absence of Tdc, top panel; in the presence of 1 μM Tdc, middle panel; in the presence of 10 μM Tdc, bottom panel).

**Fig. 5**

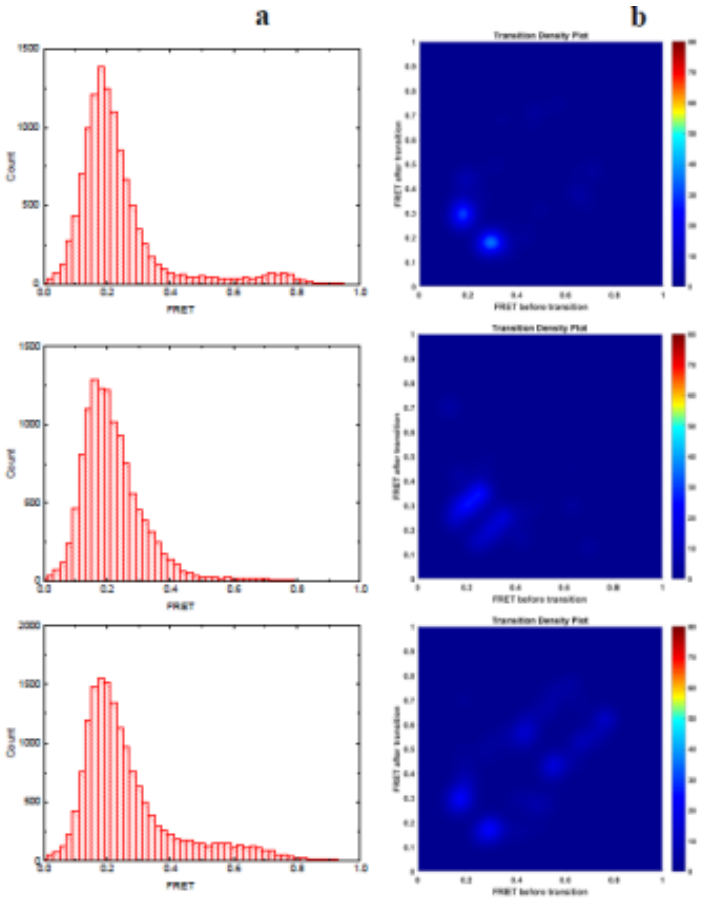


Fig. 5. Dynamics in the apo and substrate bound of the proton-relay mutant of CmeB. (a) FRET efficiency population histograms of CmeB (in the absence of Tdc (*n* = 40 traces), top panel; in the presence of 1 μM Tdc (*n* = 37 traces), middle panel; in the presence of 10 μM Tdc

($n$ = 47 traces), bottom panel). (b) Transition density plots for the CmeB efflux pump (in the absence of Tdc, top panel; in the presence of 1 μM Tdc, middle panel; in the presence of 10 μM Tdc, bottom panel).

**Fig. 6**

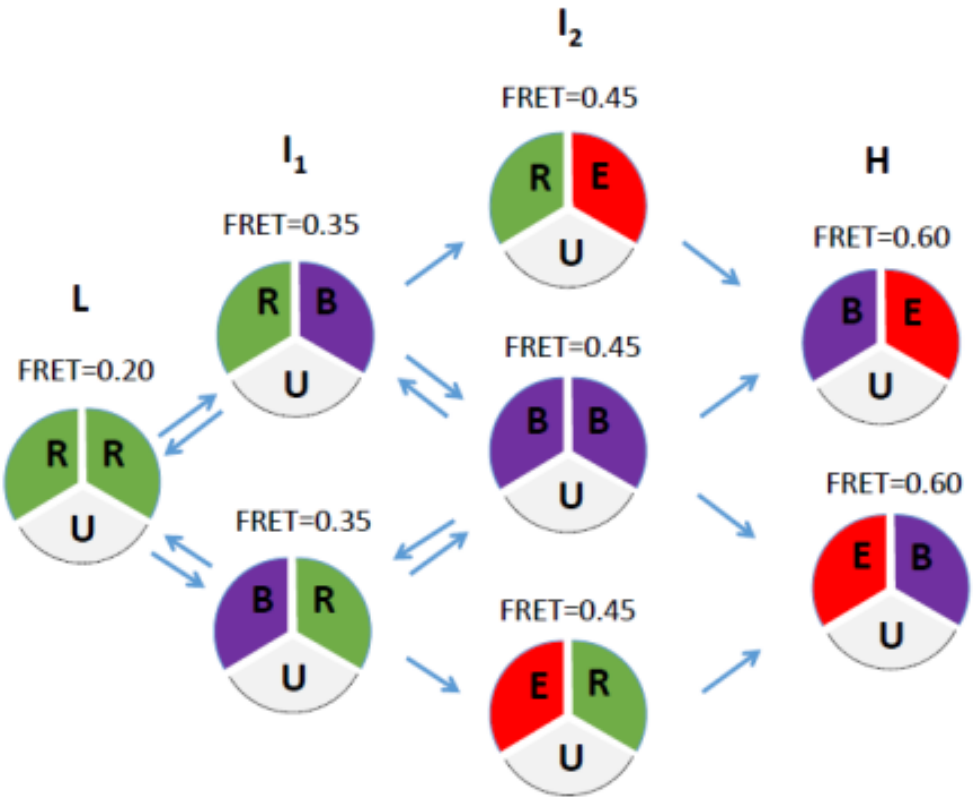


Fig. 6. Proposed simple model of drug efflux mechanism. This schematic diagram indicates that each protomer within the CmeB trimer can independently go through a sequence of conformational transitions, which lead to the extrusion of substrate (R, resting; B, binding; E, extrusion; U, unlabeled).

Table 1. Data collection and refinement statistics.

| **Data set** | CmeB (form I) | CmeB (form II) |
|---|---|---|
| **Data Collection** | | |
| Wavelength (Å) | 0.98 | 0.98 |
| Space group | C2 | P1 |
| Resolution (Å) | 50 – 3.15 (3.26 – 3.15) | 50 – 3.63 (3.77 – 3.63) |
| Cell constants (Å) | | |
| a | 300.71 | 120.85 |
| b | 147.54 | 127.94 |
| c | 120.03 | 169.58 |
| α, β, γ (°) | 90.0, 99.9, 90.0 | 99.8, 99.4, 85.0 |
| Molecules in ASU | 3 | 6 |
| Redundancy | 1.6 (1.6) | 3.7 (3.7) |
| Total reflections | 938,124 | 9060,758 |
| Unique reflections | 89,043 | 123,738 |
| Completeness (%) | 97.7 (98.0) | 97.7 (93.6) |
| $R_{sym}$ (%) | 10.3 (48.3) | 10.9 (48.8) |
| I / σ | 6.57 (1.4) | 6.6 (1.2) |
| **Refinement** | | |
| Resolution (Å) | 50 – 3.15 | 50 – 3.63 |
| $R_{work}$ (%) | 19.49 | 22.08 |
| $R_{free}$ (%) | 25.79 | 25.72 |
| Average B-factor (Å$^2$) | 60.19 | 94.5 |
| RMSD bond lengths (Å) | 0.009 | 0.004 |
| RMSD bond angles (°) | 1.39 | 0.73 |
| **Ramachandran plot** | | |
| most favoured (%) | 89.5 | 86.6 |
| additional allowed (%) | 9.9 | 12.2 |
| generously allowed (%) | 0.6 | 1.2 |
| disallowed (%) | 0.0 | 0.0 |

Table 2. Dwell times for CmeB transitions.

| | | FRET transition dwell time (s) | | | | | |
|---|---|---|---|---|---|---|---|
| CmeB | [Tdc] (μM) | L → $I_1$ | $I_1$ → L | $I_1$ → $I_2$ | $I_2$ → $I_1$ | $I_2$ → H | H → $I_2$ |
| K843C | 0 | 0.61 ± 0.06 | 0.31 ± 0.04 | 0.54 ± 0.04 | 0.26 ± 0.07 | | |
| | 1 | 0.52 ± 0.04 | 0.55 ± 0.05 | 0.62 ± 0.03 | 0.29 ± 0.03 | | |
| | 10 | 0.47 ± 0.03 | 0.65 ± 0.02 | 0.50 ± 0.03 | 0.49 ± 0.07 | 0.63 ± 0.07 | 0.35 ± 0.03 |
| K843C-D409A | 0 | 1.85 ± 0.13 | 0.35 ± 0.01 | | | | |
| | 1 | 1.68 ± 0.34 | 0.31 ± 0.05 | | | | |
| | 10 | 1.47 ± 0.39 | 0.39 ± 0.12 | | | | |

## Supplementary Materials

### Supplementary Figures

**S1a**

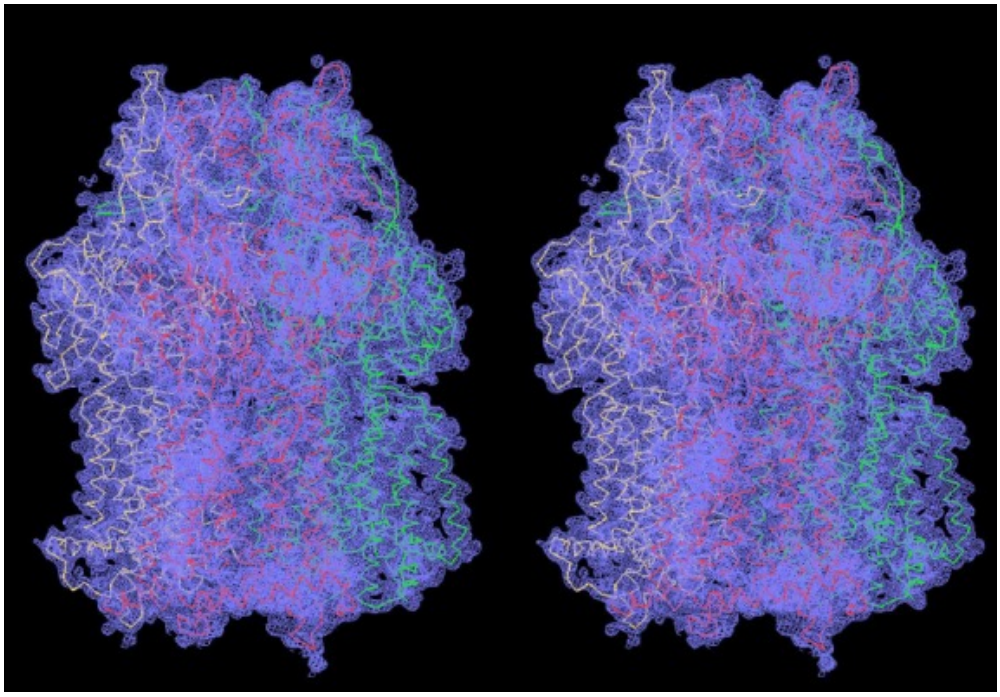

**S1b**

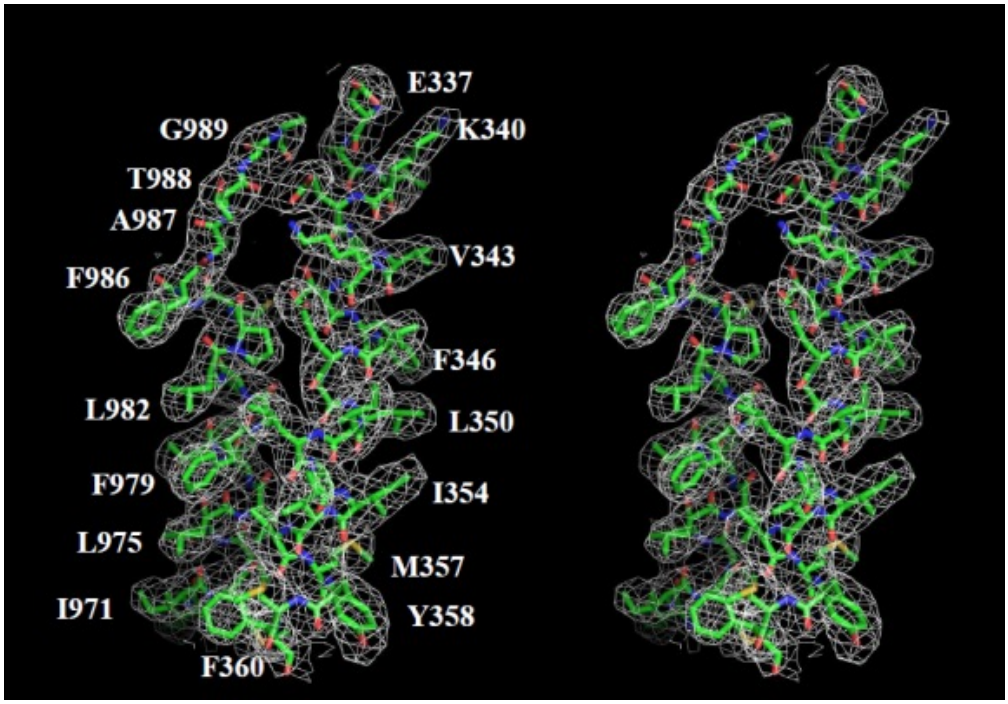

Fig. S1. Stereo view of the electron density maps of CmeB (form I) at a resolution of 3.15 Å. (a) The electron density maps are contoured at 1.2 σ. The Cα traces of the CmeB trimer in the asymmetric unit are included. (b) Representative section of the electron density in the vicinity of TMs 2 and 11 of CmeB. The electron density (colored white) is contoured at the 1.2 σ level and superimposed with the final refined model (green, carbon; red, oxygen; blue, nitrogen).

**S2a**

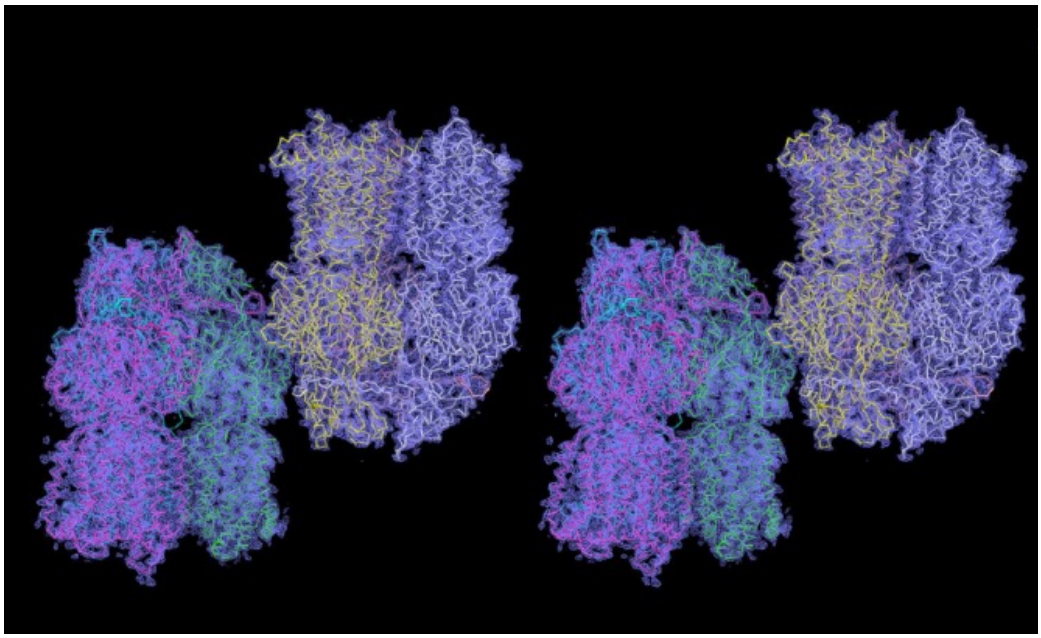

**S2b**

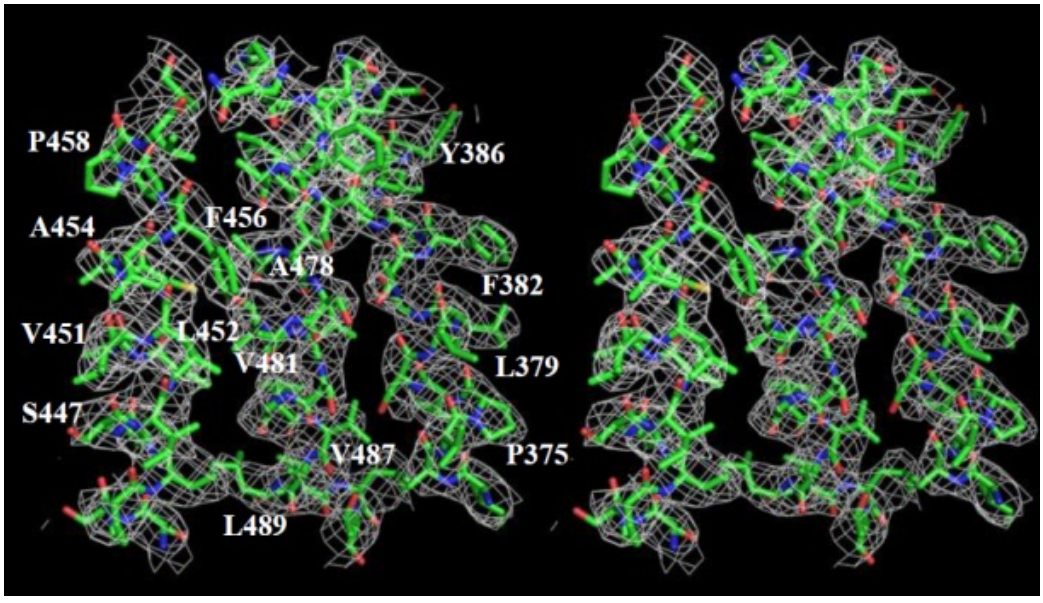

Fig. S2. Stereo view of the electron density maps of CmeB (form II) at a resolution of 3.63 Å. (a) The electron density maps are contoured at 1.2 σ. The Cα traces of the CmeB trimer in the asymmetric unit are included. (b) Representative section of the electron density in the vicinity of TMs 3, 5 and 6 of CmeB. The electron density (colored white) is contoured at the 1.2 σ level and superimposed with the final refined model (green, carbon; red, oxygen; blue, nitrogen).

## S3

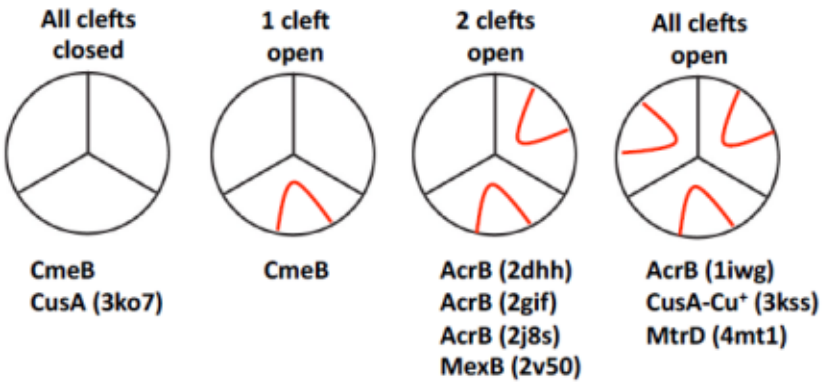


Fig. S3. Different conformations of the periplasmic domains of RND efflux pumps. The structures suggest that the periplasmic clefts formed by subdomains PC1 and PC2 could open or closed independently.

## S4

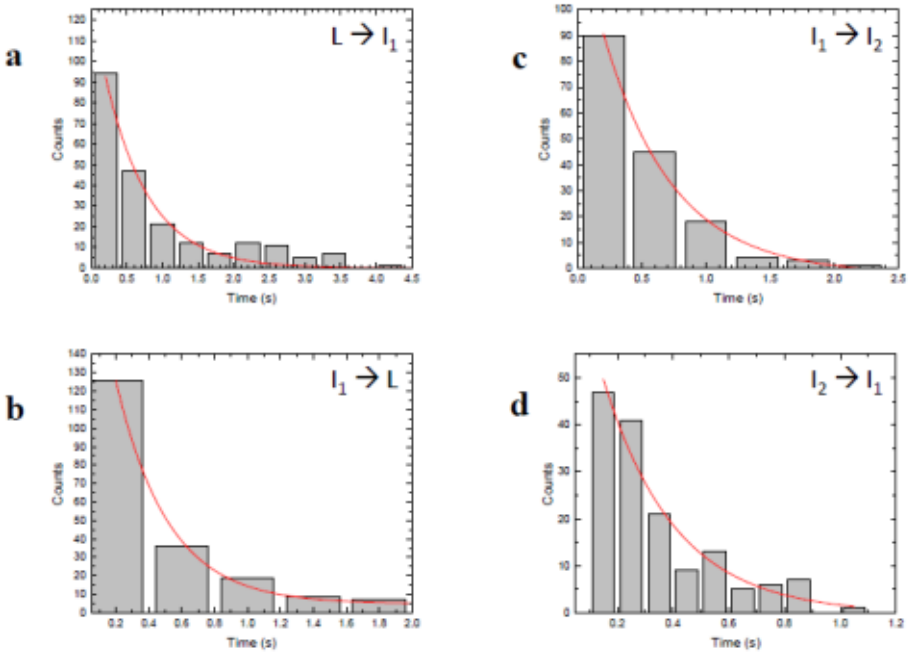


Fig. S4. Distribution of dwell times for CmeB (K843C) transitions in the absence of ligand. The exponential lifetime can be obtained by fitting the data with a single-exponential function, resulting in (a) $\tau_{L \rightarrow I1} = 0.61$ s ($k_{L \rightarrow I1} = 1.64$ s$^{-1}$), (b) $\tau_{I1 \rightarrow L} = 0.31$ s ($k_{I1 \rightarrow L} = 3.22$ s$^{-1}$), (c) $\tau_{I1 \rightarrow I2} = 0.54$ s ($k_{I1 \rightarrow I2} = 1.85$ s$^{-1}$) and (d) $\tau_{I2 \rightarrow I1} = 0.26$ s ($k_{I2 \rightarrow I1} = 3.84$ s$^{-1}$).

## S5

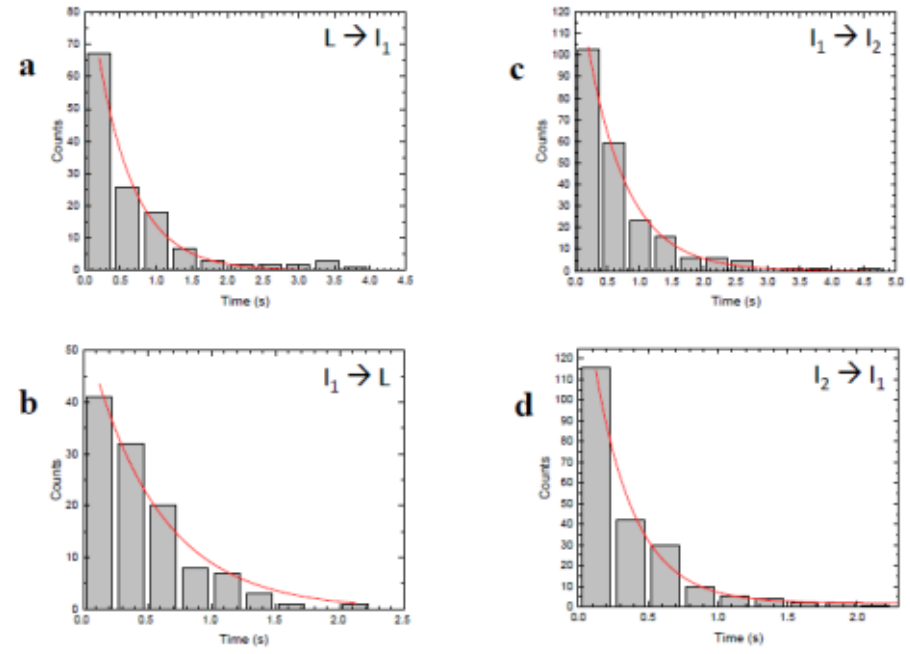

Fig. S5. Distribution of dwell times for CmeB (K843C) transitions in the presence of 1 μM Tdc. The exponential lifetime can be obtained by fitting the data with a single-exponential function, resulting in (a) $\tau_{L\rightarrow I1}$ = 0.52 s ($k_{L\rightarrow I1}$ = 1.92 $s^{-1}$), (b) $\tau_{I1\rightarrow L}$ = 0.55 s ($k_{I1\rightarrow L}$ = 1.82 $s^{-1}$), (c) $\tau_{I1\rightarrow I2}$ = 0.62 s ($k_{I1\rightarrow I2}$ = 1.61 $s^{-1}$) and (d) $\tau_{I2\rightarrow I1}$ = 0.29 s ($k_{I2\rightarrow I1}$ = 3.45 $s^{-1}$).

# S6

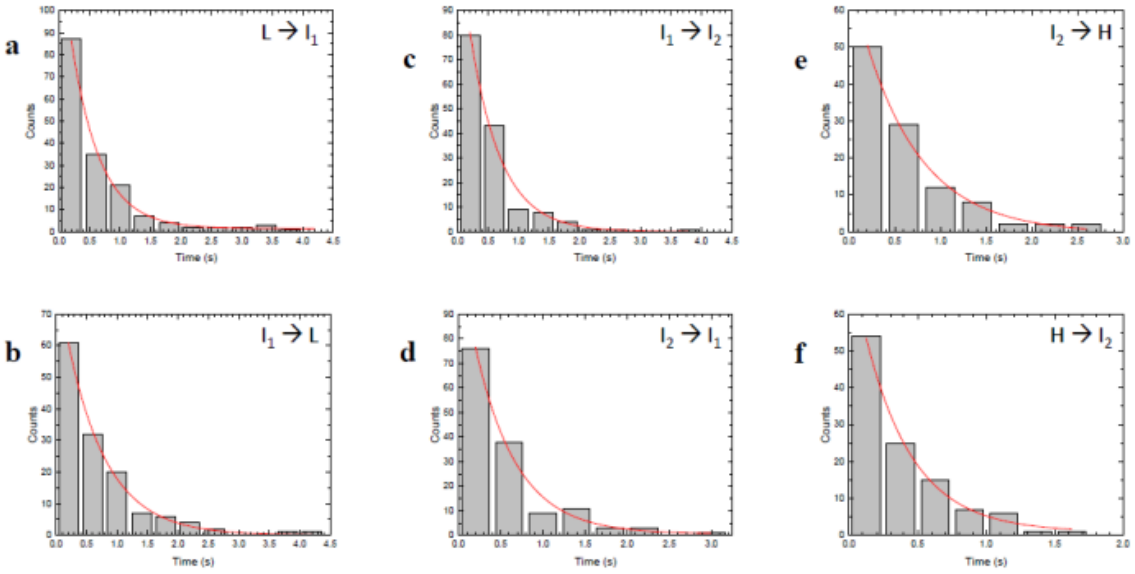


Fig. S6. Distribution of dwell times for CmeB (K843C) transitions in the presence of 10 μM Tdc. The exponential lifetime can be obtained by fitting the data with a single-exponential function, resulting in (a) $\tau_{L\rightarrow I1}$ = 0.47 s ($k_{L\rightarrow I1}$ = 2.13 $s^{-1}$), (b) $\tau_{I1\rightarrow L}$ = 0.65 s ($k_{I1\rightarrow L}$ = 1.54 $s^{-1}$), (c) $\tau_{I1\rightarrow I2}$ = 0.50 s ($k_{I1\rightarrow I2}$ = 2.00 $s^{-1}$), (d) $\tau_{I2\rightarrow I1}$ = 0.49 s ($k_{I2\rightarrow I1}$ = 2.04 $s^{-1}$), (e) $\tau_{I2\rightarrow H}$ = 0.63 s ($k_{I2\rightarrow H}$ = 1.59 $s^{-1}$) and (f) $\tau_{H\rightarrow I2}$ = 0.35 s ($k_{H\rightarrow I2}$ = 2.86 $s^{-1}$).

# S7

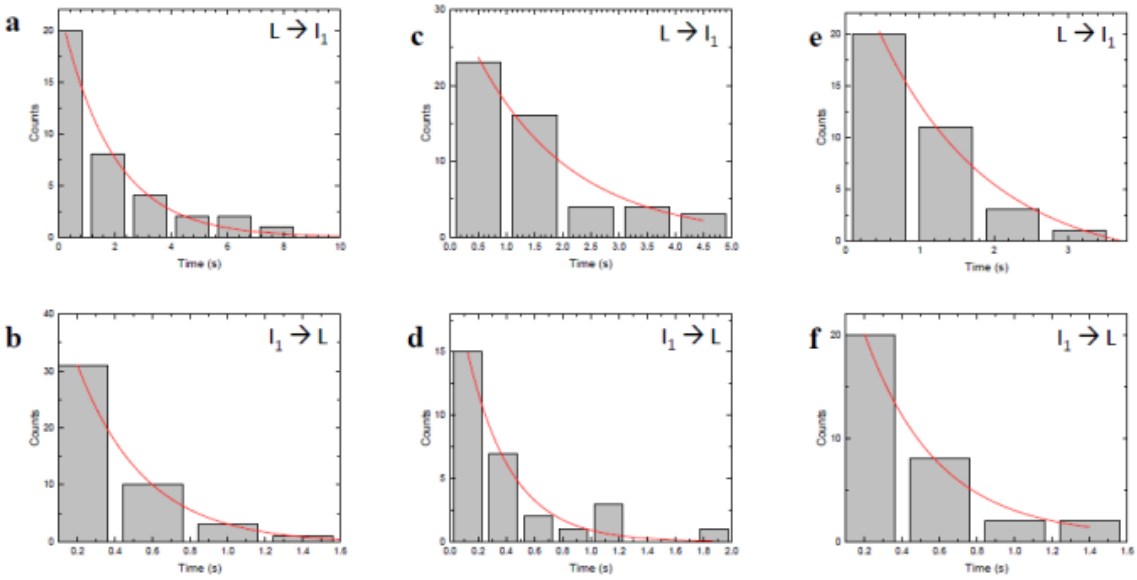


Fig. S7. Distribution of dwell times for CmeB (K843C-D409A) transitions. The exponential lifetime can be obtained by fitting the data with a single-exponential function. In the absence of ligand, the resulting dwell times are (a) $\tau_{L \rightarrow I1}$ = 1.85 s ($k_{L \rightarrow I1}$ = 0.54 $s^{-1}$) and (b) $\tau_{I1 \rightarrow L}$ = 0.35 s ($k_{I1 \rightarrow L}$ = 2.86 $s^{-1}$). In the presence of 1 μM Tdc, the resulting dwell times are (c) $\tau_{L \rightarrow I1}$ = 1.68 s ($k_{L \rightarrow I1}$ = 0.60 $s^{-1}$) and (d) $\tau_{I1 \rightarrow L}$ = 0.31 s ($k_{I1 \rightarrow L}$ = 3.22 $s^{-1}$). In the presence of 10 μM Tdc, the resulting dwell times are (e) $\tau_{L \rightarrow I1}$ = 1.47 s ($k_{L \rightarrow I1}$ = 0.68 $s^{-1}$) and (f) $\tau_{I1 \rightarrow L}$ = 0.39 s ($k_{I1 \rightarrow L}$ = 2.56 $s^{-1}$).

# CHAPTER 5. GENERAL CONCLUSIONS AND FUTURE DIRECTIONS

Active drug efflux is one of the major reasons for bacterial resistance against antibiotics. Efflux pumps of the RND superfamily play, by far, the predominant role in providing multidrug resistance to Gram-negative bacteria. As emphasized before, these pumps associate with two other classes of proteins: a periplasmic "membrane fusion protein" (MFP) and an "outer membrane factor" (OMF) protein. This construction is highly beneficial because it allows direct export of drugs into the extracellular space, instead of the periplasm. Also, it creates an outer membrane barrier to the drugs exported outside the cell, and hence makes bacterial cells less susceptible to drugs [1]. More recent efforts have also been directed towards understanding the complex regulatory pathways controlling the expression of multidrug resistance (MDR) genes. Studies have shown that most regulators act by directly binding to a similar range of toxic substrates as exported by the pump whose expression they control [2]. This dissertation is focused on the study of a transcriptional regulator Rv1219c of *M. tuberculosis* and two RND superfamily proteins: hopanoid transporter HpnN of *B. multivorans* and CmeB drug efflux pump of *C. jejuni.*

In Chapter 2, we elucidated the structural basis of Rv1219c regulation by determining the crystal structure of Rv1219c. The Rv1217c-Rv1218c multidrug efflux system, which belongs to the ATP-binding cassette superfamily, recognizes and actively extrudes a variety of structurally unrelated toxic chemicals including, novobiocins, pyrazolones, biarylpiperazines, bisanilinopyrimidines, pyrroles, and pyridines [3]. The expression of Rv1217c-Rv1218c is controlled by TetR-like transcriptional regulator Rv1219c, which is encoded by a gene immediately upstream of *rv1218c.* The crystal structure of Rv1219c reveals a dimeric arrangement of two monomers in the asymmetric unit, similar to members of the TetR family

of transcriptional regulators. The N-terminal domains of the Rv1219c dimer are separated by a large center-to-center distance of 64 Å. The C-terminal domain of each protomer possesses a large cavity. Docking studies suggested that this large cavity can accommodate a variety of structurally unrelated antimicrobial agents, and hence could be forming a multidrug binding pocket. The internal wall of this multidrug binding pocket is surrounded by seven aromatic residues, indicating that drug binding could possibly be governed by aromatic stacking interactions. In addition, fluorescence polarization studies reveal that Rv1219c is capable of binding drugs in the micromolar range [4].

Overall, the major challenges and the future directions are to crystallize the ligand-bound and DNA-bound forms of Rv1219c. Obtaining these structures might facilitate understanding the regulatory mechanism in *M. tuberculosis*, leading to rational designing of the drugs. These drugs could further be used to block the function of Rv1219c and hence inhibit the expression of the multidrug efflux pump.

In Chapter 3, we elucidated the structures of HpnN transporter which has been reported to be essential for the cell wall biogenesis [5] in *B. multivorans.* Two distinct conformations of HpnN (forms I and II) were captured in two different forms of crystal. In the asymmetric unit of both structures, two monomers were arranged as a dimer. Also, each HpnN protomer created a channel spanning the outer leaflet of the inner membrane and up to the periplasmic domain. Overall, HpnN has a very unique structure, since it is the only RND protein to be found to exist as a dimer to date. The striking difference between forms I and II of HpnN exists in the periplasmic domain, where the form II HpnN is open compared to form I HpnN. The two different conformations of HpnN basically depict the possible transient states involved in the transport of hopanoids from the inner membrane to the periplasm. To further confirm the importance of HpnN in hopanoid transport, *B. thailandensis* E264 strain was used. The knock

out *B. thailandensis* E264*ΔhpnN* cells, either alone or transformed with empty vector pHERD20T, were unable to grow in LB media supplemented with antibiotics like chloramphenicol, novobiocin or polymyxin B. However, the growth was restored in *B. thailandensis* E264*ΔhpnN* cells compensated with pHERD20TΩhpnN under the same conditions. This suggests that HpnN is critical for mediating multidrug resistance in *B. thailandensis.* Further, mutagenesis studies using the *B. thailandensis* E264*ΔhpnN* cells compensated with pHERD20TΩhpnN confirmed that the conserved residues L48, F117, D344, F541, W661, T818, and T819 are important for the functioning of HpnN.

The major goal of this project was to decipher one of the key mechanisms that *Burkholderia* pathogens employ to mediate drug resistance and hence affect the immunocompromised individuals such as cystic fibrosis pateints. HpnN plays a big role in the virulence of these pathogens by shuttling hopanoids towards the outer membrane and hence decreasing the permeability of the cell towards the antibiotics. In order to further investigate the hopanoid transport mechanism involved in HpnN, techniques like sm-FRET and single particle cryo-EM would prove quite useful to visualize the different conformations and unravel the overall functional dynamics of HpnN protein.

In Chapter 4, we determined the crystal structures of membrane protein CmeB in two different forms, both of which form an asymmetric trimer, resembling a typical RND-family protein. The most interesting fact here was that the periplasmic cleft between subdomains PC1 and PC2 was closed in all the three protomers of form I CmeB, whereas in the form II CmeB the periplasmic cleft of one of the protomers was found to be open. In the asymmetric trimeric structure of the AcrB multidrug transporter, each monomer displays a distinct conformational state. It has been proposed that the three monomers in AcrB represent the consecutive states involved in the drug transport cycle: access, binding and extrusion. Thus, a functionally

rotating mechanism was suggested for the extrusion of drugs in AcrB, where each monomer works in a cooperative fashion with the other [6, 7].

The trimeric structure of form I CmeB was found to have all three periplasmic clefts closed and hence resembles the “extrusion” state of AcrB. Surprisingly, in the asymmetric trimer of form II CmeB, the periplasmic cleft of only one protomer was open, similar to the “binding” state of AcrB. Although, the periplasmic clefts are closed in the other two protomers of form II CmeB, only one of them relates closely to the “extrusion” state of form I CmeB. The other protomer surprisingly displayed a distinct conformation from the “extrusion” form, forming a new state. We believed this new conformation represented one of the intermediate states involved in drug transport never seen before [8, 9, 10]. The drug transport mechanism of CmeB was further elucidated using single molecule fluorescence resonance energy transfer (sm-FRET), where we directly observed the conformational dynamics in individual CmeB trimers embedded in membrane vesicles. FRET measurements indicated that each CmeB subunit undergoes uncoordinated conformational transitions which are independent of each other. Hence we postulated that individual protomers of these trimeric RND pumps might be capable of binding and exporting drugs independently, rather than operating in a synchronized way.

One of the future directions in this project is to crystallize CmeB with a native substrate in order to determine the important residues in the binding pocket and the conformational changes involved. Hence, the structural determination would further aid the understanding of drug efflux mechanism in *Campylobacter jejuni*.

MDR is a natural and unavoidable phenomenon, posing a serious threat to the public health. Pathogens tend to adopt various resistance mechanisms in order to survive various unfavorable conditions. An effort towards continuous development of newer drugs along with

cooperative action at global level for implementation of various awareness programs to highlight the appropriate use of drugs is needed to combat the MDR. The work in this thesis is aimed at improving the knowledge of structural and functional mechanisms of proteins controlling MDR and hence contribute towards development of novel therapies to counteract infectious diseases [11].

## References

1) Nikaido H. Multidrug Resistance in Bacteria. *Annu Rev Biochem.* 2009; **78**:119–46.

2) S. Grkovic, M.H. Brown, R.A. Skurray. Transcriptional regulation of multidrug efflux pumps in bacteria. *Semin. Cell Dev. Biol.*, **12** (2001), pp. 225–237.

3) Balganesh M, Kuruppath S, Marcel N, Sharma S (2010). Rv1218c, an ABC transporter of *Mycobacterium tuberculosis* with implications in drug discovery. *Antimicrob Agents Chemother* **54**:5167–5172.

4) Kumar N, Radhakrishnan A, Wright CC, Chou TH, Lei HT, Bolla JR, Tringides ML, Rajashankar KR, Su CC, Purdy GE, Yu EW. Crystal Structure of the transcriptional regulator Rv1219c of *Mycobacterium tuberculosis*. *Protein Sci.* (2014).

5) Welander PV, Hunter RC, Zhang L, et al. Hopanoids play a role in membrane integrity and pH homeostasis in *Rhodopseudomonas palustris* TIE-1. *J Bacteriol* (2009); **191**:6145-56.

6) Seeger MA, Schiefner A, Eicher T, Verrey F, Diederichs K, Pos KM (2006). Structural asymmetry of AcrB trimer suggests a peristaltic pump mechanism. *Science* **313**:1295–1298.

7) Murakami S., Nakashima R., Yamashita E., Matsumoto T., Yamaguchi A. Crystal structures of a multidrug transporter reveal a functionally rotating mechanism (2006) *Nature*, **443** (7108), pp. 173-179.

8) G. Sennhauser, M.A. Bukowska, C. Briand, M.G. Grutter. Crystal structure of the multidrug exporter MexB from *Pseudomonas aeruginosa*. *J Mol Biol*, **389** (2009), pp. 134–145.

9) Long F, et al. (2010). Crystal structures of the CusA efflux pump suggest methionine-mediated metal transport. *Nature* **467**(7314):484–488.

10) J.R. Bolla, C.C. Su, S.V. Do, A. Radhakrishnan, N. Kumar, F. Long, T.H. Chou, J.A. Delmar, H.T. Lei, K.R. Rajashankar, W.M. Shafer, E.W. Yu. Crystal structure of the *Neisseria gonorrhoeae* MtrD inner membrane multidrug efflux pump. *PLoS One*, **9** (2014), p. e97903.

11) Jyoti Tanwar, Shrayanee Das, Zeeshan Fatima, and Saif Hameed, "Multidrug Resistance: An Emerging Crisis," Interdisciplinary Perspectives on Infectious Diseases, vol. 2014, Article ID 541340, 7 pages, 2014.

## ACKNOWLEDGEMENTS

Firstly, I would like to express my sincere gratitude to my advisor Prof. Edward Yu for the tremendous support, motivation and patience he has shown throughout my Ph.D. studies. His guidance in my research and thesis writing was priceless. His efforts towards shaping up my career gives me privilege to proudly accept that I could not have found a better advisor and mentor.

Besides my advisor, I would like to thank the rest of my POS committee: Dr. Drena Dobbs, Dr. Young-Jin Lee, Dr. Emily Smith and Dr. Wenyu Huang, for their valuable advice and encouragement to help broaden my research from various perspectives.

I feel very fortunate to work in close collaboration with Dr. Chih Chia Su and Dr. Feng Long. Special thanks to my fellow lab mates Dr. Hsiang-Ting Lei, Dr. Jani Reddy Bolla, Abhijith Radhakrishnan, Tsung-Han Chou and Jared Delmar for the stimulating discussions, providing courage in tough times, for enormous support during the sleepless nights we were working together in order to meet the deadlines, and for all the fun we had together in last five years. I fall short of words to mention how much each one of them means to me and the way they always stood by me.

I would like to thank Dr. Kanagalaghatta R. Rajashankar, Dr. Surajit Banerjee and all the staff members of NECAT at Advanced Photon Source, Argonne National Lab for helping in X-ray data collection and structure determination. I want to thank our collaborators Dr. Georgiana E. Purdy for the EMSA studies related to Rv1219c and Dr. Yeon-Kyon Shin for the sm-FRET experiments related to CmeB. I also thank the ISU facilities including, Chemical Instrumentation Facility, DNA facility, protein facility and hybridoma facility. Special thanks to Marit Nilsen-Hamilton for letting me use their Microplate reader for my experiments.

I feel indebted to my friend Bhuvnesh Bharti for his immnese support and motivation in helping me get into the graduate school. Great thanks to Pratik, Mani and Gargey for providing me with family-like feeling and comfort in Ames. I would always cherish their company and the fun-packed trips they organized. I would like to thank Aleem, Uma, Raghuvamsy, Naresh, Bharat, and Mohit whom I made wonderful friends with during my PhD journey. Thanks to Molly and Caribou Coffee staff for the afternoon coffees and wonderful refreshing ambience. The list of friends I want to thank doesn't end here. I really thank everyone for the great time spent and the unforgettable memories made together.

Last but not the least, I would like to thank my parents and my brother. They were my greatest pillars of support and strength all this time. I fall short of words thanking my brother Vinit Sharma for taking care of parents and managing all the home related issues along with his rigorous job schedule, while was away pursuing PhD in US. I want to express my appreciation to my beloved fiancée Nidhi K. Bhatia for being a wonderful friend and sharing every moment of pain and joy through all these years. I have evolved as a person after having her in my life and find myself extremely lucky as she was always inspiring and very caring. Finally, I would like to dedicate this dissertation to my mama and papa, whose blessings and enormous support made this accomplishment possible.

# APPENDIX. *CURRICULUM VITAE*

**Author:** Nitin Kumar

## EDUCATION

| | |
|---|---|
| **2011-2016** | PhD Chemistry<br>Iowa State University, Ames, IA<br>Advisor: Prof. Edward W. Yu |
| **2009-2011** | MSc (Hons. School) Chemistry<br>Panjab University, India<br>Advisor: Prof. Vikas |
| **2006-2009** | BSc (Hons. School) Chemistry<br>Panjab University, India |

## RESEARCH EXPERIENCE

| | |
|---|---|
| **2011-2016** | Research Assistant<br>Department of Chemistry<br>Iowa State University, Ames, IA |

## TEACHING EXPERIENCE

**2011-2016** Teaching Assistant
Department of Chemistry
Iowa State University, Ames, IA

Supervised and graded undergraduate classes and labs of 20 students for a total of 8 semesters, which included:

- General Chemistry Recitation
- General Chemistry Laboratory
- Chemical Thermodynamics

## PUBLICATIONS

1) **Kumar N***, Su CC*, Yin L*, Radhakrishnan A, Chou TH, Dai L, Delmar JA, Zhang Q, Shin YK and Yu EW (2016). Structures and transport dynamics of a multidrug efflux pump. (manuscript in preparation)

2) **Kumar N***, Su CC*, Chou TH, Radhakrishnan A, Delmar JA, Rajashankar KR, and Yu EW (2016). Crystal structure of a hopanoid transporter of *Burkholderia*.
(manuscript in preparation)

3) **Kumar N***, Radhakrishnan A, Su CC, Osteryoung KW, Yu EW (2015). Crystal structure of a conserved domain in the intermembrane space region of the plastid division protein ARC6. *Protein Sci.* 25: 523-529. doi: 10.1002/pro.2825

4) Delmar JA, Chou TH, Wright CC, Licon MH, Doh JK, Radhakrishnan A**, Kumar N**, Lei HT, Bolla JR, Rajashankar KR, Su CC, Purdy GE, Yu EW (2015). Structural Basis for the Regulation of the MmpL Transporters of *Mycobacterium tuberculosis*. *J. Biol. Chem.* 290: 28559-28574. doi: 10.1074/jbc.M115.683797

5) Chou TH, Delmar JA, Wright CC, **Kumar N**, Radhakrishnan A, Doh JK, Licon MH, Bolla JR, Lei HT, Rajashankar KR, Su CC, Purdy GE, Yu EW (2015). Crystal structure of the *Mycobacterium tuberculosis* transcriptional regulator Rv0302. *Protein Sci.* 25: 1942-1955. doi: 10.1002/pro.2802

6) Bolla JR, Su CC, Delmar JA, Radhakrishnan A, **Kumar N**, Chou TH, Long F, Rajashankar KR, Yu EW (2015). Crystal structure of the *Alcanivorax borkumensis* YdaH transporter reveals an unusual topology. *Nat. Commun.* 6: 6874. doi: 10.1038/ncomms7874

7) Su CC, Bolla JR, **Kumar N**, Radhakrishnan A, Long F, Delmar JA, Chou TH, Rajashankar KR, Shafer WM, Yu EW (2015). Structure and function of *Neisseria gonorrhoeae* MtrF illuminates a class of antimetabolite efflux pumps. *Cell Rep.* 11(1): 61-70. doi: 10.1016/j.celrep.2015.03.003.

8) Bolla JR, Su CC, Do SV, Radhakrishnan A, **Kumar N**, Long F, Chou TH, Delmar JA, Lei HT, Rajashankar KR, Shafer WM, Yu EW (2014). Crystal structure of the *Neisseria gonorrhoeae* MtrD inner membrane multidrug efflux pump. *PLoS ONE* 9(6): e97903. doi:10.1371/journal.pone.0097903

9) Lei HT, Chou TH, Su CC, Bolla JR, **Kumar N**, Radhakrishnan A, Long F, Delmar JA, Do SV, Rajashankar KR, Shafer WM, Yu EW (2014). Crystal structure of the open state of the *Neisseria gonorrhoeae* MtrE outer membrane channel. *PLoS ONE* 9(6): e97475. doi: 10.1371/journal.pone.0097475

10) **Kumar N***, Su CC*, Radhakrishnan A*, Long F, Bolla JR, Lei HT, Delmar JA, Do SV, Chou TH, Rajashankar KR, Zhang Q, Yu EW (2014). Crystal structure of the *Campylobacter jejuni* CmeC outer membrane channel. *Protein Sci.* 23: 954-961. doi:10.1002/pro.2478

11) **Kumar N***, Radhakrishnan A*, Wright CC, Chou TH, Tringides ML, Bolla JR, Lei HT, Rajashankar KR, Su CC, Purdy GE, Yu EW (2014). Crystal structure of the transcriptional regulator Rv0678 of *Mycobacterium tuberculosis*. *J. Biol. Chem.* 289: 16526-16540. doi: 10.1074/jbc.M113.538959

12) **Kumar N***, Radhakrishnan A*, Wright CC, Chou TH, Lei HT, Bolla JR, Tringides ML, Rajashankar KR, Su CC, Purdy GE, Yu EW (2014). Crystal Structure of the transcriptional regulator Rv1219c of *Mycobacterium tuberculosis*. *Protein Sci*. 23: 423-432. doi: 10.1002/pro.2424

** Co-first author*

**PRESENTATIONS**

"Crystal structure of the transcriptional regulator Rv1219c of Mycobacterium tuberculosis" at the 49th Midwest Regional Meeting of the American Chemical Society - MWRM 2014, University of Missouri – Columbia, MO (Oral Presentation).